

UNIVERSIDADE FEDERAL DO ESPÍRITO SANTO
CENTRO DE CIÊNCIAS EXATAS
PROGRAMA DE PÓS-GRADUAÇÃO EM FÍSICA

Erik Fissicaro Procópio

**Electronic Properties of Single-layer In_2Se_3 :
from Photocatalysis to Non-trivial Band
Topology**

VITÓRIA

ERIK FISSICARO PROCÓPIO

**Electronic Properties of Single-layer In_2Se_3 : from
Photocatalysis to Non-trivial Band Topology**

Tese apresentada à Universidade Federal do Espírito Santo como parte das exigências do Programa de Pós-Graduação em Física da Matéria Condensada, para obtenção do título de Doutor em Física.

VITÓRIA

2022

Ficha catalográfica disponibilizada pelo Sistema Integrado de Bibliotecas - SIBI/UFES e elaborada pelo autor

P963e Procopio, Erik, 1991-
Electronic Properties of Single-layer In₂Se₃: from Photocatalysis to Non-trivial Band Topology / Erik Procopio. - 2022.
91 f. : il.

Orientador: Wanderla Luis Scopel.
Coorientador: Wendel Silva Paz.
Tese (Doutorado em Física) - Universidade Federal do Espírito Santo, Centro de Ciências Exatas.

1. Matéria Condensada. 2. Teoria do Funcional Densidade. 3. Isolantes Topológicos. 4. Materiais Bidimensionais. 5. Semicondutores. I. Scopel, Wanderla Luis. II. Paz, Wendel Silva. III. Universidade Federal do Espírito Santo. Centro de Ciências Exatas. IV. Título.

CDU: 53



UNIVERSIDADE FEDERAL DO ESPÍRITO SANTO
CENTRO DE CIÊNCIAS EXATAS
PROGRAMA DE PÓS-GRADUAÇÃO EM FÍSICA

“Electronic Properties of Single-layer In₂ Se₃ : from Photocatalysis to Non-trivial Band Topology”

ERIK FISSICARO PROCOPIO

Tese submetida ao Programa de Pós-Graduação em Física da Universidade Federal do Espírito Santo, por webconferência, como requisito parcial para a obtenção do título de Doutor em Física.

Aprovada por:

Prof. Dr. Ângelo Malachias de Souza
(UFMG)

Prof. Dr. Wanderlã Luis Scopel
(Orientador - PPGFis/UFES)

Prof. Dr. Rodrigo Garcia Amorim
(UFF)

Prof. Dr. Wendel Silva Paz
(Coorientador - PPGFis/UFES)

Prof. Dr. Edson Passamani Caetano
(PPGFIS/UFES)

Vitória-ES, 02 de setembro de 2022.



UNIVERSIDADE FEDERAL DO ESPÍRITO SANTO

PROTOCOLO DE ASSINATURA



O documento acima foi assinado digitalmente com senha eletrônica através do Protocolo Web, conforme Portaria UFES nº 1.269 de 30/08/2018, por
WENDEL SILVA PAZ - SIAPE 1034700
Departamento de Física - DF/CCE
Em 05/09/2022 às 14:49

Para verificar as assinaturas e visualizar o documento original acesse o link:
<https://api.lepisma.ufes.br/arquivos-assinados/555232?tipoArquivo=O>



UNIVERSIDADE FEDERAL DO ESPÍRITO SANTO

PROTOCOLO DE ASSINATURA



O documento acima foi assinado digitalmente com senha eletrônica através do Protocolo Web, conforme Portaria UFES nº 1.269 de 30/08/2018, por
WANDERLA LUIS SCOPEL - SIAPE 1537668
Departamento de Física - DF/CCE
Em 05/09/2022 às 17:25

Para verificar as assinaturas e visualizar o documento original acesse o link:
<https://api.lepisma.ufes.br/arquivos-assinados/555587?tipoArquivo=O>

“The night is in its darkest just before dawn. But keep your eyes open. If you avert your eyes from the dark, you’ll be blind to the rays of a new day. So keep your eyes open, no matter how dark the night ahead may be.”

Hideaki Sorachi, *Gintama*

Resumo

Nesta tese foram exploradas a aplicabilidade de monocamadas do material ferroelétrico $\alpha\text{-In}_2\text{Se}_3$ na geração fotocatalítica de gás hidrogênio, através de engenharia de band gap, e a transição de fase topológica a partir da oxigenação do material via cálculos *ab initio*, baseados na Teoria do Funcional Densidade (DFT). Para In_2Se_3 pristino, nossos resultados indicam que, através da engenharia de band gap, sob certos níveis de pH, o alinhamento de bandas favorece o uso deste material para atividade fotocatalítica em processos de separação de água. Além disso, motivados por pesquisas recentes relacionadas a transições de fase topológicas em materiais 2D, por engenharia de tensões e incorporação de oxigênio superficial, um estudo sistemático foi empregado para estimar a possibilidade de tal transição neste sistema. Algumas fontes de oxigênio foram consideradas para determinar se esta reação ocorreria de fato: moléculas de O_2 (estados de spin singleto e tripleto), moléculas de H_2O e oxigênio atômico. Nossos resultados sugerem que a adsorção só ocorre para O_2 e oxigênio atômico. Além disso, a análise de energia total para estas fontes indica que não há nenhuma seletividade aparente de sítios de Se ativos, isto é, a adsorção provavelmente ocorre de forma uniforme. A recém-formada camada $\alpha\text{-In}_2\text{Se}_3\text{O}$ apresenta topologia de bandas não-trivial que por sua vez é modulada por um campo elétrico externo aplicado, destacando um efeito de *field-effect switching* da ordem topológica presente.

Abstract

In this thesis, the potential applicability of single layers of ferroelectric $\alpha\text{-In}_2\text{Se}_3$ in photocatalytic hydrogen gas generation, via band gap engineering, and a topological phase transition induced by oxygen incorporation are explored via *ab initio* calculations, based on Density Functional Theory (DFT). For pristine In_2Se_3 , our results indicate that via band gap engineering, under certain pH levels, the band alignment favors the use of this material in photocatalytic activity in water-splitting processes. Furthermore, motivated by recent research related to topological phase transitions in 2D materials by strain engineering and surface oxygen incorporation, a systematic study of the latter was employed to evaluate the possibility of such transition in this system. A handful of oxygen sources were used to determine if such reaction would occur: O_2 molecules (triplet and singlet spin states), H_2O molecules and atomic oxygen. Our findings suggest that adsorption only occurs for singlet O_2 and atomic oxygen. Moreover, total energy analysis for these sources indicate that there is no apparent active Se surface site selectivity, i.e., the adsorption might happen uniformly. The newly formed $\alpha\text{-In}_2\text{Se}_3\text{O}$ layer was shown to present non-trivial band topology which was then modulated by an external applied electric field, highlighting a field-effect switching of the topological order.

List of Figures

- 1.1 Illustration of a photocatalytic water splitting process. A semiconductor in aqueous solution is subject to visible-light irradiation with energy $h\nu \geq E_g$. Photogenerated electron-hole pairs may facilitate hydrogen reduction and oxygen evolution reactions, if recombination is hindered. 4
- 1.2 Schematic of a silicon based solar cell. Image extracted from the Chem-Matters magazine. 4
- 1.3 Band structure evolution of single-layer α - In_2Se_3 under different (a)-(c) compressive biaxial and (d)-(f) tensile uniaxial strais. Figure extracted from Jiang *et al* (2019)^[59]. 5
- 2.1 (a) Evolution of a vector $|u_j\rangle$ in N discrete steps along a closed path. (b) Continuum limit approximation where N steps are taken in infinitesimal increments. (c) Continuous limit where the vectors $|u_j\rangle$ are carried out along a path parameterized by $\lambda \in [0, 1]$. Figure extracted from Vanderbilt (2018)^[70]. 9
- 2.2 Possible Hall effects illustration. Figure extracted from Liu *et al* (2016)^[78]. 14
- 2.3 (a) Haldane model for graphene. The vectors \mathbf{a}_1 and \mathbf{a}_2 connect lattice sites containing orbitals 1 (filled circles) and 2 (open circles). Hopping integrals t_1 and it_2 connect first and second nearest-neighbors, respectively. (b) Reciprocal hexagonal lattice with highlighted high symmetry points. Figure extracted from Vanderbilt (2018)^[70]. 16
- 2.4 Graphene slab energy bands (inset). The bulk gap is crossed by conducting edge states at $k_x = \pi/a$ responsible for a polarized spin current. t characterizes the interaction intensity between neighbors, with $t_2/t = 0.03$. Figure extracted from Kane e Mele (2005)^[85]. 17

- 2.5 (a) Band structures without and (b) with SOC. The dashed line indicates the Fermi level. (c) Diagram illustrating the evolution of p_z and p_{xy} Bi and Se orbitals that compose the conduction and valence bands at the high symmetry point Γ . (d) Edge states projection. Bands in red belong to the bulk and the conducting edge states are evident in Γ as a result of the material's non-trivial topology. Figure extracted and adapted from Zhang *et al* (2009)^[88]. 19
- 2.6 Sketch of possible band structures at the edges of a 2D material, as a function of momentum k along the edges. (a) The Fermi level is crossed an even number of times, characterizing a trivial phase. (b) Odd number of Fermi level crossing, characterizing a non-trivial topological phase robust against small perturbations. Only half the BZ is mapped since TR symmetry implies that the other half $-\pi/a < k < 0$ is its mirror image. Figure extracted from Franz e Molenkamp (2013)^[90]. 22
- 2.7 Wannier charge center evolution \bar{x} as a function of time t in an adiabatic process. The WCCs wrap around an unit circle as t varies from 0 to $T/2$. (a) Odd number of pair exchanges, defining a \mathbb{Z}_2 insulator. (b) WCCs reconnect without exchanging pairs, defining a trivial phase. Figure extracted from Soluyanov (2011)^[100]. 26
- 3.1 Self-consistency cycle sketch. 34
- 4.1 Equivalent rectangular geometric structure and band structure of monolayer α - In_2Se_3 . (a) Side and top view of the monolayer α - In_2Se_3 structure. The dashed lines delimit the unit cells. (b) GGA-PBE calculated band structure and Partial Density of States (PDOS, in the right) for the unstrained α monolayer. The Fermi level is shifted to energy zero. Real space distribution of the Bloch wave functions of (c) VB and (d) CB along the M- Γ path. 41
- 4.2 GGA-PBE calculated band structures (a)-(j) of α - In_2Se_3 for the different values of ε_b . The blue and red curves are Conduction Band (CB) and Valence Band (VB), respectively. The sub-VB state λ is highlighted in orange. All band structure plots are shifted by their respective vacuum level. 42
- 4.3 GGA-PBE (black circle) and HSE06 (red square) calculated band gap *vs.* in-plane biaxial strain. The dashed line is a guide to the eyes. 43

4.4	HSE06 calculated band edges diagrams of 2D α - In_2Se_3 with respect to the vacuum level. The dashed lines represent the H_2O potentials in a $\text{pH} = 0$ solution. The width of the coloured blocks is a guide to the eyes.	44
4.5	Optical absorption spectra of α - In_2Se_3 monolayer in the visible light range for ϵ_b 0, -4 -6, and -8%, based on HSE06 calculations.	45
5.1	(a) Side and top views of the atomic structure of monolayer α - In_2Se_3 , with the electric polarization pointing downwards along the c -axis. (b) Side and top views of its 5×5 supercell with oxygen atoms adsorbed on surface Se atoms. In, Se and O atoms are represented by purple, green and red circles, respectively. The dashed lines delimit one unit cell within the structure. . .	49
5.2	Dissociation reaction path of a O_2 on the surface of monolayer α - In_2Se_3 . .	49
5.3	Phonon dispersion for α - In_2Se_3 with full passivation of Se surface sites by oxygen atoms.	51
5.4	Effective electronic band structures of α - In_2Se_3 with increasing surface oxygen coverage along the M- Γ -K-M high-symmetry path. (a)-(c) Low coverage regime. An indirect-to-direct gap nature transition is observed as oxygen concentration is raised. (d)-(f) High coverage regime. Band inversion occurs and α - $\text{In}_2\text{Se}_3\text{O}$ becomes gapless at maximum concentration. All Fermi levels are shifted to zero energy.	52
5.5	Orbital-resolved electronic band structure of pristine (a)-(d) and fully oxygenated α - In_2Se_3 (e)-(h) split into contributions from each atom. Orbitals are represented by different colors and sizes according to their respective contribution to a given band. The incorporation of oxygen into the system to hybridization and band inversion between $\text{Se}^{(1)}\text{-p}_z$, $\text{In}^{(1)}\text{-s}$, $\text{In}^{(2)}\text{-s}$, $\text{Se}^{(3)}\text{-p}_y$ and $\text{O-p}_{x,y}$ orbitals. All Fermi levels are shifted to zero energy. . .	54
5.6	Band structure of monolayer α - In_2Se_3 (a) without SOC and (b) with SOC. A gap of 61 meV opens up around E_F	55

- 5.7 (a) Evolution of the Wannier centers along k_y which indicate a non-trivial invariant ($\mathbb{Z}_2 = 1$) for the bulk band structure in oxygenated two-dimensional α - In_2Se_3 . The evolution lines cross the arbitrary reference line (blue dashed line parallel to k_y) an odd number of times. (b) Projected edge spectrum (edge along the [100] direction), where \mathbb{Z}_2 topological edge states can be observed in the energy gaps. (c) Band gap as a function of external electric field applied in the out-of-plane direction. The insets show regions where the electric field drives a transition into a normal insulator or into a metallic state. Brown and white curves represent higher and lower spectral weight, respectively. 56
- 6.1 Kinetic pathways of polarization reversal processes in 2D α - $\text{In}_2\text{Se}_3\text{O}$. . . 59

List of Tables

IV.1 Raman Active Phonons for the α phase for different values of ε_b	43
V.1 The binding energies per oxygen atom from different sources: an atomic oxygen source (in a triplet spin state), a O_2 molecule source (in its singlet spin state) and a H_2O molecule.	50

Contents

I	Introduction	2
II	Berry Phases and Topological Insulators	8
2.1	Berry Phase, Connection and Curvature	8
2.1.1	Berry Curvatures and Chern's Theorem	12
2.2	Quantum Hall Effect and Topological Insulators	14
2.3	The \mathbb{Z}_2 Topological Class	20
III	Methodological Fundamentals	28
3.1	The Many-Body Interaction Problem	28
3.2	The Hartree-Fock Approximation	29
3.3	Density Functional Theory	31
3.4	Exchange-Correlation and Hybrid Functionals	34
3.5	Computational Details	36
IV	Single-layer α-In_2Se_3 as a Photocatalyst for H_2O Splitting	38
4.1	Conclusions	46
V	Non-trivial Edge States in Oxygenated Monolayer α-In_2Se_3	47
5.1	Conclusions	56
VI	Final Remarks	58
A	Adiabatic Dynamics	61
B	Wannier Functions	63
C	Second Quantization Formalism	65
3.1	Occupation Number and Fock Space	66

3.2 One and Two-body Representation 68

Bibliography **72**

Chapter I

Introduction

*“I’m about to kill it I can feel it
building up, Blow this building up,
I’ve been sealed enough, My cup
runneth over I done filled it up”*

Rabbit Run, Eminem

The main focus of this thesis is research on electronic properties of layered semiconducting systems whose dimensions are of approximately 1 nm, with emphasis on single layers of the parent bulk material where the van der Waals (vdW) interaction is weak enough to allow inter- and intralayer separation processes, controlled by the general properties and geometry of the material in question. The most prominent and known example of such groundbreaking advances in materials science and condensed matter physics in the development of new generation nanodevices is found in graphene^[1], that represents a new class of materials and, since its successful exfoliation, has offered new insight on the emerging low-dimensionality phenomena.

With its experimental realization in 2004^[1,2], a new branch of solid state physics emerged, directed towards the study and development of devices based on two-dimensional materials (2D) whose properties would allow for their usage as key components in applications that would otherwise be difficult, or even impossible, to obtain with then recent technologies^[2,3]. Owing to its extraordinary properties, graphene was posed as a potential substitute for silicon in high-performance electronic devices. The absence of a band gap, however, may hinder its optoelectronic applications due to its relatively low light absorption^[4,5]. Its use in field-effect transistors (FETs)^[6-8], for instance, is inadequate, which motivates the search for new two-dimensional materials with similar properties and

more appropriate band gaps.

This search led to the discovery of different classes of 2D materials and countless quantum phenomena that arise at the atomic limit, such as massless Dirac fermions in graphene^[9], quantum spin Hall effect^[10], doping-controlled magnetism, topologically protected edge states and applications in quantum computers^[11–14]. Furthermore, an abundance of properties emerges when distinct 2D materials are stacked in order to create heterostructures (lateral or van der Waals) that allow the study of new unique effects such as tunneling and topological currents in graphene/h-BN heterostructures^[15,16].

Among these classes, much attention is given to transition metal dichalcogenides (TMDs) and layered group III₂–IV₃ and V materials, which in general present semiconducting nature with band gaps in the 1-2 eV range, allowing, within a number of other applications, greater electrostatic control and scalability for nanotransistors^[17,18], adjustable optical properties^[19,20], gas detection^[21–23], solar panels and photocatalysts^[24–26], and the possible engineering of newly formed materials through vdW heterostructures^[27]. Despite the constant developments in experimental isolation of 2D semiconductors, still to this day there are hundreds of vdW materials with isolation capability and potential applications in future devices^[28]. In contrast with their bulk counterparts, layered 2D materials, mainly semiconductors, possess extraordinary advantages. Namely, their surface area is larger, resulting in a larger number of active surface sites, enabling a higher photocatalytic activity, for example^[29,30].

Additionally, some materials show good conductivity and superior electronic mobility, which in turn may facilitate the recombination rate of electron-hole pairs generated in a photocatalyst, rendering materials of this kind strong candidates to enhance device efficiency^[31,32]. Recently, monolayer MoS₂, a direct band gap TMD (≈ 1.9 eV), was posed as a potential candidate for use as a cocatalyst in hydrogen evolution reactions (HERs)^[33,34]. For pH levels in the 0-7 range, a single layer of MoS₂ exhibits adequate band alignment with respect to the reduction potential of hydrogen (H⁺/H₂) and oxygen evolution reactions (O₂/H₂O, OERs)^[35–37], an unambiguous condition for water splitting through sunlight processes^[37]. Under photon irradiation with energy larger than the optical gap, a semiconductor may generate electron-hole pairs via excitation of electrons sitting at the valence band maximum (VBM) to the conduction band minimum (CBM)^[38–40]. However, most semiconductors do not possess high photocatalytic activity owing to the fast recombination of pairs, and the use of noble metals such as Pt might still be necessary, greatly increasing the cost of this process. Conversely, the recombination rates of photogener-

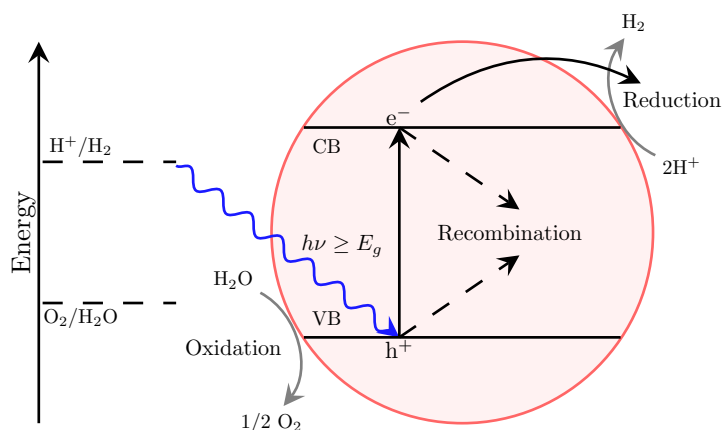


Figure 1.1: Illustration of a photocatalytic water splitting process. A semiconductor in aqueous solution is subject to visible-light irradiation with energy $h\nu \geq E_g$. Photogenerated electron-hole pairs may facilitate hydrogen reduction and oxygen evolution reactions, if recombination is hindered.

ated carriers may be hindered in materials that exhibit intrinsic electric fields^[32], namely layered semiconductors belonging to the M_2X_3 ($M = \text{Al, Ga, In; X} = \text{S, Se, Te}$) family. Other examples of 2D materials with possible optoelectronic applications are group V monolayers, such as antimonene^[41,42], phosphorene^[43,44] and arsenene^[45].

In this regard, as an example, most solar cells (residential and industrial) are based on poly- or monocrystalline silicon consisting of a single semiconducting junction between type-n and type-p Si arranged along the cell's surface. These devices collect a relatively narrow portion of the solar light spectrum, resulting in photovoltaic conversion efficiencies of up to 39%^[46]. More recent technologies began using so-called multijunction cells, where different semiconducting junctions are stacked along the cell and each of these junctions collect different portions of the spectrum, effectively increasing the spectral width as whole, thus reaching conversion efficiencies of up to 50%^[47,48]. However, their use is limited by their high manufacturing cost, leading to the search of alternative lower cost with similar efficacy. One of such alternatives is found in perovskite-based cells with inexpensive cost. Moreover, silicon high synthesis temperatures and thermal annealing are not needed, facilitating its mass production.

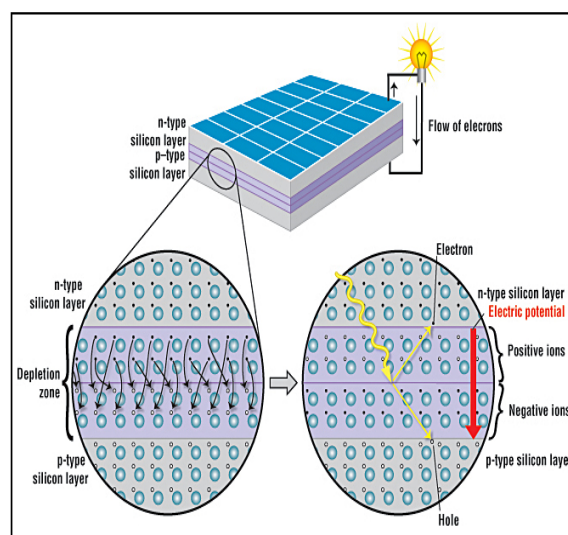


Figure 1.2: Schematic of a silicon based solar cell. Image extracted from the ChemMatters magazine.

Nevertheless, in spite of the low production cost, these cells have a very short lifespan. As such, the field has recently expanded into the use of 2D materials in photovoltaic materials^[25,49], photocatalysts for hydrogen gas generation^[26,50–52] and pollutant degradation, such as Cr(VI)^[51–53].

Another advantage of 2D materials is the relative ease to manipulate and adjust their electronic properties and consequently enhance their photocatalytic performance through external agents, such as atom and molecule adsorption or strain. Strain engineering is a simple concept defined when a crystal is compressed, stretched or sheared, and may be controlled and directed towards various applications and effects, notably photocatalysis and topological phase transitions^[54–58]. Under the context of bi and uniaxial strains, it is possible to induce in this selenide phase transitions of metallic and topological nature. Jiang *et al*^[59] have demonstrated the coexistence of ferroelectricity and non-trivial topological edge states in single layers of α -In₂Se₃ above certain values of strains, as depicted in Fig. 1.3. The system undergoes an indirect-to-direct band gap transition, eventually reaching a metallic state as the applied strain is increased to a critical value, measured in relation to the optimized lattice parameter, after which the manifestation of a band inversion process is evident, an imprint of a phase transition of topological nature that is subsequently confirmed by calculating the \mathbb{Z}_2 invariant $\nu = 1$ (more details regarding these claims will be explored in the following chapter). Besides,

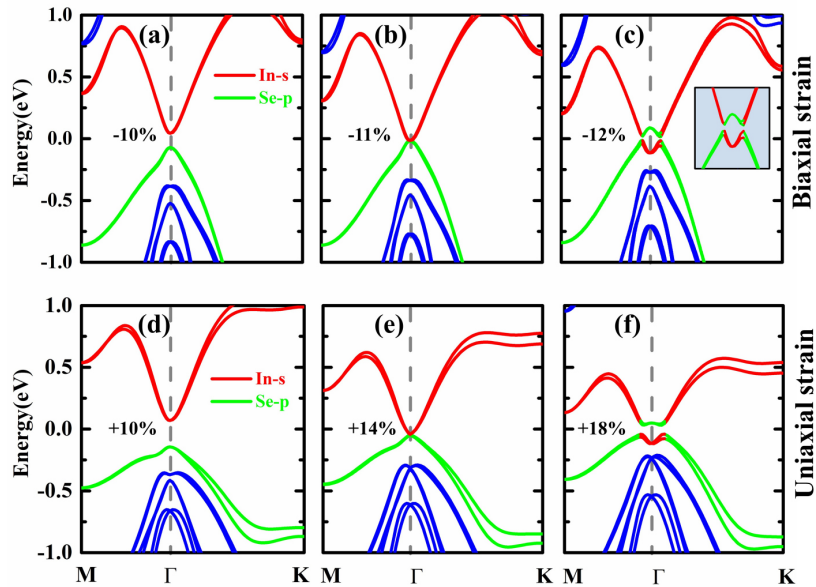


Figure 1.3: Band structure evolution of single-layer α -In₂Se₃ under different (a)-(c) compressive biaxial and (d)-(f) tensile uniaxial strains. Figure extracted from Jiang *et al* (2019)^[59].

recent applications involving a ferroelectric control of the non-trivial topological state of

β -antimonene/ α -In₂Se₃ heterobilayers were reported^[60], where the authors observed that a specific ordering of the electronic polarization in the selenide layer drives the system into a non-trivial state, whereas an inversion of P by an external electric field returns the system into a trivial insulating state. In light of these and other reported findings, it is of particular interest for this work to thoroughly investigate the properties of this selenide, from basic structural details and semiconducting character to changes of the former cause by external strains and surface atom adsorption.

Findings of this nature motivate the continuous search for different materials where not only the single-layer separation is obtainable by any means adequate to the experiment, given the interlayer van der Waals interaction is weak enough, but also possess high photoactivity and/or topologically protected states. In particular, we turn our attention to the layered group III₂IV₃ semiconductor, In₂Se₃, that has been extensively studied for decades due to its numerous distinct crystalline phases (commonly named α , β , β' , γ , δ , among others), complex phase diagrams and optoelectronic applications, prominently as photodetectors^[61–64], phase-change memories (P-RAMs)^[65,66] and photocatalysts^[26,32]. Moreover, as a result of its noncentrosymmetric structural configuration, a spontaneous electronic polarization (both in and out-of-plane) reversible by an external electric field arises, rendering this material a ferroelectric semiconductor¹, in addition to experimental evidence of piezoelectricity, that may be explored for applications in sensors given its photosensitivity^[67–69].

In the following chapters, I will introduce the works developed throughout my doctorate, ranging from biaxial strain effects to surface adsorption of oxygen atoms in single layers of α -In₂Se₃ and how these react under such conditions. The phenomena herein mentioned, and in general belonging to low-dimensionality physics share the same limitation: the unsolvability of the exact Schrödinger for many body systems. As such, I will review a powerful approximative theory that on which this thesis is carried out. The chapters are disposed as follows: Chapter II will be dedicated to the classification of non-trivial topological states under the context of Berry phases and in Chapter III I will review the fundamentals of Density Functional Theory (DFT) and numerical methods associated with it. Chapter IV will be dedicated to the study of feasibility of In₂Se₃ as a photocatalyst for hydrogen gas generation by strain engineering; Chapter V refers to

¹A material is said to be ferroelectric if, and only if, its intrinsic polarization is reversible. This means that the initial and final (inverted) phases are degenerate and the external electric field must cause the system to transition to a less stable, centrosymmetric intermediate phase. An excellent example can be found in Nat. Comm. 8, 2017^[67].

the emergence of non-trivial edge states in this very material as a result of oxygen atom adsorption on its surface and how this topological phase transition may be controlled by its spontaneous electric polarization. Thus, the chapters devoted to our results may be read in any order without loss of information, as they refer to published works that address distinct subjects, despite the material in question being essentially the same.

Chapter II

Berry Phases and Topological Insulators

I will abstain from abstract mathematical details that lie outside the scope of this thesis, unless in cases where its use is necessary to understand some physical concept. In general terms, a Berry phase γ is defined as a geometric phase angle describing the global evolution of a complex vector as it is carried out around a path in its own vector space^[70], usually applicable in cyclic processes where the changes in said vector are adiabatic. Due to the probabilistic nature of quantum theory, that is, physical observables involve expectation values over a set of basis functions in which phase factors cancel out, it is natural to disregard them as arbitrary. However, Berry phases are intimately connected to measurable physical phenomena and are widely used in molecular physics^[71] and notably in condensed matter physics, both in the modern theory of electronic polarization and in the theoretical development of topological insulators, whose classifications are directly attached to γ .

2.1 Berry Phase, Connection and Curvature

As previously mentioned, a Berry phase is a global phase property acquired by the system when it is subject to an adiabatic cyclic process and may be defined as the inner product of neighboring Bloch states in the k vector space. This means that in a given quantum system in an eigenstate $|u_n\rangle$, an adiabatic evolution of the Hamiltonian preserves the system in the same eigenstate, with a phase vector with contributions from the time evolution of $|u_n\rangle$ and its variation inherited from deforming \mathcal{H} . We can depict

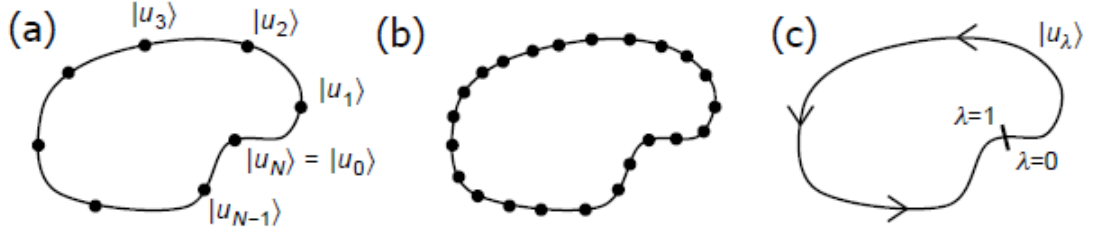


Figure 2.1: (a) Evolution of a vector $|u_j\rangle$ in N discrete steps along a closed path. (b) Continuum limit approximation where N steps are taken in infinitesimal increments. (c) Continuous limit where the vectors $|u_j\rangle$ are carried out along a path parameterized by $\lambda \in [0, 1]$. Figure extracted from Vanderbilt (2018)^[70].

this process by considering a set of states $|u_j\rangle$, with $j = 0, 1, \dots, N - 1$, of some complex vector transversing a close path along the base u_j in a way that the vectors $|u_0\rangle$ and $|u_N\rangle$ are identical (Fig. 2.1). The Berry phase γ is then defined as^[70,72]

$$\gamma = -\text{Im} \ln \left[\langle u_0 | u_1 \rangle \langle u_1 | u_2 \rangle \dots \langle u_{N-1} | u_0 \rangle \right], \quad (2.1)$$

where the individual inner products must be real and positive, and the magnitude of the vectors is neglected by definition, since for a complex number $z = |z|e^{i\theta}$. Furthermore, it is noted that the definition 2.1 is *independent* of the choices of the individual phases of each vector; that is, the Berry phase is ***invariant under gauge transformations***, which means that we may introduce a modified base, related to the previous one by a real phase β_j , such that

$$|\tilde{u}_j\rangle = e^{-i\beta_j} |u_j\rangle. \quad (2.2)$$

Since the definition 2.1 involves inner products, the phase factors cancel out and the value of γ is unchanged when we use the new base. Such property combined with the fact that we are dealing with cyclic processes render Berry phases observables of the system. A question that may arise at this point is whether or not γ is dependent of the path to be transversed along the vector space, however, as will become explicit shortly in the generalization to the continuous case, γ is independent of choice, as long as it is done slow enough to preserve the adiabatic approximation^[72].

We may now generalize the definition of a Berry phase to the continuous limit, where the density of points along the path C is increased, parameterized by a parameter λ in such a way that the vectors $|u_\lambda\rangle$ are carried out along C as λ varies from 0 to 1 (Fig. 2.1c), and each step between neighboring vectors is taken in infinitesimal increments $d\lambda$, so that $|u_\lambda\rangle$ is a smooth and differentiable function in λ . Recurring to the definition 2.1

and expanding $|u_{\lambda+d\lambda}\rangle$ in a power series, we obtain^[70]

$$\ln \langle u_\lambda | u_{\lambda+d\lambda} \rangle = \ln \langle u_\lambda | \left(|u_\lambda\rangle + d\lambda \frac{|u_\lambda\rangle}{d\lambda} + \mathcal{O}(\lambda^2) \right) \quad (2.3)$$

$$= \ln(1 + d\lambda \langle u_\lambda | \partial_\lambda u_\lambda \rangle + \mathcal{O}(\lambda^2)). \quad (2.4)$$

Since $\lambda \ll 1$, we may neglect higher order terms and approximate the above result as $d\lambda \langle u_\lambda | \partial_\lambda u_\lambda \rangle$. Thus, the definition of γ becomes

$$\gamma = -\text{Im} \oint_C d\lambda \langle u_\lambda | \partial_\lambda u_\lambda \rangle.$$

In this case, $\langle u_\lambda | \partial_\lambda u_\lambda \rangle$ is a purely imaginary quantity, since $2\text{Re}(\langle u_\lambda | \partial_\lambda u_\lambda \rangle) = 0$. Thus, we obtain the (one dimensional) expression derived by Berry in his original work:

$$\boxed{\gamma = i \oint_C d\lambda \langle u_\lambda | \partial_\lambda u_\lambda \rangle.} \quad (2.5)$$

The integrand to the right is commonly named Berry's connection or potential (\mathcal{A}) in analogy to the electromagnetic vector potential, so that we can rewrite γ as the line integral of \mathcal{A} throughout C . Naturally, in the continuous limit the Berry phase must remain invariant under gauge transformations, but the connection is not. If we suppose the same previous modified base $|\tilde{u}\rangle$, it is easy to see that

$$\tilde{\mathcal{A}}(\lambda) = \langle \tilde{u}_\lambda | i\partial_\lambda | \tilde{u}_\lambda \rangle = \langle u_\lambda | i\partial_\lambda | u_\lambda \rangle + \beta'(\lambda),$$

i.e., the connection \mathcal{A} transforms according to $\tilde{\mathcal{A}}(\lambda) = \mathcal{A}(\lambda) + \beta'(\lambda)$. Using this relation combined with the fact that the initial and final states must be identical, we would arrive at $\beta(1) = \beta(0) + 2\pi m$ with m integer, so that the Berry phase γ is invariant under gauge transformations *modulo* 2π :

$$\tilde{\gamma} = \gamma + 2\pi m. \quad (2.6)$$

At a first glance, Eq. 2.6 seems simple and intuitive, but its meaning is profound. Each and every transformation of the form $\tilde{\mathcal{A}}(\lambda) = \mathcal{A}(\lambda) + \beta'(\lambda)$ in a closed path can be topologically classified according to the number m , a winding number specifying how many times the phase factor $e^{-i\beta}$ is carried out along the unit circle in the imaginary plane as λ circles the path C ^[70]; this conclusion is very similar to Chern's theorem, to be introduced at the end of this section.

Note that thus far we have used a one dimensional path and there is no explicit time dependence of the vectors $|u_\lambda\rangle$; the generalization to a three-dimensional space is direct (we replace $\partial_\lambda \rightarrow \nabla$ and $d\lambda$ by an equivalent increment, such as the position vector \mathbf{r} or wave vector \mathbf{k}) and the approach taking into account a time dependence in t requires a bit more caution, and at this point I will use Berry's own development based on Born-Fock's adiabatic theorem (1928)^[73].

Let $\mathcal{H}(t)$ a Hamiltonian dependent of variable parameters $\mathbf{R} = (x, y, \dots)$ as the system transverses a path C between times $t = 0$ and $t = T$ (T is assumed to be large enough to preserve the adiabatic approximation), so that $\mathbf{R}(T) = \mathbf{R}(0)$. The time evolution of an eigenstate $|u_n(t)\rangle$ will satisfy the eigenvalue equation

$$\mathcal{H}(\mathbf{R}) |u_n(\mathbf{R})\rangle = E_n |u_n(\mathbf{R})\rangle, \quad (2.7)$$

in which there is no relation between the kets in \mathbf{R} . Arbitrary choices of differentiable phases may be done as long as the vectors $|u_n(\mathbf{R}(t))\rangle$ are single-valued¹ in C . Thus, a system in an eigenstate $|u_n(\mathbf{R}(0))\rangle$ evolves adiabatically with \mathcal{H} and after a time interval t will be in an eigenstate $|u_n(\mathbf{R}(t))\rangle$. As such, we may then express the wave function $|\Psi(t)\rangle$ as

$$|\Psi(t)\rangle = \exp\left[\frac{1}{i\hbar} \int_0^t dt' E_n(\mathbf{R}(t'))\right] e^{i\gamma_n(t)} |u_n(\mathbf{R}(t))\rangle, \quad (2.8)$$

where the first exponential is the usual dynamic phase factor arising from the expansion coefficients of $|\Psi(t)\rangle$ in the base spanned by $\{|u_n\rangle\}$. The second phase factor is non-integrable, i.e., γ_n cannot be expressed as a function of \mathbf{R} and is not single-valued in a given path transversed by the system along the time interval $t \in [0, T]$ ^[72]. Therefore, the wave equation for $|\Psi(t)\rangle$ results (after some algebra - see Appendix A) in

$$\dot{\gamma}_n(t) = i \langle u_n(\mathbf{R}(t)) | \nabla_{\mathbf{R}} u_n(\mathbf{R}(t)) \rangle \cdot \dot{\mathbf{R}}(t), \quad (2.9)$$

from which we determine the change in geometric phase (Berry's phase) in an adiabatic cyclic process along a path C as^[72]

$$\boxed{\gamma_n(C) = i \oint_C d\mathbf{R} \cdot \langle u_n(\mathbf{R}) | \nabla_{\mathbf{R}} u_n(\mathbf{R}) \rangle}, \quad (2.10)$$

equal to the previous result, but with a subtlety: the Berry phase in the time evolution of

¹A function $f(x)$ is single-valued if there is a single value of f for a given x .

$|\Psi(t)\rangle$ is a function *only* of the transversed path in parameter space, and is *independent* of the rate at which it is carried out, as long as - reiterating - the parameter $\mathbf{R}(t)$ evolves adiabatically and for this reason γ is said to be a geometric phase.

2.1.1 Berry Curvatures and Chern's Theorem

The expression found for γ_n involves the product of a vector in the form of $|\nabla_{\mathbf{R}}u_n(\mathbf{R})\rangle$ and its calculation can be cumbersome. In this context, let us consider a two-dimensional space parameterized by $\mathbf{R} = (x, y)$ such that the Berry connection is generalized to a two-dimensional vector $\mathcal{A} = (A_x, A_y)$ and the vectorial evolution is carried out through a path C delimiting a curve S . Still in our analogy with the magnetic potential vector, it is inevitable to establish the rotational of \mathcal{A} , known as the **Berry curvature**, $\Omega(\mathbf{R})$:

$$\boxed{\Omega(\mathbf{R}) = \nabla_{\mathbf{R}} \times \mathcal{A}(\mathbf{R}) = i \left[\langle \partial_x u_n(\mathbf{R}) | \partial_y u_n(\mathbf{R}) \rangle - \langle \partial_y u_n(\mathbf{R}) | \partial_x u_n(\mathbf{R}) \rangle \right]} \quad (2.11)$$

We may think of the curvature like a magnetic field; it is a local quantity that is unambiguous of the path choice embed in the connection, so that Ω is itself invariant under gauge transformations, since the rotational of a gradient is null. Given the form of Ω , the use of Stokes' theorem follows immediately to relate the flux Φ_S that crosses a curve S to the Berry phase along the path C :

$$\Phi_S = \int_S d\mathbf{S} \cdot \Omega(\mathbf{R}) = \oint_C d\mathbf{R} \cdot \mathcal{A}(\mathbf{R}) = \gamma_C. \quad (2.12)$$

In other words, the flux Φ_S is equal to the Berry phase along its contour. This is equivalent to saying that if we were to divide region S in infinitesimal area elements and calculate the circulation of \mathcal{A} through S , the result would simply be the Berry phase calculated along C . This conclusion, together with the *modulo* 2π definition of Berry's phase, is intimately connected to the famous **Chern Theorem**^{[74]2}, postulated in 1944: *the sum of the gaussian curvature of a two-dimensional manifold is 2π times an integer number C , i.e.,*

$$\boxed{\oint_S d\mathbf{S} \cdot \Omega = 2\pi C.} \quad (2.13)$$

The integer C is known as the surface's Chern number or index and may be considered as a topological invariant of the states manifold $|u_{\mathbf{R}}\rangle$ that transverse S ^[70]. This form

²The original theorem is a generalization of Gauss-Bonnet theorem of differential geometry and its proof is *far* beyond the scope of this work.

of Chern's theorem was found by B. Simon in his work connecting Berry's and Thouless *et al* in 1983^[75]. Therein, Simon attributed the integral of Berry's curvature associated to the Brillouin zone (BZ) as a Thouless-Komoto-Nightingale-den-Nijs (TKNN) invariant, that provides both a concrete explanation for the quantum Hall effect and the possibility of existence for the Hall conductivity in the absence of external magnetic fields, which is today known as the anomalous quantum Hall effect^[76].

To this point, some questions may have been posed regarding the definitions of γ and Ω : what happens when the varying parameters are, for instance, the wave vector \mathbf{k} of Bloch states $|\psi_{n\mathbf{k}}\rangle$ with band index n that describe the parameter space along the BZ? If Berry curvatures do exist in a crystal of interest (non-zero Chern number), what are its sources?

It is noted that in cases where the Chern number is non-zero, it is *impossible* to construct a continuous smooth gauge along the entire BZ; this becomes clear when we calculate Eq. 2.13 in a closed path encompassing the Brillouin zone, assuming $C \neq 0$ in a time reversal symmetric system: we would arrive at a non-zero number, since by definition $\Omega_n(\mathbf{k}) = -\Omega_n(-\mathbf{k})$ and any quantities involving a closed integral of the curvature along the BZ equals zero, contradicting our assumption. This is the equivalent of the inability to construct a continuous gauge so that the wave functions are smooth in all momentum space.

We then infer that Berry's phase and curvature can only be computed in cases where the Hamiltonian describing the system has a gap. In other words, the Chern number can only be calculated for isolated bands that do not touch. This is a significant restriction, given that in crystalline materials band degeneracy in high symmetry points is common. In materials where bands touch, the Berry phase is undefined; in points where this occurs the wave functions have non-analytical dependence on \mathbf{k} . This concept is again more easily understood when we in fact calculate $\Omega_n(\mathbf{k})$. Given the system's periodicity, the two-dimensional BZ is, by definition, a torus and as such has no borders; when the curvature is integrated we are met with a topological obstruction to Stokes' theorem, and thus we conclude that if there are indeed sources of Berry curvatures throughout the BZ, they cannot be defined in these points. Therefore, we can imply that sources Berry curvatures Ω_n are gap closings along the BZ, defining a non-trivial topology, i.e., C is non-zero. Gap closings in high symmetry points translate in metallic degenerate states that are topologically protected against continuous deformations, and materials that present this property are generally known as topological insulators or quantum spin

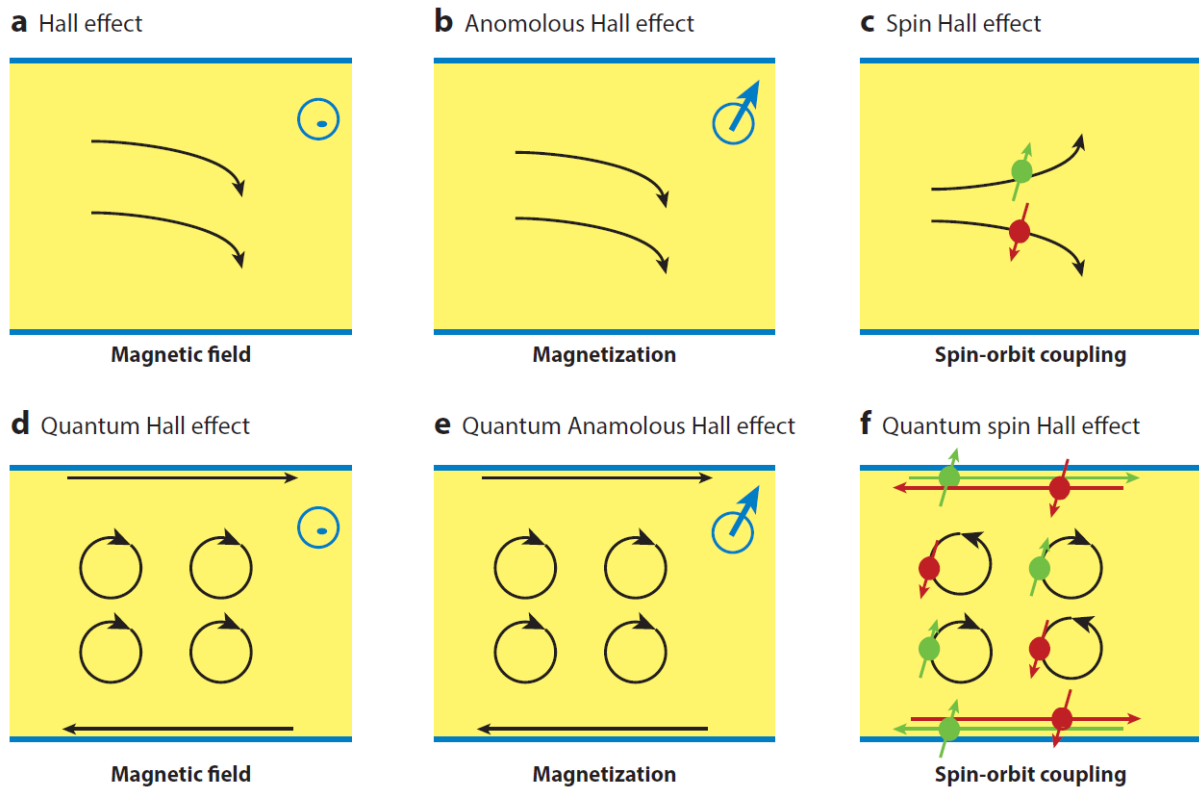


Figure 2.2: Possible Hall effects illustration. Figure extracted from Liu *et al* (2016)^[78].

Hall insulators.

2.2 Quantum Hall Effect and Topological Insulators

Over a century ago, Hall observed the appearance of a transversal potential difference along a non-magnetic conductor under an applied external magnetic field perpendicular to the material due to changes in the trajectory of electrons, known today as the Hall effect^[77] (Fig. 2.2a). In a two-dimensional electron gas in low temperatures and under high magnetic fields (quantum limit), the Hall conductance is quantized in units of e^2/h (also known as the Klitzing constant, where e is the electron charge and h Planck's constant) whereas the longitudinal resistance goes to zero, describing the integer Hall effect (IQH). Electrons in this system would present edge states with chirality and only propagate along the edges of the material, while every other state is well localized^[78,79]. One year after his discovery, Hall observed that the “Hall voltage” in ferromagnetic metals was around 10 times larger than in non-magnetic materials and is dependent on the system's magnetization; this effect is known as the anomalous Hall effect (Fig. 2.2b). With the discovery of IQH, the search for the manifestation of any quantum analogue of the anomalous effect was motivated. Over the course of a century, researchers questioned whether or not

the quantization of the Hall conductance in the absence of an external magnetic field is possible. The first observation of a quantum Hall effect was reported by Klitzing *et al*^[80]. In this work, the authors measured the Hall resistivity in metallic oxide semiconducting transistors (MOSFETs) within the quantum limit and reported that the conductivity σ_{xy} was quantized in units of e^2/h . In subsequent experimental works, researchers were driven to determine if this effect is dependent of sample geometry and impurity concentration. In this scope, Paalanen *et al*^[81] demonstrated that in a two-dimensional electron gas in GaAs–Al_xGa_{1-x}As heterojunctions the Hall effect quantization is well defined regardless of system geometry and up to a certain degree of disorder. In that same year, Thouless and collaborators demonstrated that the Hall conductance calculated in a system with M filled bands would be given by a topological invariant (first Chern number $C \in \mathbb{Z}$) obtained from the net Berry curvature flux as \mathbf{k} varies in the BZ, multiplied by some universal constant^[78,82]:

$$\sigma_H = \frac{e^2}{h} \frac{1}{2\pi} \int_{\text{occ.}} d^2\mathbf{k} \cdot \boldsymbol{\Omega}(\mathbf{k}). \quad (2.14)$$

The first model to explain the Hall conductance quantization in the absence of an external magnetic field for spinless electrons was proposed by F. M. Haldane in 1988^[83]. To replicate a quantum Hall state there must exist a time reversal symmetry (\mathcal{T} , TRS) breaking, that in preceding works was caused by a magnetic field. The model is based on a tight-binding³ Hamiltonian of a two-dimensional hexagonal lattice, such as graphene or boron nitrate, with the addition of a complex hopping term between second-neighbors. The Hamiltonian describing the system takes the form^[70,83,84]

$$\mathcal{H}_{IQH} = M \sum_i (-1)^{\tau_i} c_i^\dagger c_i + t_1 \sum_{\langle ij \rangle} (c_i^\dagger c_j + \text{h.c.}) + t_2 \sum_{\langle\langle ij \rangle\rangle} (ic_i^\dagger c_j + \text{h.c.}), \quad (2.15)$$

where i, j are carried across all lattice sites, $\tau_i = \{1, 2\}$ is the sublattice index, t_1 is the hopping amplitude between first-neighbors $\langle ij \rangle$, t_2 is the hopping amplitude between second nearest-neighbors in a given direction and h.c. is a hermitian conjugate term describing corresponding amplitudes in the opposite directions; the latter guarantees the breaking of TRS due to changes in signs and is responsible for the emergence of a non-trivial topology described by a non-zero Chern number⁴. Even with its apparent simplicity,

³The tight-binding method is based on electronic structure calculations using a set of localized wave functions for each atomic site describing electrons in a periodic potential, i.e., in a crystal. In general, the system's Hamiltonian is split into different contributions: an atomic Hamiltonian and a contribution for the total potential treated as a small perturbation resulting from the overlap of wave functions of isolated atoms, so that only first-neighbor interactions are taken into account.

⁴Materials presenting integer quantum Hall effect (IQH) are commonly referred to as Chern insulators

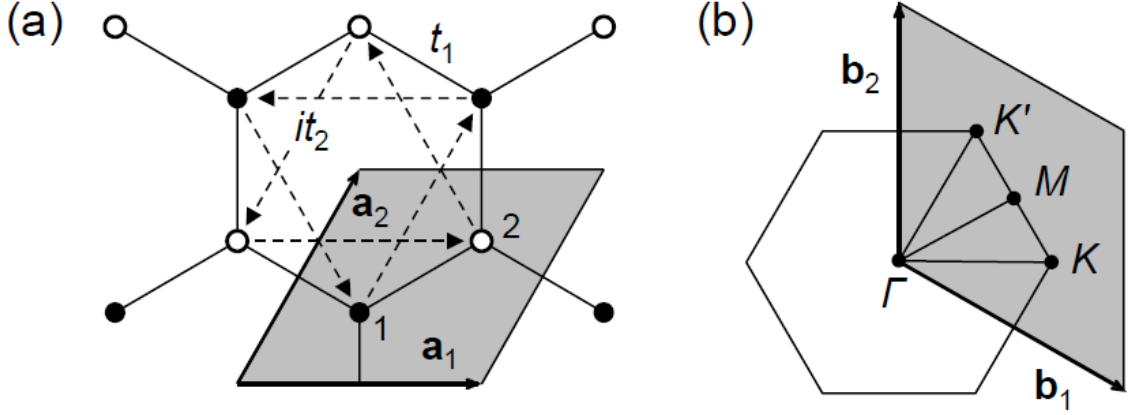


Figure 2.3: (a) Haldane model for graphene. The vectors \mathbf{a}_1 and \mathbf{a}_2 connect lattice sites containing orbitals 1 (filled circles) and 2 (open circles). Hopping integrals t_1 and it_2 connect first and second nearest-neighbors, respectively. (b) Reciprocal hexagonal lattice with highlighted high symmetry points. Figure extracted from Vanderbilt (2018)^[70].

Haldane's model is of extreme importance and is recurrently used in literature, since it admits analytical solutions of the form^[70,83]

$$E_{\mathbf{k}} = \pm \begin{cases} M - 3\sqrt{3}t_2 & \text{em } K, \\ M + 3\sqrt{3}t_2 & \text{em } K'. \end{cases} \quad (2.16)$$

When $t_2 = 0$ the states in K and K' (Fig. 2.3) are degenerate due to \mathcal{T} and define a trivial insulating phase, i.e., no bands touch across all BZ. However, as $t_2 \neq 0$, the gaps in high symmetry points become asymmetrical and the connection between states generated by the hopping term and those generated by the trivial insulating phase cannot be made in a smooth manner without passing through a critical point where the gap vanishes, separating them in topologically distinct fundamental states. Furthermore, in temperatures much smaller than the gap order, the analytical nature of the solutions and characteristics of the model lead to a quantized Hall conductivity $\sigma_{xy} = \pm e^2/h$ ^[85].

Despite being the first observation of a topological phase of matter, the conditions for the manifestation of the quantum Hall effect are specific: very low temperatures and high external applied magnetic fields to ensure TR symmetry breaking. The model proposed by Haldane is a good starting point for the realization of a QAH in the absence of an applied field; however, for over two decades this effect in materials was not observed. Only in 2005 Kane and Mele^[85] and Bernevig e Zhang^[86] independently proposed a theoretical model for the presence of a quantum spin Hall effect in two-dimensional systems, due to the classification by a topological invariant $C \neq 0$.

specifically in graphene and GaAs. The authors relied on the condition that the spin-orbit coupling (SOC) would give rise to the spin Hall effect (SHE, Fig. 2.2e). Unlike the charge Hall effect, in materials with SOC electrons with opposite spin polarizations are deflected in opposite directions, leading to spin accumulation at the edges. Contrary to QHE, the quantum spin Hall effect (QSE, Fig. 2.2f) does not require breaking of TR symmetry and may occur in semiconductors in the absence of an applied field. In fact, the spin-orbit coupling *guarantees* that TRS is preserved and leads to a topologically distinct phase from a trivial insulator^[85], in which similarly to QHE, charge and spin currents can be transported by metallic edge states.

The model is based on Haldane's model with the premise that conducting edge states are also present in graphene, where a tight-binding Hamiltonian similar to that of Eq. 2.15 is introduced, only now the hopping term between second neighbors is given by a product that connects them by a spin-dependent amplitude^[85]:

$$\mathcal{H}_{QSH} = \sum_{\langle ij \rangle \alpha} t_1 c_{i\alpha}^\dagger c_{j\alpha} + \sum_{\langle\langle ij \rangle\rangle \alpha\beta} it_2 \nu_{ij} \sigma_{\alpha\beta}^z c_{i\alpha}^\dagger c_{j\beta}, \quad (2.17)$$

where $\nu_{ij} = -\nu_{ji} = \pm 1$, depending on the \mathbf{d}_1 and \mathbf{d}_2 bond orientation that an electron crosses when going from a site j to a site i according to the direction (left or right) that it moves to between the bonds and $\sigma_{\alpha\beta}^z$ is a Pauli matrix. The solution of Eq. 2.17 leads to a band structure (Fig. 2.4) with a bulk gap and emergent conducting edge states at

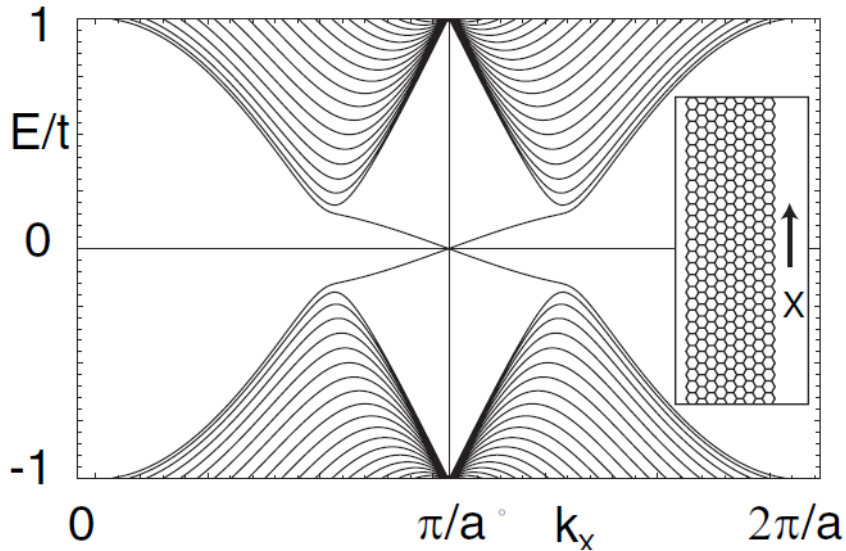


Figure 2.4: Graphene slab energy bands (inset). The bulk gap is crossed by conducting edge states at $k_x = \pi/a$ responsible for a polarized spin current. t characterizes the interaction intensity between neighbors, with $t_2/t = 0.03$. Figure extracted from Kane e Mele (2005)^[85].

the high symmetry points K and K' , and the authors argue that these are non-quiral states, as is the case for the QHE, but are “spin filtered”, in the sense that electrons with opposite spins propagate in opposite directions, similar to the charge Hall effect. Even with the theoretical prediction of metallic edge states and topological properties in graphene, this effect remains unobserved. Nevertheless, given the possibility of obtaining a topological phase in materials without extreme conditions and only spin-orbit coupling, this seminal work led to the discovery of topological insulators, and their first observation was confirmed by Bernevig *et al* in HgTe/CdTe quantum wells^[87] above a critical thickness $d > d_c$, and in this and subsequent works, the general mechanism for topological insulators was discovered, known as band inversion. In most semiconductors, the conduction band is formed by s orbitals, while the valence band is formed by p orbitals; in HgTe, the spin-orbit coupling is strong enough to invert the character of bands above d_c , i.e., the bands cross and CB exhibits VB contributions, and vice-versa. Usually this effect is easily observed in electronic band structure calculations, however it is not always the case. I will use as an example Bi₂Se₃, a widely studied natural topological insulator^[88,89]. Fig. 2.5 shows the electronic structure of monolayer Bi₂Se₃ obtained by Density Functional Theory (DFT). The band structures with and without spin polarization are shown in Fig. 2.5a and 2.5b, respectively. As is typical for semiconductors, the conduction (in blue) and valence (in red) bands are attributed to s and p orbitals, respectively. As SOC is turned on, the conduction (valence) band is shifted relative to the valence (conduction) band, resulting in a change of character between CB and CB and in the process of band inversion at the center of the Brillouin zone, characteristic of materials exhibiting non-trivial topology.

Fig. 2.5c schematically summarizes the band inversion process. At stage (I) only the chemical bond between Bi and Se atoms is considered, in which the parities $|+, -\rangle$ of all five eigenstates are well defined. As we take into account the crystalline field effect, the degeneracy between p_z and $p_{x,y}$ orbitals is lifted and the band character around the Fermi level is predominantly that of p_z orbitals. When SOC effects are included in stage (III), the orbital angular and spin momenta are mixed, while the total angular momentum is preserved; this results in a repulsion between states $|p1_z; + \uparrow\rangle$ and $|p1_{x+iy}; + \downarrow\rangle$, and similar combinations⁵. As a consequence, the $|p1_z; + \uparrow, \downarrow\rangle$ Bi orbitals are shifted to energy levels below E_F , whereas $|p2_z; - \uparrow, \downarrow\rangle$ Se orbitals are shifted to energy levels above E_F . If the spin-orbit coupling is strong enough, the parity of the inverted states is itself inverted,

⁵Note that the spin-orbit coupling does not act on s orbitals since their orbital quantum number l is zero.

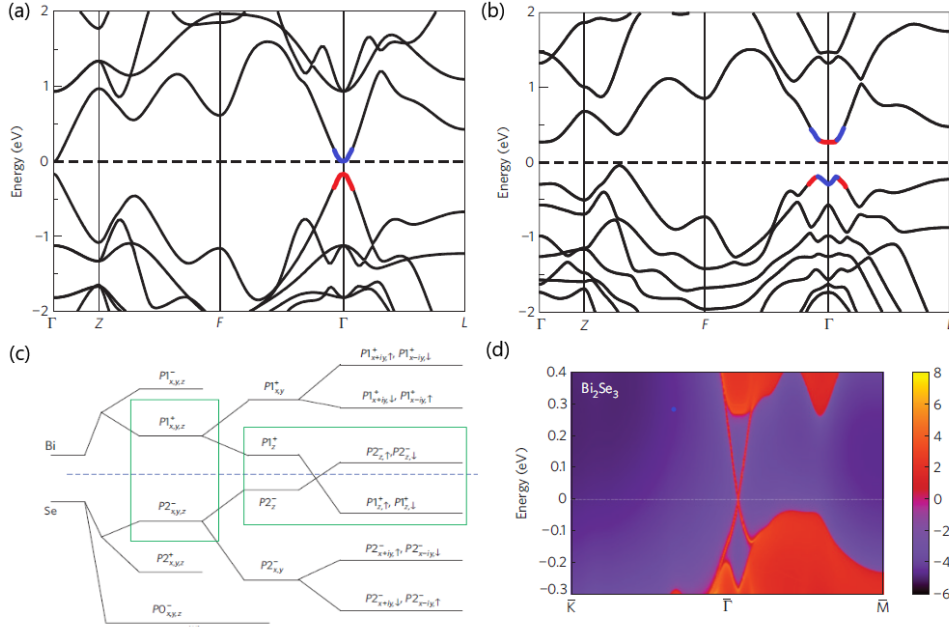


Figure 2.5: (a) Band structures without and (b) with SOC. The dashed line indicates the Fermi level. (c) Diagram illustrating the evolution of p_z and p_{xy} Bi and Se orbitals that compose the conduction and valence bands at the high symmetry point Γ . (d) Edge states projection. Bands in red belong to the bulk and the conducting edge states are evident in Γ as a result of the material's non-trivial topology. Figure extracted and adapted from Zhang *et al* (2009)^[88].

resulting in states lying within the bulk gap with non-trivial topology, confirmed by the presence of conducting edge states, as shown in Fig. 2.5d.

Although the inversion process is a characteristic and a good indicative for non-trivial topology, the *only* way to guaranteed that a material is indeed a TI is through the calculation of its topological invariant, and the \mathbb{Z}_2 classification will be explored in the next section.

Topology is a branch of mathematics that deals with geometric properties of objects that are insensitive to continuous smooth deformations. The most didactic example is of two-dimensional closed surfaces in three dimensions. A sphere may be continuously deformed into different shapes, such as a disc or a bowl, but cannot be smoothly deformed into the surface of a doughnut without there being a critical event, in this case a hole opening. A sphere and a doughnut are distinguished by a distinct topological invariant, known as a *genus*, g , that in essence counts the number of holes in an object. Since an integer cannot be deformed smoothly and continuously, surfaces with distinct *genus* *cannot be* deformed into each other and therefore are said to be topologically distinct. In this context, a tea-cup and a doughnut ($g = 1$) belong to the same topological class, while a sphere or an ellipse belong to a different class ($g = 0$). The Chern theorem presented

earlier is a generalization of the Gauss-Bonnet theorem, which states that the integral of a gaussian curvature K over a surface S defines an integer topological invariant $\chi = 2 - 2g$. In other words, topology classifies objects according to their shapes and their details are of little importance. From a physical standpoint, we may classify topologically distinct Hamiltonians, describing distinct electronic phases. Two insulators are said to belong to the same topological class if their Hamiltonians can be adiabatically connected in a way that two bands *never touch throughout the mapping of the Brillouin zone*, in analogy to the *genus* classification^[70,84,90]. Under this pretext, connecting topologically distinct insulators necessarily involve a phase transition of quantum nature in which the bulk gap closes^[90].

In general, a topological insulator may be defined as a time reversal invariant material that behaves as an insulator in its interior (bulk) and possesses topologically protected conducting states in its surface or edges, whose most striking property is the feasibility of dissipationless electronic conduction^[91] and may be characterized by *some* topological index, for example (but not necessarily) the Chern number, C . Being “TR invariant” means that throughout all the adiabatic process the \mathcal{T} symmetry is preserved. In a more rigorous manner, we may classify a TI as an insulator whose Hamiltonian cannot be adiabatically connected to the atomic limit without a bulk gap closing, since otherwise a change of the topological invariant would be impossible^[79] and the material would be classified as trivial. As a qualitative example, in an interface between materials of distinct classifications, such as a material-vacuum interface (trivial by definition), the Hamiltonian of both systems cannot be smoothly connected. There will necessarily be a gap closing and consequent emergence of conducting surface states that are robust against continuous deformations.

2.3 The \mathbb{Z}_2 Topological Class

The fact that the spin-orbit coupling guarantees the system is \mathcal{T} -invariant suggests we may classify it with a new topological invariant $\nu \in \mathbb{Z}_2$. In addition, the robustness of edge states of a QSH indicate that the classification of such insulator differs from that of a Chern insulator^[90]. The requirement for time reversal invariance is a good indicative that this invariant is attached to \mathcal{T} and its analysis may prove fruitful.

Time reversal is an operation that takes the complex conjugate of an eigenstate of a particle and reverts its spin, and is described by an antiunitary operator $\Theta =$

$\exp(i\pi S_y/\hbar)K$, where S_y is the spin operator and K represents complex conjugation^[90,92]. For fermions, Θ has the property $\Theta^2 = -1$. From Kramers theorem, it follows that if a Hamiltonian is \mathcal{T} -invariant, all of its eigenstates are at least doubly degenerate. In absence of SOC, the degeneracy of the eigenstates is a consequence of Pauli's exclusion principle; however, in the presence of SOC this degeneracy is lifted and bands come in Kramer pairs \mathbf{k} and $-\mathbf{k}$, and its implications are not trivial. More precisely, \mathcal{T} -invariant Bloch Hamiltonians must satisfy

$$\Theta\mathcal{H}(\mathbf{k})\Theta^{-1} = \mathcal{H}(-\mathbf{k}). \quad (2.18)$$

Any Hamiltonian deformed continuously and smoothly in order to preserve Eq. 2.18 without a gap closing belong to the same topological class described by the invariant ν that may assume two values, 0 or 1, as demonstrated by Kane and Mele^[93].

The restriction of Kramers pairs becomes evident when we observe the bulk-boundary correspondence in a 2D insulator described by Eq. 2.18^[90]. Fig. 2.6 contains the electronic structured associated with edge states of a 2D \mathcal{T} -invariant insulator as a function of crystal momentum. The insulating bulk character is defined by the finite energy gap separating the conduction and valence bands. Depending on the details of $\mathcal{H}(\mathbf{k})$ at the edges, there may exist edge states within the gap. When these states are present, Kramers theorem require that they occur in degenerate pairs^[93] in specific points along the BZ at which the time reversal symmetry is preserved. Due to the spin-orbit coupling, only a few points $\Gamma_{a,b}$, referred to as TRIMs (time reversal invariant momenta), satisfy Eq. 2.18. In Fig. 2.6, the edge states at $k_x = 0$ and $k_x = \pi/a$ necessarily cross the Fermi level E_F an even number of times; in this case the reduction or even elimination of edge states to some potential is possible, allowing for backscattering such that they are localized by weak disorder^[93]. The QSH phase defined by Kane and Mele, however, distinguishes itself from a trivial insulating phase by the number of pairs of edge states *modulo* 2, i.e., the Fermi level is crossed an odd number of times, characterizing topologically protected conducting edge states^[90,93]. The bulk-boundary correspondence thus relates the number N_k of Kramers pairs that cross E_F to the change of the invariant ν , that is, $N_K = \Delta\nu \bmod 2$.

There are a number of ways to determine the \mathbb{Z}_2 invariant^[93-97]. A widely used approach to classify TIs based on band structure calculations, proposed by Kane and Mele in 2005, is to define an unitary matrix $w_{m,n}(\mathbf{k})$ constructed from occupied Bloch states,

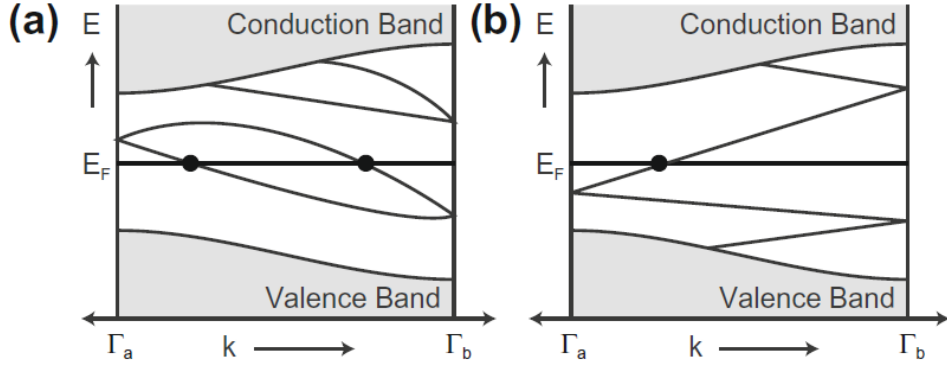


Figure 2.6: Sketch of possible band structures at the edges of a 2D material, as a function of momentum k along the edges. (a) The Fermi level is crossed an even number of times, characterizing a trivial phase. (b) Odd number of Fermi level crossing, characterizing a non-trivial topological phase robust against small perturbations. Only half the BZ is mapped since TR symmetry implies that the other half $-\pi/a < k < 0$ is its mirror image. Figure extracted from Franz e Molenkamp (2013)^[90].

so that

$$w_{m,n}(\mathbf{k}) = \langle u_m(-\mathbf{k}) | \Theta | u_n(\mathbf{k}) \rangle. \quad (2.19)$$

Since the transformation Θ is unitary, it follows that $w^T(\mathbf{k}) = -w(-\mathbf{k})$. In the Brillouin zone of a 2D TI (3D) there are four (eight) points Γ_i at which the momenta \mathbf{k} and $-\mathbf{k}$ coincide (TRIMs) and the matrix $\omega(\Gamma_i)$ is antisymmetric. The determinant of an antiunitary matrix is given by the square root of its Pfaffian, so that the authors defined the quantity δ_i ^[93,94]:

$$\delta_i = \frac{\sqrt{\det[w(\Gamma_i)]}}{\text{Pf}[w(\Gamma_i)]} = \pm 1. \quad (2.20)$$

As long as the eigenvectors $|u_m(\mathbf{k})\rangle$ are continuous throughout the entire BZ, the determinant of the matrices $\omega(\Gamma_i)$ may be globally defined, allowing the \mathbb{Z}_2 topological invariant classification to be obtained by counting the zeros of the Pfaffian of ω at half the torus *modulo 2*, such that

$$\boxed{(-1)^\nu = \prod_{i=1}^4 \delta_i.} \quad (2.21)$$

The extension of the above result for a three-dimensional case is direct and one defines four invariants $\nu_0; (\nu_1, \nu_2, \nu_3) \in \mathbb{Z}_2$ that allow one to classify a material as a strong or weak topological insulator, but that is not of any particular interest for this present text since the materials herein studied are exclusively two-dimensional.

The calculation of ν is simplified when the system possesses additional symmetries. For instance, if the system conserves spin at the z -axis, then $[\mathcal{H}, S_z] = 0$ and independent Chern numbers n_\uparrow e n_\downarrow may be associated to the $S_{z\uparrow}$ and $S_{z\downarrow}$ components. In these cases

there is a QSH effect for each spin component and it is possible to define the invariant via the spin quantized Hall conductivity^[98]. When the crystal has \mathcal{T} and centrosymmetry, at the TRIMs the Bloch states are also eigenstates of the parity operator \mathcal{P} with eigenvalues $\xi_m(\Gamma_i) = \pm 1$. In this context the \mathbb{Z}_2 invariant can be defined through the parities of the Kramers pairs' wave functions of occupied bands:

$$\delta_i = \prod_m \xi_m(\Gamma_i). \quad (2.22)$$

Another way to determine the invariant (and of particular interest for this thesis) is under the context of time reversal polarization (TRP) proposed by Fu and Kane^[99], from which it is possible to extend the calculation of ν to non-centrosymmetric crystals, as is the case for HgTe. The authors considered one-dimensional insulating Hamiltonians under a cyclic adiabatic “ \mathbb{Z}_2 spin pumping” , in which changes in TRP define a topological invariant that distinguish the system from a trivial insulating phase that is equivalent to the invariant introduced in the QSH effect.

In Fu and Kane's notation, the reversal polarization is a parallel to the electronic charge polarization in insulators by making use of electronic polarization related to Wannier charge centers (WCCs), which in turn are related to the Berry phase of Bloch wave functions^[99]. The authors then considered the role of Kramers pairs degeneracy in \mathcal{T} -invariant systems and defined the TRP in terms of the difference of WCCs of degenerate bands in such a way that changes in polarization throughout the cyclic process define ν .

We consider a one-dimensional system with $2N$ occupied bands described by a Hamiltonian obeying Eq. 2.18 in t . Such restriction guarantees the system is \mathcal{T} -invariant at $t = 0$ and $t = T/2$, whereas \mathcal{T} is broken in intermediate points along the torus defined by the BZ. From Kramers theorem, then, the eigenstates of $\mathcal{H}(t)$ are degenerate pairs at $k = 0$ and $k = \pi$ ^[99,100]. The Wannier functions associated to each unit cell with lattice parameter R are given by (Eq. B.1)

$$|R, n\rangle = \frac{1}{2\pi} \int dk e^{-ik(R-r)} |u_{k,n}\rangle,$$

and the polarization is given by the sum over all bands of WCCs (Eq. B.5) associated to $R = 0$ ^[99,101,102]:

$$P_\rho = \sum_n \langle 0, n | r | 0, n \rangle = \frac{1}{2\pi} \oint dk \mathcal{A}(k), \quad (2.23)$$

where Berry's connection is expressed as usual. Given the dependency of path choice for

the connection, the fact that the charge polarization can only be defined up to a lattice vector becomes explicit. The *changes* of polarization between different t , however, are well defined as long as the deformations acting on \mathcal{H} are continuous, usual. Therefore, if the Bloch functions are well defined continuously between instants t_1 and t_2 for any k in the BZ, then we have

$$\Delta P_\rho = \frac{1}{2\pi} \left[\oint dk \mathcal{A}(k, t_1) - \oint dk \mathcal{A}(k, t_2) \right]. \quad (2.24)$$

As seen in previous sections, the above definition may be expressed as the integral of Berry curvatures along the torus defined by (k, t) : this quantity is an integer given by the first Chern number, and for time reversal invariant systems, $\Delta P_\rho = 0$. Based on Kramers theorem, again, the Wannier charge centers come in degenerate pairs, where each pair is associated to the same center. The idea proposed by Fu and Kane, therefore, is to track only the center of one degenerate Wannier state defining what the authors named a partial polarization. Hence, we assume that $2N$ eigenstates are split into N pairs and must satisfy^[99]

$$\begin{aligned} |u_{-k,\alpha}^{\text{I}}\rangle &= -e^{i\chi_{k,\alpha}} \Theta |u_{k,\alpha}^{\text{II}}\rangle \\ |u_{-k,\alpha}^{\text{II}}\rangle &= e^{i\chi_{-k,\alpha}} \Theta |u_{k,\alpha}^{\text{I}}\rangle, \end{aligned} \quad (2.25)$$

where $\alpha = 1, \dots, N$. In analogy with the charge polarization, we define partial polarizations for each $s = \text{I, II}$ corresponding to Wannier centers,

$$P^s = \frac{1}{2\pi} \int_{-\pi}^{\pi} dk \mathcal{A}^s(k) = \frac{1}{2\pi} \int_0^{\pi} dk [\mathcal{A}^s(k) + \mathcal{A}^s(-k)], \quad (2.26)$$

where $\mathcal{A}^s(k) = i \sum_{\alpha} \langle u_{k,\alpha}^s | \nabla_k | u_{k,\alpha}^s \rangle$. From the above definitions it is easy to show that we may relate the partial connections as $\mathcal{A}^{\text{I}}(-k) = \mathcal{A}^{\text{II}}(k) - \sum_{\alpha} \nabla_k \chi_{k,\alpha}$, so that

$$P^{\text{I}} = \frac{1}{2\pi} \left[\int_0^{\pi} dk (\mathcal{A}^{\text{I}}(k) + \mathcal{A}^{\text{II}}(k)) - \sum_{\alpha} (\chi_{\pi,\alpha} - \chi_{0,\alpha}) \right]. \quad (2.27)$$

The first term is the Berry connection and the second term guarantees gauge invariance, since the integration path is open^[99]. This may be rewritten introducing the unitary matrix $\omega_{mn}(\mathbf{k})$, that in this case is antisymmetric at points $k = 0$ and $k = \pi$. In the same

manner as before, we characterize $\omega_{mn}(\mathbf{k})$ by its Pfaffian, and thus we have

$$\ln \left\{ \frac{\text{Pf}[w(\pi)]}{\text{Pf}[w(0)]} \right\} = i \sum_{\alpha} (\chi_{\pi,\alpha} - \chi_{0,\alpha}). \quad (2.28)$$

We note that the total charge polarization is given by the sum of partial polarizations $P_{\rho} = P^{\text{I}} + P^{\text{II}}$; we thus define the time reversal polarization as the difference $P_{\theta} = P^{\text{I}} - P^{\text{II}}$, written as^[99]

$$P_{\theta} = \frac{1}{2\pi} \left[\int_0^{\pi} dk \mathcal{A}(k) - \int_{-\pi}^0 dk \mathcal{A}(k) + 2i \ln \left(\frac{\text{Pf}[w(\pi)]}{\text{Pf}[w(0)]} \right) \right]. \quad (2.29)$$

The TRP defined above is an integer defined *modulo 2*; odds and evens are distinguished by the path choice between $k = 0$ and $k = \pi$, and therefore the authors wrote P_{θ} as

$$(-1)^{P_{\theta}} = \frac{\sqrt{\det[w(0)]}}{\text{Pf}[w(0)]} \frac{\sqrt{\det[w(\pi)]}}{\text{Pf}[w(\pi)]}. \quad (2.30)$$

We may then infer that P_{θ} defines states with distinct polarizations and are related to the presence or absence of degenerate Kramers pairs in the system, and thus define distinct topological phases given that P cannot be altered by continuous deformations of \mathcal{H} that preserve \mathcal{T} . However, the authors proved that adiabatic changes in \mathcal{H} that preserve TRS at the initial and final points of a cycle define a \mathbb{Z}_2 topological invariant given by the difference of time reversal polarization (that maps the changes of Wannier centers throughout a cycle) between $t = 0$ and $t = T/2$, i.e., $\Delta = P_{\theta}(T/2) - P_{\theta}(0) \bmod 2$. Finally, we can calculate the topological invariant at the TRIMs as

$$\boxed{(-1)^{\Delta} = \prod_{i=1}^4 \frac{\sqrt{\det[w(\Gamma_i)]}}{\text{Pf}[w(\Gamma_i)]}.} \quad (2.31)$$

Eq. 2.31 is specially useful in systems where additional symmetries, such as centrosymmetry, is present. The question that arises at this stage is: is this true for non-centrosymmetric systems, as is the case for GeTe or HgTe? The answer is yes: in 2011 Soluyanov and Vanderbilt^[100] developed a method for calculating Δ that is applicable to any system, being particularly useful when the material is non-centrosymmetrical, as is the case for HgTe. In terms of WCCs, Δ may be rewritten as

$$\Delta = \sum_{\alpha} [\bar{x}_{\alpha}^{\text{I}}(T/2) - \bar{x}_{\alpha}^{\text{II}}(T/2)] - \sum_{\alpha} [\bar{x}_{\alpha}^{\text{I}}(0) - \bar{x}_{\alpha}^{\text{II}}(0)]. \quad (2.32)$$

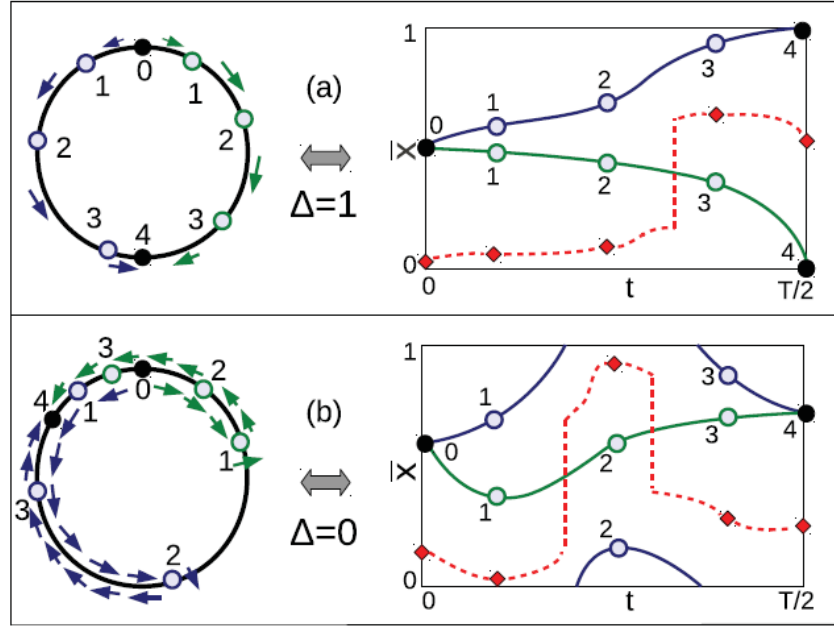


Figure 2.7: Wannier charge center evolution \bar{x} as a function of time t in an adiabatic process. The WCCs wrap around an unit circle as t varies from 0 to $T/2$. (a) Odd number of pair exchanges, defining a \mathbb{Z}_2 insulator. (b) WCCs reconnect without exchanging pairs, defining a trivial phase. Figure extracted from Soluyanov (2011)^[100].

This method consists of tracking the evolution of WCCs along the torus between $t = 0$ and $t = T/2$ using a gauge that satisfies \mathcal{T} invariance and continuity over the half-torus^[100]. Soluyanov and Vanderbilt demonstrated that to calculate the \mathbb{Z}_2 invariant it is necessary to choose a gauge that respect such restrictions and this corresponds to maximum localized Wannier functions (MLWFs) for each t , as long as the WFs are a smooth function of t . Such gauge choice must provide the smallest possible quadratic deviation $\Omega = \sum_n (\bar{x}_n^2 - \bar{x}_n^2)$. Under these constraints, the MLWFs are eigenvectors of the position operator, which in turn commutes with the time reversal operator Θ . In other words, its eigenvalues are doubly degenerate and its eigenvectors come in Kramers pairs in $t = 0$ and $t = T/2$. Now, since WCCs are defined *modulo* 1^[100], we may imagine them wrapping an unit circle after each half-cycle (Fig. 2.7); the system will be in an odd \mathbb{Z}_2 state ($\Delta = 1$) if along the process the WCCs (blue and green curves representing two charge centers) “exchange” pairs, that is, two Kramers pairs in $t = 0$ *do not reconnect* in $t = T/2$, which is equivalent to the previous argument of the Fermi level being crossed an odd number of times by degenerate Kramers pairs, thus defining a non-trivial band topology. In the case of even pair exchanges, the WCCs reconnect without the unit circle being wrapped as a whole, with no effective Kramers pairs exchange. In general, as the \bar{x}_n are carried out throughout the BZ between $t = 0$ and $t = T/2$, they either exchange

pairs or they do not, defining an odd or even \mathbb{Z}_2 invariant, respectively. This allows us to draw an arbitrary curve along the WCCs evolution and depending on the number of times said curve is crossed by the \bar{x}_n the system will be of non-trivial (odd) or trivial (even) topological nature. An extension of this method consists in, instead of tracking the individual WCCs evolution, determining the largest gaps between WCCs (red curves in Fig. 2.7b), which allows us by visual inspection to determine the topological invariant from the flux of WCCs through the manifold (\bar{x}_n, t) . This method is of particular interest since the post-processing WannierTools^[103] algorithm used at the end of chapter V is partially based on it.

Chapter III

Methodological Fundamentals

In this chapter the theoretical background of methods applied in the composition of this thesis will be presented. In summary, the approach is based on Density Functional Theory (DFT) in the context of periodic systems with plane-wave basis and pseudopotentials, that poses as an approximative solution to the many-body Schrödinger's equation, given its exact insolubility. In DFT, if the electronic density $\rho(\mathbf{r})$ is known, the system's ground state energy, as well as its other structural properties, may be uniquely determined once these are treated as functionals of ρ . Rather than using the usual wave function, an abstract quantity with no physical interpretation, with $3N$ spatial coordinates and N spin coordinates, the electronic density is treated as the fundamental quantity that is only a function of $3N$ spatial coordinates, and thus the many-body problem is greatly simplified. Therefore, the DFT facilitates the study of many-electron systems, being extensively used in condensed matter research. The topological phase transitions require, in this context, use of Wannier functions to determine surface states and topological index $\nu \in \mathbb{Z}_2$. Based on this formalism, employment of methods to calculate ν for periodic materials with and without inversion symmetry becomes necessary for the topological properties studied in this thesis.

3.1 The Many-Body Interaction Problem

A large portion of available electronic structure methods is based on the Born-Oppenheimer approximation, where the mass of electrons is considered to be much smaller than that of nuclei, so that within the electronic time frame the nuclear dynamics can be neglected. Hence, within this approximation we consider electrons moving in a “field” of fixed nuclei, resulting in the decoupling of electronic and nuclear dynamics. That is

to say the Hamiltonian describing the system will have distinct contributions, with the electronic wave function being explicitly dependent on electronic coordinates, so that for each nuclear configuration there is a different electronic problem to be solved. Therefore, the system Hamiltonian in an orthonormal basis $\{|\psi_n\rangle\}$ may be written as^[104]

$$\mathcal{H} = T + V_{en} + V_{ee} = \sum_{\mu\nu} h_{\mu\nu} a_{\mu}^{\dagger} a_{\nu} + \frac{1}{2} \sum_{\mu\nu\kappa\gamma} g_{\mu\nu\kappa\gamma} a_{\mu}^{\dagger} a_{\kappa}^{\dagger} a_{\nu} a_{\gamma}, \quad (3.1)$$

where (Eq. C.16)

$$h_{\mu\nu} = \langle \psi_{\mu} | \mathcal{H}_{en} | \psi_{\nu} \rangle = \int d\mathbf{r} \psi_{\mu}^*(\mathbf{r}) \left[-\frac{\hbar^2}{2m} \nabla^2 - \frac{1}{4\pi\epsilon_0} \sum_{\mathbf{R}} \frac{Z}{|\mathbf{R} - \mathbf{r}|} \right] \psi_{\nu}(\mathbf{r}) \quad (3.2)$$

is the electronic Hamiltonian $T + V_{en}$, due to the nuclei, of an electron described by a wave function ψ_n , and

$$g_{\mu\nu\kappa\gamma} = \langle \psi_{\mu} \psi_{\kappa} | V_{ee} | \psi_{\nu} \psi_{\gamma} \rangle = \frac{1}{4\pi\epsilon_0} \int d\mathbf{r} d\mathbf{r}' \psi_{\mu}^*(\mathbf{r}) \psi_{\kappa}^*(\mathbf{r}') \frac{1}{|\mathbf{r} - \mathbf{r}'|} \psi_{\nu}(\mathbf{r}) \psi_{\gamma}(\mathbf{r}') \quad (3.3)$$

the repulsive potential V_{ee} due to the electron-electron interaction. Despite simplifying the problem using the Born-Oppenheimer approximation, the repulsion term still results in unfeasible calculations in typical cases, forcing us to resort to additional approximations, namely Hartree-Fock and DFT, for instance.

3.2 The Hartree-Fock Approximation

The Hartree-Fock approach (HF) is a variational method based on finding an approximation for the ground state of a system composed of N electrons as we minimize the total energy E^{HF} ^[105–108]. We begin with a reference state $|0\rangle$ lying within Fock space, spanned by an orbital orthonormal basis $\{|\psi_n\rangle\}$, from which the Slater determinant is constructed in such a way that

$$a_N^{\dagger} \dots a_2^{\dagger} a_1^{\dagger} |0\rangle = |\psi^{HF}\rangle, \quad (3.4)$$

where it follows that the Hartree-Fock energy related to the reference state is given by the expectation value of \mathcal{H}^{HF} :

$$E^{\text{HF}} = \langle 0 | \mathcal{H}^{\text{HF}} | 0 \rangle = \sum_{\mu\nu} h_{\mu\nu} \langle 0 | a_{\mu}^{\dagger} a_{\nu} | 0 \rangle + \frac{1}{2} \sum_{\mu\nu\kappa\gamma} g_{\mu\nu\kappa\gamma} \langle 0 | a_{\mu}^{\dagger} a_{\kappa}^{\dagger} a_{\nu} a_{\gamma} | 0 \rangle. \quad (3.5)$$

The first term, related to the energy of an electron, tells us that the processes $\langle 0 | a_{\mu}^{\dagger} a_{\nu} | 0 \rangle$ are only possible if the orbitals μ and ν are occupied, so the created vectors must be equal due to the orthonormality of basis vectors. Hence, $\sum_{\mu\nu} h_{\mu\nu} \langle 0 | a_{\mu}^{\dagger} a_{\nu} | 0 \rangle = \sum_{\alpha} h_{\alpha\alpha}$. For the two-electron energy, the operators $a_{\nu} a_{\gamma}$ attempt to remove electrons to the right, and the orbitals must be occupied, but need not be identical. Similarly, the $a_{\mu}^{\dagger} a_{\kappa}^{\dagger}$ operators attempt to remove electrons to the left, and once more the orbitals μ and κ must be occupied, but need not be identical. Hence, there are two possibilities where $\mu\kappa = \nu\gamma$, resulting in non-zero inner products:

$$\sum_{\mu\nu\kappa\gamma} g_{\mu\nu\kappa\gamma} \langle 0 | a_{\mu}^{\dagger} a_{\kappa}^{\dagger} a_{\nu} a_{\gamma} | 0 \rangle = \sum_{\alpha \neq \beta} \{ g_{\alpha\beta, \alpha\beta} \langle 0 | a_{\alpha}^{\dagger} a_{\beta}^{\dagger} a_{\alpha} a_{\beta} | 0 \rangle + g_{\alpha\beta, \beta\alpha} \langle 0 | a_{\alpha}^{\dagger} a_{\beta}^{\dagger} a_{\beta} a_{\alpha} | 0 \rangle \}.$$

From the anticommutator relation $\{a_{\alpha} a_{\beta}\}$ it follows that $a_{\alpha} a_{\beta} = -a_{\beta} a_{\alpha}$, and thus we have

$$\sum_{\mu\nu\kappa\gamma} g_{\mu\nu\kappa\gamma} \langle 0 | a_{\mu}^{\dagger} a_{\kappa}^{\dagger} a_{\nu} a_{\gamma} | 0 \rangle = \sum_{\alpha \neq \beta} \{ g_{\alpha\beta, \alpha\beta} - g_{\alpha\beta, \beta\alpha} \}. \quad (3.6)$$

Finally, we may rewrite Eq. 3.5 as^[109]:

$$E^{\text{HF}} = \sum_{\alpha} h_{\alpha\alpha} + \frac{1}{2} \sum_{\alpha \neq \beta} \{ g_{\alpha\beta, \alpha\beta} - g_{\alpha\beta, \beta\alpha} \} = \sum_{\alpha} h_{\alpha\alpha} + \sum_{\alpha \neq \beta} F_{\alpha\beta}. \quad (3.7)$$

Here, we identify $h_{\alpha\alpha}$ as the usual electronic Hamiltonian, given by the kinetic energy plus the external potential due to the static nuclear potential. The term $g_{\alpha\beta, \alpha\beta}$ is the Coulomb repulsion (V_{ee}) and the term $g_{\alpha\beta, \beta\alpha}$ is denoted the exchange integral, J , arising from the Coulomb interaction and Pauli's exclusion principle.

The Hartree-Fock energy (or Fock matrix, $F_{\alpha\beta}$ ^[109]) defined in Eq. 3.7 represents an upper limit for the ground state energy and is a functional of the occupied orbitals $|\psi_{\alpha}\rangle$, and its minimization can be obtained by the orthonormal orbitals restriction, i.e., $\langle \psi_{\alpha} | \psi_{\beta} \rangle = \delta_{\alpha\beta}$. Such optimization is commonly reached by making use of Lagrange

multipliers

$$\mathcal{L}^{\text{HF}}[\{\psi_\alpha\}] = E^{\text{HF}}[\{\psi_\alpha\}] - \sum_{\alpha\beta} \lambda_{\alpha\beta} \{\langle \psi_\alpha | \psi_\beta \rangle - \delta_{\alpha\beta}\}, \quad (3.8)$$

from which we may finally express the Hartree-Fock energy in terms of individual orbital energies:

$$E^{\text{HF}} = \sum_{\alpha} \varepsilon_{\alpha} + \frac{1}{2} \sum_{\alpha\beta} (V_{\alpha\beta,\alpha\beta} - J_{\alpha\beta,\beta\alpha}). \quad (3.9)$$

We hence notice that within the Hartree-Fock approximation the total energy is *not* equal to the sum of individual orbital energies. In fact, the approximation is based in the assumption a problem of N interacting bodies is decomposed into N decoupled equations. The optimization is done self-consistently, since the solutions are functionals of the reference state - the Fock matrix depends, through the sum over occupied orbitals (or density matrix), on the Slater determinant on which it is applied. The HF approximation thus is a key milestone in the development of methods to solve many-body quantum problems. However, it does not take into account the electron correlation, since it treats each electron as though interacting with the remaining electrons via an effective potential. The correlation energy, denoted as E_{corr} , is defined as the difference between the exact ground state energy and the Hartree-Fock energy. Any modern method that aims to improve these approximations must somehow include the correlation energy. A powerful alternative is poised in first-principles calculations such as DFT, in which the wave functions are replaced by the charge density as a fundamental quantity and every system property can be extracted from it.

3.3 Density Functional Theory

As mentioned, the wave equation for real systems is impossible to solve when the number of electrons N is sufficiently large, and thus robust approximate methods for the Coulomb interactions are necessary. As a direct consequence, the electronic wave function cannot be written as a single Slater determinant^[70], and it follows that the complexity of the problem grows exponentially with N . In this scope, DFT is poised as a powerful tool for electronic structure calculations, offering precise results for finite periodic systems or with a small number of atoms. Nevertheless, in spite of constant software and code advances and developments, the theory still has practical limitations owing to self-consistency and dimensionality of the system of interest, since electrons are

often described by plane waves. Luckily, the study of functional two-dimensional materials are performed on much smaller scales.

The DFT is the foundation of *ab initio* calculations and is based on the proof by P. Hohenberg and W. Kohn^[110] (1964) that the ground state wave function of an interacting many-body quantum system can be treated as a functional of the electronic density $\rho(\mathbf{r})$ of the ground state, effectively reducing Eq. C.16 to a one-particle Hamiltonian, i.e., the $3N$ variables problem becomes N problems of 3 variables. The ground state energy is, therefore, also a functional of $\rho(\mathbf{r})$ and its minimum is the exact ground state energy of the system in question. Correspondingly, we may in principle solve the many-body problem by minimizing the energy functional, similar to the Fock matrix. Hence, Hohenberg-Kohn postulated two theorems (whose proofs are readily available in any textbook and will not be included here):

Teorema 1. *The effective potential V_{eff} acting on the electrons is a unique functional of the electronic density $\rho(r)$;*

Teorema 2. *For a given electronic density $\rho' > 0$, the total energy is an upper limit for the exact ground state energy, i.e., $E_0 \leq E[\rho']$.*

The second Hohenberg-Kohn theorem is an exact analog of the variational principle, where the test quantity is the wave function. The minimization of the test density determines its own Hamiltonian that consequently determines its own wave function. In 1965, Kohn-Sham^[111] provided a self-consistent strategy, analogous to Eq. 3.7, to minimize the ground state energy of a system by constructing a reference system of non-interacting electrons subject to an effective potential with electronic density exactly equal to the density of an interacting electrons system. Naturally, the result will be as good as the choice of an energy functional on which it is based and, despite the second Hohenberg-Kohn theorem guaranteeing the existence of said functional, its exact form is still unknown and widely used additional approximations are necessary, namely the generalized gradient (GGA) and local density approximations.

Since every property is a functional of the electronic density $\rho(\mathbf{r}) = a^\dagger(\mathbf{r})a(\mathbf{r})$, in DFT the total Hamiltonian of an arbitrary system is

$$\mathcal{H}^{\text{KS}}[\rho] = \mathcal{H}_{el.} + V^{\text{KS}} = \mathcal{H}_{el.}[\rho] + V_{ee}[\rho] - w_{\text{ex.}}K[\rho] + v_{\text{xc}}[\rho], \quad (3.10)$$

where K is the exact exchange contribution for the Kohn-Sham energy and v_{xc} is the

exchange-correlation potential, over which the previously mentioned approximations are made. The scaling factor $w_{ex.}$ is zero for non-hybrid theories^[112], such as GGA. The Kohn-Sham is then written as:

$$E^{KS} = \langle 0 | \mathcal{H}^{KS} | 0 \rangle = \sum_{\mu\nu} h_{\mu\nu} \langle 0 | a_{\mu}^{\dagger} a_{\nu} | 0 \rangle + \frac{(1 - w_{ex.})}{2} \sum_{\mu\nu\kappa\gamma} g_{\mu\nu\kappa\gamma} \langle 0 | a_{\mu}^{\dagger} a_{\kappa}^{\dagger} a_{\nu} a_{\gamma} | 0 \rangle + E_{xc}[\rho]. \quad (3.11)$$

We may, for simplicity, express the KS energy in terms of the density matrix C.22 in order to obtain the KS matrix, equal to the Fock matrix encountered in the previous section up to a scaling factor $w_{ex.}$, and given by the derivative of E^{KS} with respect to the matrix $D_{\mu\nu}$ ^[112]:

$$(G^{KS}(D))_{\mu\nu} = \frac{\partial E^{KS}[\rho]}{\partial D_{\nu\mu}} = \sum_{\mu\nu} h_{\mu\nu} + F_{\mu\nu}^{HF}(D) + \frac{\partial E_{xc}[\rho]}{\partial D_{\nu\mu}}, \quad (3.12)$$

where we have defined $G_{\mu\nu}^{HF} = \sum_{\kappa\gamma} D_{\gamma\kappa} (g_{\mu\nu\kappa\gamma} - w_{ex.} g_{\mu\gamma\kappa\nu})$. Here, the third term of the KS matrix is the derivative of the exchange-correlation energy, defined as the exchange correlation potential, given by

$$v_{xc}(\mathbf{r}) = \frac{\delta E_{xc}}{\delta \rho(\mathbf{r})}. \quad (3.13)$$

Similarly to the Hartree-Fock approximation, we may minimize the Kohn-Sham equation by using Lagrange multipliers or exponential parametrizations to obtain the individual Kohn-Sham orbital eigensolutions^[70]:

$$\boxed{\mathcal{H}^{KS} |\psi_i^{KS}\rangle = E_i |\psi_i^{KS}\rangle}. \quad (3.14)$$

We see now explicitly that the strategy employed by Kohn and Sham allows us to replace a problem of N interacting electrons with N problems of a single electron subject to an effective external potential that accounts for the interactions with the remaining system electrons and nuclei, similar to the HF approximation. The ground state solution is thus found by identifying the N eigenvalues of Eq. 3.14 and constructing the charge density

$$\rho(\mathbf{r}) = \sum_{i=1}^N \psi_i^{\dagger}(\mathbf{r}) \psi_i(\mathbf{r}) a_i^{\dagger} a_i \quad (3.15)$$

which in turn is used to obtain a new KS potential and from it, new solutions. Having a new set of solutions, a new density ρ^{i+1} is calculated and then compared with the initial density ρ^i : if the difference of densities is within a previously established convergence threshold, ρ^{i+1} may be used to determined system observables. If convergence is not

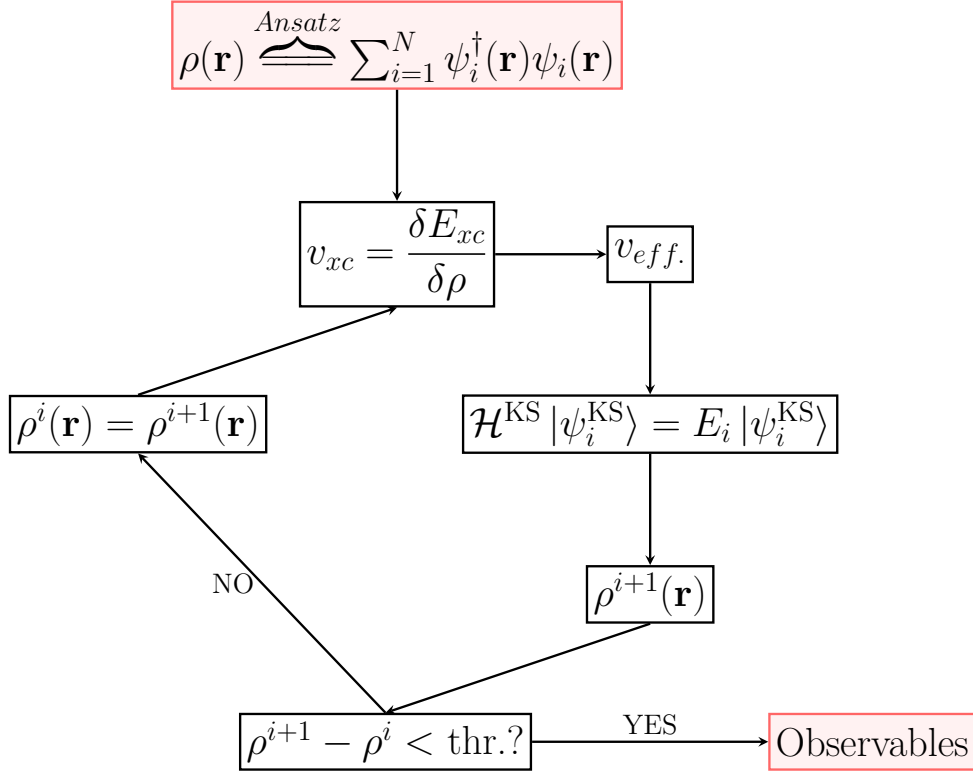


Figure 3.1: Self-consistency cycle sketch.

achieved, ρ^{i+1} is plugged back into the KS equation and the cycle is repeated until a self-consistent solution for ρ and V^{KS} is found^[70,111], as illustrated in Fig. 3.1.

3.4 Exchange-Correlation and Hybrid Functionals

Essentially, DFT is a purely exact theory, however it does not provide any means to understand the properties of a given material by only knowing the shape of its electronic density. As previously mentioned, its application is tied to how good is the functional of choice for the exchange-correlation energy description. The branch of physics for development and testing of functionals able to accurately describe the potential v_{xc} is highly active and though the exact form of the $E[\rho]$ functional is complex, an extraordinary success is reached with quite simple approximations. Notably, the simplest LDA form was provided by KS in their seminal work^[70,110,113], where the authors suggest ρ may be treated locally as a homogeneous electron gas:

$$E_{xc}^{LDA} = \int d\mathbf{r} \rho(\mathbf{r}) \epsilon_{xc}[\rho(\mathbf{r})] = \int d\mathbf{r} \rho(\mathbf{r}) [\epsilon_x + \epsilon_c], \quad (3.16)$$

where ϵ_{xc} is the exchange-correlation energy per electron of an uniform electron gas of density $\rho(\mathbf{r})$. Thus, in this approximation the potential v_{xc} takes the form:

$$v_{xc}^{LDA}[\rho(\mathbf{r})] = \frac{\delta E_{xc}^{LDA}}{\delta \rho(\mathbf{r})} = \epsilon_{xc}(\rho(\mathbf{r})) + \rho(\mathbf{r}) \frac{\partial \epsilon_{xc}(\rho)}{\partial \rho}. \quad (3.17)$$

Since the E_{xc}^{LDA} functional is universal, the only necessary information is the electron gas exchange-correlation energy, i.e., for practical LDA applications one needs to determine E_{xc} of an uniform gas with a given density $\rho(\mathbf{r})$. The basis of this approximation is that for densities commonly found in solids, the exchange and correlation effects are of short range. However, how far this can be used in practical applications must be tested. For materials where the density is similar to that of a homogeneous gas, such as metals, the use of LDA is quite suitable. In cases where the density varies abruptly, such as in molecules, its use often fails. Still, the LDA is a mark for the construction of more generalized and adequate functionals for non-homogeneous systems, namely the GGA functional, where not only the value of ρ at every \mathbf{r} is expressed, but also E_{xc} as a function of the density's gradient $\nabla \rho$ ^[114]:

$$E_{xc}^{GGA}[\rho(\mathbf{r}), \nabla \rho(\mathbf{r})] = \int d\mathbf{r} \rho(\mathbf{r}) \epsilon_x F_{xc}[\rho(\mathbf{r}), \nabla \rho(\mathbf{r})], \quad (3.18)$$

where F_{xc} is a dimensionless local exchange factor. The GGA functional has various available parametrizations, however for this thesis only the Perdew-Burke-Ernzerhof^[114] (PBE) parametrization will be used and more details regarding its implementation can be found in their original work.

As the calculation of E^{KS} and ρ utilizing the mentioned functionals has no empirical parameter, we may consider them to be *ab initio*, commonly denoted first-principles. The band gap estimatives within Kohn-Sham's formalism is done by taking the difference between the highest occupied and lowest unoccupied energy levels. However, despite great success of simpler functionals such as LDA and GGA for electronic band structure characterizations, it is well established that these functionals underestimate real gaps^[115], specially in semiconducting systems. An alternative is given in the form of hybrid functionals^[116-119] that allow for a better description of important physical properties descriptions, such as lattice parameter and band gaps. Hybrid functionals such as Heyd-Scuseria-Ernzerhof (HSE) e B3LYP^[118-120] are widely used in the description of atoms and molecules and are based on employing a fraction of the short-range Hartree-Fock

exchange, rather than the exact local exchange, offering a better energy gap description that is comparable to experimental values. The HSE06 functional applied in chapter IV uses an error function to split the Coulomb potential in short-range and long-range contributions to calculate the exact HF exchange, and the exchange-correlation term can be expressed as

$$E_{xc}^{HSE} = aE_x^{HF,SR} + (1 - a)E_x^{PBE,SR} + E_x^{PBE,LR} + E_c^{PBE}, \quad (3.19)$$

where a is the HF mixing parameter^[118,119], $E^{HF,SR}$ is the HF exchange energy and $E^{PBE,SR}$ and $E^{PBE,LR}$ are the short and long-range PBE functional components, respectively.

3.5 Computational Details

In the following chapters our results and discussions regarding the electronic and structural properties of monolayer α -In₂Se₃ within the context of strain engineering and subsequently of surface oxidation will be presented. To assess these properties, the electronic structure calculations were carried out using DFT within the GGA-PBE approximation^[121] for the exchange-correlation functionals, where the employment of the HSE06 hybrid functional^[122] was necessary for a better approximation of experimental band gaps.

At first, to characterise the system, optoelectronic properties of single-layer α -In₂Se₃ subject to biaxial strains were explored. It was shown that this system is highly sensitive to external factors that lead to unit cell compressions or expansions, as well as the feasibility of manipulating the electronic band gap and consequently the material's optical properties under certain conditions, leading to its applicability in photocatalyst devices. Next, we explored how such properties respond to adsorption of oxygen atoms to the layer's surface and how the band topology is classified within these conditions. We showed that the newly formed α -In₂Se₃O material undergoes a quantum phase transition due to the emergence of non-trivial topological edge states that can be further manipulated through external applied electric fields.

In all cases, we start from an hexagonal unit cell with a vacuum of more than 20 Å in the z -axis to avoid periodic image interactions. The systems were treated within the context of DFT calculations^[110,111] carried out as implemented in the Quantum ESPRESSO (QE)^[123,124]. The exchange-correlation functional was treated using the

PBE parametrization of the GGA approximation, unless the use of hybrid functionals is needed. Valence electrons were described by the projector-augmented wave method (PAW)^[125], whereas core electrons were modeled with norm-conserving pseudopotentials following the Troullier and Martins^[126] parametrization.

The cutoff energy for the plane wave basis was fixed at 60 Ry and a Monkhorst-Pack^[127,128] k -grid of $6 \times 6 \times 1$ was adopted and was sufficient for Brillouin zone sampling, leading to a convergence threshold of 10^{-8} eV. Geometric optimizations were carried out until residual forces on each ion were less than 0.01 eV/Å.

Structural stability was studied by employing the density functional perturbation theory (DFPT) as implemented in the QE PHonon package. Interatomic forces were calculated over a $3 \times 3 \times 1$ supercell with a $12 \times 12 \times 1$ q -point grid, within a convergence threshold of 10^{-12} eV Å⁻¹.

In-plane and out-of-plane electronic polarization calculations were carried out for each unit cell using the Berry phase approach, as implemented in the modern theory of electronic polarization. The in-plane polarization was calculated as the sum of x and y components, since QE implementations only allow for in-axis calculations.

The \mathbb{Z}_2 topological invariant was calculated from the orthogonal maximum localized Wannier function basis obtained from self-consistent calculations used in the construction of a tight-binding Hamiltonian, as implemented in the WannierTools^[103] package. The calculation of surface states corresponding to bulk topology was carried out using the surface Green's function for a semi-infinite system.

Chapter IV

Single-layer α - In_2Se_3 as a Photocatalyst for H_2O Splitting

This finished work has been published in *Phys. Chem. Chem. Phys.*, 2020, 22, 3520-3526.

Driven by the search for new forms of renewable energy that could replace fossil fuels and reduce environmental impacts, hydrogen generation from photocatalytic water-splitting processes has attracted much attention due to its economical interest as well as the fact that it does not produce pollutants. However, efficient photocatalytic water-splitting is somewhat challenging. Photocatalysts require a band gap energy of the order of water reduction potential (1.23 eV), which imposes limits upon potential materials, and even within this regime the efficiency of the solar-to-hydrogen process is as low as 10%^[129,130]. Additionally, the water splitting process requires good carrier mobility and adequate band edge alignment^[131] to drive hydrogen evolution reaction (HER), as well as oxygen reduction (OER).

Two-dimensional semiconductors are potential candidates to fit these criteria and have been explored as promising photocatalysts for HER^[26,132–134], due to their striking electronic and optical properties and tunable band gaps. Although many materials have been proposed as photocatalysts, their overall synthesis is difficult, and even those that have been synthesized, such as phosphorene^[130] and SnO^[132], still possess limitations, motivating the search for more efficient candidates.

Among these materials, indium selenide (In_2Se_3) is a III₂-IV₃ group layered semiconducting compound that has been extensively studied for many years due to its varying applications that include photodetection^[61,64,135] and phase random access memo-

ries^[65,136]. In₂Se₃ is formed by vertical stacking of covalently bonded quintuple layers of In and Se sheets via weak van der Waals interaction with a sizable direct band gap of 1.3-2.0 eV in its bulk α phase or in the few-layers regime^[69,137-140], and shows very efficient visible-light absorption^[26,63], which may offer promising use in solar energy conversion and supports applications in photocatalytic activity for hydrogen gas generation or Cr(VI) removal^[134]. This material has also been shown to be an excellent broad-range photodetector, with photoresponses ranging from ultraviolet to short-wavelength infrared^[64]. Additionally, this selenide has intrinsic out-of-plane ferroelectricity^[67,69], which can be explored to improve and accelerate the carrier mobility required for a higher efficiency in the photocatalytic water-splitting process^[32].

The ability to manipulate the nature of the electronic structure of 2D materials has been permitting the functionalization of nanomaterials and the development of the next generation of ultrathin nanodevices. For instance, graphene and graphene-based devices have shown promising performance as both gas^[141-143] and biosensors^[144-146]. Despite investigations on the adsorption of gas molecules on 2D indium selenide being somewhat scarce, InSe and α -In₂Se₃ have recently been shown theoretically to be applicable as gas molecule sensors, such as N₂, NH₃^[147], NO and NO₂^[148]. Strain engineering has also been used to adjust the electronic structure and band gap of semiconducting materials, such as thin films. Strain may be achieved experimentally by controlled synthesis routes, such as deposition rates in epitaxial growth, sample thickness, changes in substrates, applied pressure and other techniques^[149,150]. In this context, Feng *et al.*^[151] have demonstrated that strain sensor arrays fabricated from patterned 2D α -In₂Se₃ films show excellent stability and high spatial resolution in strain distributions, leading to interesting applications in wearable electronic devices for robotics and human body monitoring.

In order to shed some light on the nature of the electronic structure of the α phase of In₂Se₃ under strain, we have performed calculations based on Density Functional Theory (DFT). Here we report a thorough investigation of the influence of biaxial strains on the electronic properties of single layers of α -In₂Se₃, and the results show that there is a change of the band gap nature. Furthermore, our results also demonstrate that this material is suitable for photocatalysis with compressive strains.

The effect of the biaxial strain on the electronic structure was investigated by defining $\varepsilon_b = (a - a_0)/a_0$, where a (a_0) is the new in-plane lattice constant (lattice parameter of the fully relaxed system). In this sense, aiming to examine the photocatalytic performance of α -In₂Se₃ under strain, the hybrid Heyd-Scuseria-Ernzerhof (HSE06) functional

was employed to better describe the band gap energy, as implemented in the Vienna Ab Initio Simulation Package (VASP)^[152]. To perform the band edge alignments, we have calculated the electrostatic potential of the single layers along the z -axis, while adding a self-consistent dipole correction to the vacuum region in order to balance the energy levels of different sides of the monolayer due to intrinsic electric polarization^[67]. All energy levels were then subtracted by the calculated reference level in order to determine the position of the band edges for comparison to water oxidation and reduction potentials.

The UV-Vis optical absorption of the studied material was calculated by applying the sum-over-state method implemented in VASP along with HSE06 formalism. The optical properties were obtained from the frequency-dependent complex dielectric function $\epsilon(\omega) = \epsilon_1(\omega) + i\epsilon_2(\omega)$, using the Kramers-Kronig relation^[153]. To determine the fraction of light absorbed by the material, we have calculated the optical absorption coefficient α (in cm⁻¹) for each structure as a function of the wavelength of the incident light using the following equations:

$$\alpha(\omega) = \frac{4\pi}{\lambda} \left(\frac{\sqrt{\epsilon_1^2 + \epsilon_2^2} - \epsilon_1}{2} \right)^{1/2}. \quad (4.1)$$

where λ and ω are the wavelength and frequency of the incident light, respectively. These calculations were performed using a $12 \times 12 \times 1$ k -point mesh with a 520 eV energy cutoff.

The fully relaxed crystal structure of monolayer α -In₂Se₃ is depicted in Fig. 4.1(a). Each monolayer is five atoms thick, arranged in a Se-In-Se-In-Se sequence, with a total height of one quintuple-layer of about 6.6 Å. The calculated lattice parameter is 4.106 Å, which agrees very well with foregoing experimental and theoretical studies^[67,154]. The theoretically predicted electronic band structure of monolayer α -In₂Se₃ has been calculated along the high symmetry M- Γ -K-M path (see Fig. 4.1(b), left panel), and an indirect electronic band gap of 0.81 eV obtained through GGA-PBE approach is observed, corroborating with previous studies^[67,140,147,148].

The right side of Fig. 4.1(b) shows the PDOS of monolayer α -In₂Se₃. On the one hand, it is noted that the peaks of PDOS above the Fermi level are mainly ascribed to the In-5s and Se-4p orbitals. On the other hand, the peaks below the Fermi level are mainly associated with Se-4p orbitals. Fig. 4.1 (c) and (d) shows the real-space distributions of the Bloch functions. Whilst the Valence Band (VB) is mainly dominated by Se p orbitals, the Conduction Band (CB) is a mixture of Se s , p and In s orbitals, showing that VB and CB states are spatially separated. Such spatial separation could facilitate HER and OER, improving the photocatalytic properties of the material.

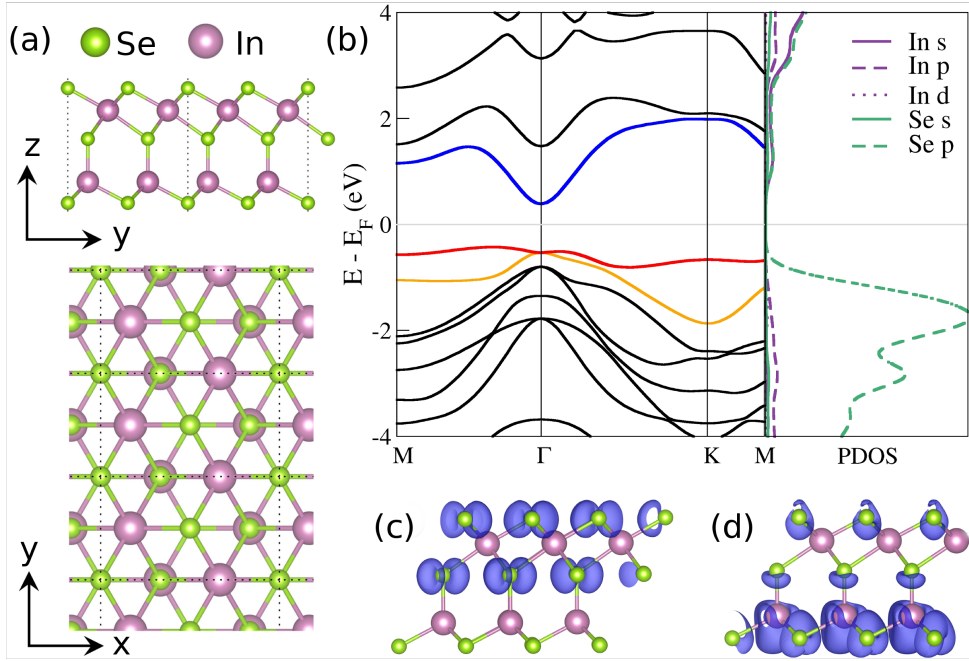


Figure 4.1: Equivalent rectangular geometric structure and band structure of monolayer α -In₂Se₃. (a) Side and top view of the monolayer α -In₂Se₃. The dashed lines delimit the unit cells. (b) GGA-PBE calculated band structure and Partial Density of States (PDOS, in the right) for the unstrained α monolayer. The Fermi level is shifted to energy zero. Real space distribution of the Bloch wave functions of (c) VB and (d) CB along the M- Γ path.

For an unstrained single layer of α -In₂Se₃, we have also performed calculations with the Spin-Orbit Coupling (SOC) to further investigate the electronic properties of this phase. When SOC is included, we observe a splitting of energy bands due to the Rashba effect and the energy levels at Γ are ever so slightly shifted upwards by a few millielectronvolts, causing the gap to now be direct. The difference in energy levels between the band structures with and without SOC is as low as 4 meV, and this has also been reported by other authors^[140].

The effects of external forces applied on the stable 2D α -In₂Se₃ structure are examined. The calculated band structures are shown in Fig. 4.2. In particular, focusing the analysis around the Fermi level, one observes that the Conduction Band Minimum (CBM) of the CB (highlighted in blue) remains at Γ regardless of ε_b . Varying ε_b from -8% up to 6%, CB shifts gradually toward lower energies along M- Γ direction, while shifting upwards along Γ -K direction, leading to a more delocalized band. For the VB (highlighted in red) one observes a reduction of the energy dispersion for both M- Γ and Γ -M direction up to $\varepsilon_b = 2\%$; above this strain the opposite behavior emerges. Additionally, it is also verified that the sub-VB λ states (Fig. 4.2(g), highlighted in orange) and Valence Band Maximum (VBM) are degenerate at the Γ point for all strain considered herein. Regard-

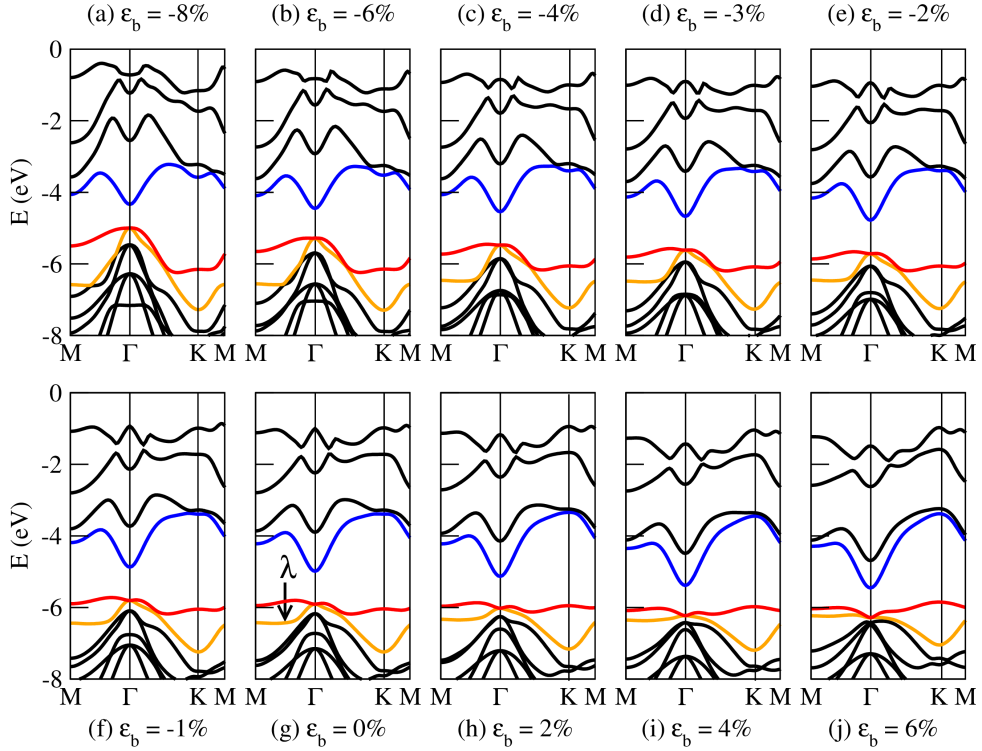


Figure 4.2: GGA-PBE calculated band structures (a)-(j) of α - In_2Se_3 for the different values of ε_b . The blue and red curves are Conduction Band (CB) and Valence Band (VB), respectively. The sub-VB state λ is highlighted in orange. All band structure plots are shifted by their respective vacuum level.

ing the band gap nature, it is worth noting that by going from $\varepsilon_b = +6\%$ to -8% , an indirect to direct transition occurs at $\varepsilon_b = -4\%$.

Fig. 4.3 shows the band gap behavior as a function of the ε_b for the monolayer α - In_2Se_3 , within the GGA-PBE and HSE06 approaches. One can clearly note that the same trend emerges for both GGA-PBE and HSE06 curves, being the GGA-PBE always lower than the corresponding HSE06 values, as expected. In both cases, for a strain ranging from $\varepsilon_b = 6\%$ to -4% , the indirect band gap increases monotonically. In contrast, from $\varepsilon_b = -4\%$ to -8% , the band gap magnitude decreases monotonically, but remaining higher than $\varepsilon_b = 6\%$. In special, an inflection point at $\varepsilon_b = -4\%$ is observed, exactly where an indirect to direct band gap transition occurs.

A detailed lattice dynamics calculation was carried out to verify the structural stability and active Raman modes (see Table IV.1) for different values of ε_b . The calculated peaks of the unstrained α - In_2Se_3 at 93.4 , 173.8 and 188.9 cm^{-1} are attributed to A_1 , A_1 (TO) and A_1 (LO+TO) phonon modes, respectively, in good agreement with experimental^[69,138,155,156] and theoretical^[67,157] reports. Our findings show that the active Raman modes undergo a blue-shift when pressure is applied, as is reported when In_2Se_3 suffers a phase transition from α to β . Additionally, as a increases, the active modes undergo a

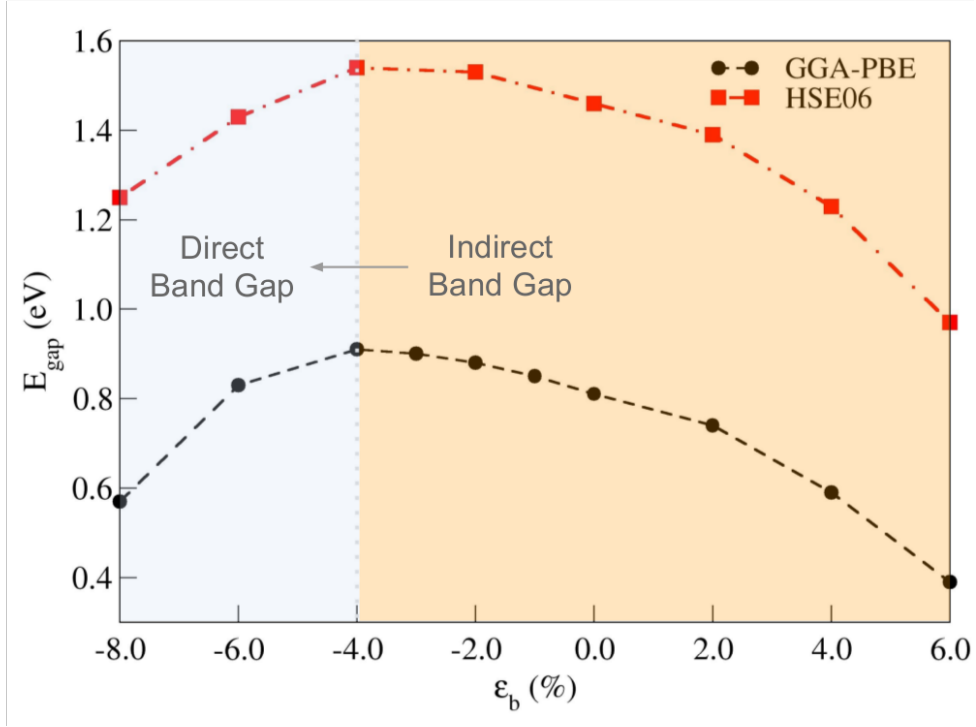


Figure 4.3: GGA-PBE (black circle) and HSE06 (red square) calculated band gap *vs.* in-plane biaxial strain. The dashed line is a guide to the eyes.

red-shift.

Table IV.1: Raman Active Phonons for the α phase for different values of ϵ_b .

ϵ_b (%)	Active Raman Peaks in Γ (cm ⁻¹)		
	A ₁	A ₁ (TO)	A ₁ (TO+LO)
-4	99.0	184.8	205.9
0	93.4	173.8	188.9
4	84.0	159.2	173.4

In₂Se₃ and its homojunctions have been attracting great interest for photocatalytic applications^[26,134]. In this sense, we have systematically studied the biaxial strain dependence of the CBM and VBM position for the 2D α -In₂Se₃ with respect to water reduction and oxidation potentials, using the hybrid HSE06 functional. The obtained band gap was 1.46 eV, which is in accordance with previous reports^[67] and deviates less from experimental values^[69,139], compared with the previously calculated GGA-PBE value.

The demonstrated feasibility of tuning the band gap energy with biaxial strains implies that single-layered α -In₂Se₃ can potentially be designed for usage as a visible-light photocatalyst. It is clearly seen from Fig. 4.4 that the CBM of the 2D structures, for compressive strains from -4% to -8%, is higher than the reduction potential of H⁺/H₂ at a pH value of 0 (the standard potential is $-4.44 + \text{pH} \times 0.059$ eV). Hence, the predicted band gap of 1.46 eV is appropriate for visible-light absorption, and therefore 2D α -In₂Se₃

meets the requirements for photocatalytic hydrogen gas generation. One can also notice that the VBM of the structures within this strain range, except for $\varepsilon_b = -4\%$, sit at higher energy levels than the oxidation potential of $\text{O}_2/\text{H}_2\text{O}$ ($-5.67 + \text{pH} \times 0.059$ eV); as such, a small external bias potential of $0.15 \sim 0.25$ eV ($\varepsilon_b = -6\%$) and $0.4 \sim 0.50$ eV ($\varepsilon_b = -8\%$) is required to enable oxygen evolution in photocatalytic water splitting. Alternatively, a more feasible way to enable hydrogen gas generation and oxygen evolution of 2D α - In_2Se_3 under these strain conditions is to slightly increase the pH levels of the solution. For instance, the adequate pH levels for the considered values of strain would be within the range of 0-3 and 2-4 for $\varepsilon_b = -4$ and -6% , and 7 for $\varepsilon_b = -8\%$, respectively. Our model is an approximation of a neutral surface and neglects solvent effects. It is worth noting

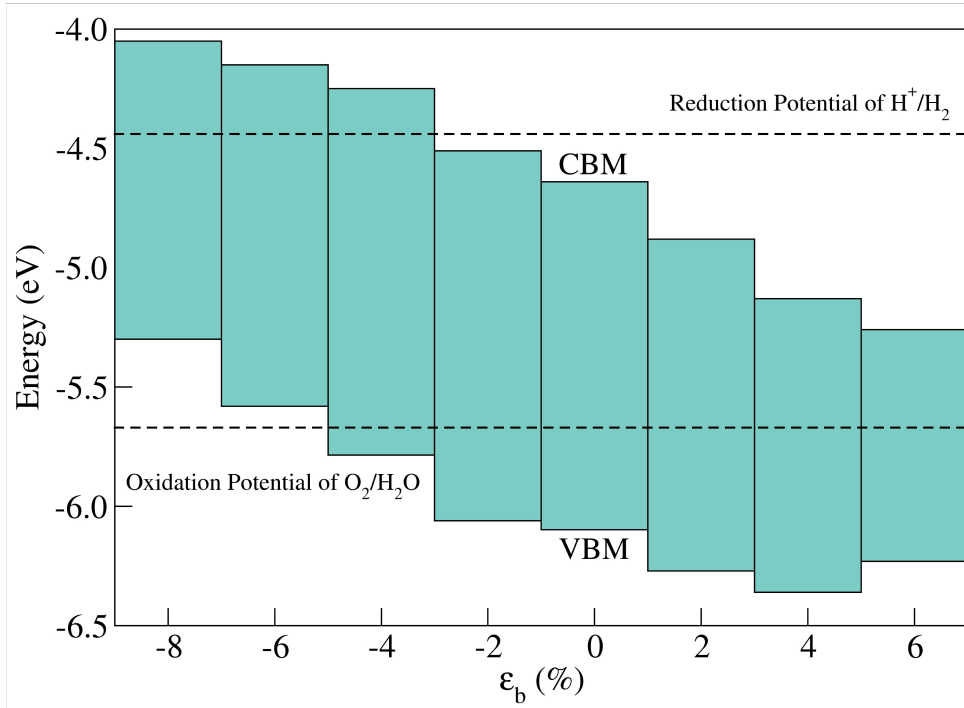


Figure 4.4: HSE06 calculated band edges diagrams of 2D α - In_2Se_3 with respect to the vacuum level. The dashed lines represent the H_2O potentials in a $\text{pH} = 0$ solution. The width of the coloured blocks is a guide to the eyes.

that for a deeper study of the feasibility of manipulating the redox potentials of water by changing pH levels, the approach by Nørskov could be adopted^[158-160], where the water splitting reaction is explicitly treated, but that is not the main focus of this work, since we are using a neutral surface approximation and neglecting solvent effects.

To further assess the photocatalytic water-splitting capabilities of α - In_2Se_3 using visible light, the absorption spectra and effective masses have also been calculated. In Fig. 4.5, we present the optical absorption spectra of α - In_2Se_3 monolayer for ε_b values 0, -4, -6, and -8%. In general, we can observe that for 0, -4, and -6% the spectra present

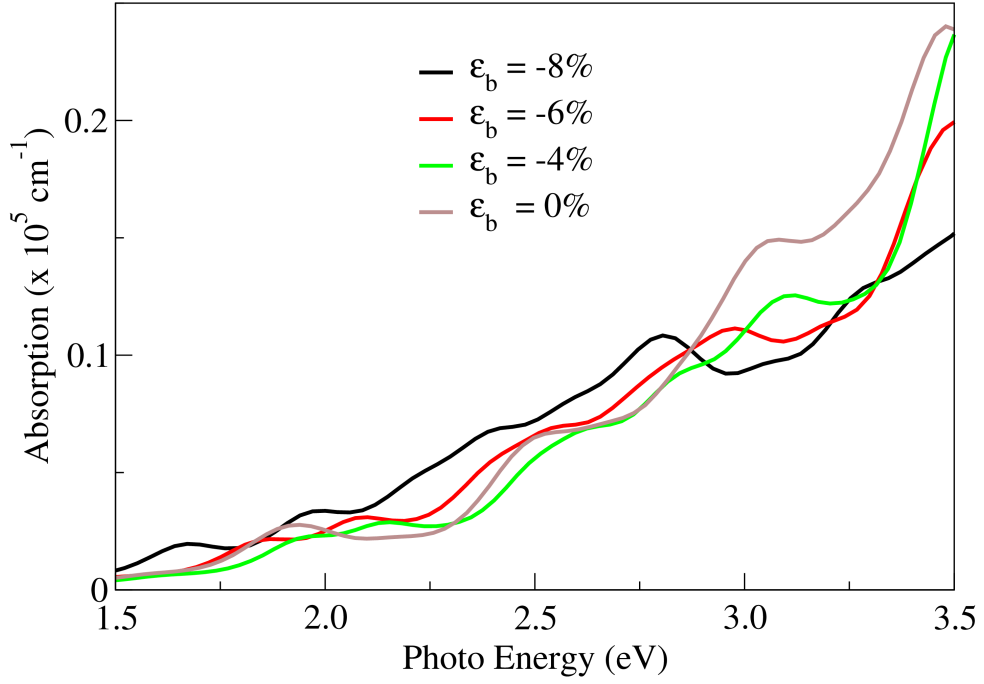


Figure 4.5: Optical absorption spectra of α -In₂Se₃ monolayer in the visible light range for ϵ_b 0, -4 -6, and -8%, based on HSE06 calculations.

a similar photoresponse in the range of visible light. On the one hand, the spectrum for $\epsilon_b = -8\%$ presented a slightly higher absorption compared to others from 1.5 up to 2.9 eV; the absorption edge for this structure is around 1.6 eV. On the other hand, from 2.9 up to 3.5 eV, $\epsilon_b = 0\%$ presents the highest intensity. Overall, our results show that the optical absorption of α -In₂Se₃ monolayer is little affected by relatively small compressive strains. Regarding the change of electron-hole mobility by applying strain, the results show that there is a reduction of electron (hole) effective mass of 59.0% (4.8%), as a compressive strain is applied from 0% \rightarrow -4%. As a result, the photo-generated electrons in the strained structure possess higher mobility with respect to the ones in the unstrained structure, which could favor the two half-reactions of water splitting (O₂/H₂O and H⁺/H₂). For ϵ_b between -2% and +4%, the predicted band gap remains appropriate for visible light absorption, but the CBM is lower than the reduction potential of H⁺/H₂, and thus α -In₂Se₃ becomes unsuitable for hydrogen gas generation. However, the VBM of all structures are lower than the oxidation potential, and therefore these structures remain suitable for oxygen evolution. When the applied strain reaches 6%, the predicted band gap energy is much lower than 1.23 eV and 2D α -In₂Se₃ becomes unsuitable for visible-light photocatalysis. Then, based on these results, considering a pH of 0, the optimal value of the biaxial strain to drive photocatalytic water splitting is -4%.

4.1 Conclusions

In summary, we have performed DFT calculations to explore the electronic structure of monolayer α -In₂Se₃ under biaxial strains. We have demonstrated that two-dimensional In₂Se₃ on its α phase undergoes an indirect-direct gap transition for compressive biaxial strains higher than 4%. Our results also predict that for relatively small strains the calculated band gap increases or decreases monotonically (based on the value of ϵ_b). These biaxial strain studies for α -In₂Se₃ are useful to understand the physical property patterns for two-dimensional layers of this selenide. We have also shown that 2D α -In₂Se₃ is a suitable material as a visible-light photocatalyst in hydrogen gas generation under compressive biaxial strains, and require very small pH values or external bias potentials to drive oxygen evolution in water splitting. These results show that controlled changes in the lattice parameter offer new insight into the technological applications of single-layered α -In₂Se₃ and enhance the photocatalytic activity of this material.

Chapter V

Non-trivial Edge States in Oxygenated Monolayer α -In₂Se₃

This finished work has been published in *ACS Appl. Nano Mater.*
2021, 4, 8154-8161.

Two-dimensional materials, such as graphene^[1,2], have remarkable properties that not only deviate from those of their bulk parent crystals, but can easily be tuned by external stimuli, resulting in their usage in a wide range of applications. However, for reported band gaps below 2.0 eV, their applications in optoelectronic and photoresponsive devices may be hindered in an important range of the electromagnetic spectrum^[161,162]. Furthermore, many of these atomically-thin materials suffer oxygenation and degradation when exposed to ambient conditions^[27,163,164]. For instance, transition metal dichalcogenides, black phosphorus and III₂-IV₃ group layered compounds such as In₂Se₃ samples are known to form surface oxides, which may affect their device performance and degrade surface states^[139,164–167].

Although these findings are somewhat disadvantageous, oxygenation in 2D materials may also lead to more stability and remarkable useful properties. For instance, Zhou *et al.* have shown that monolayer BiN^[168] and black arsenic-phosphorus^[169] display a high performance as two dimensional field-effect transistors and could be potential candidates for next generation electronic devices. Zhong *et al.*^[170] have shown that a honeycomb borophene oxide adopts a stable 2D planar structure and presents a topological phase transition. Zhang^[171] *et al.* have shown that in ultrathin antimonene high concentrations of oxygen atoms drive an indirect-to-direct band gap transition, also inducing non-trivial topological properties. Yang *et al.*^[165] have also shown that monolayer 1T'-WTe₂, a well-

known topological insulator, may maintain its quantum spin Hall (QSH) insulator states with high-coverage oxygen incorporation. Results of this nature spark the interest in the exploitation of oxygenation effects on the electronic properties of different 2D materials.

Among these, a candidate under thorough research is α -In₂Se₃, a layered noncentrosymmetric van der Waals^[154] semiconductor that has been predicted and shown^[69] to have a sizable indirect band gap suitable for various applications in optoelectronics^[26,67], photocatalysis, or pollutant removal^[134]. The breaking of centrosymmetry leads to a spontaneous out-of-plane polarization^[67] that is switchable by an applied electric field. In general, the emergence of electric polarization demands breaking of the structural centrosymmetry in the polarization direction. Several recent experiments with SnTe^[172], In₂Se₃^[68,69,173] binary oxides such as ZrO₂^[174] and HfO₂, and group-V materials^[175] show that the ferroelectricity in these van der Waals 2D crystals can be strong enough and survive thickness limitation. Recently, by density functional theory (DFT) calculations, Zhang *et al.* explored the heterobilayer of β -phase antimonene and ferroelectric In₂Se₃ and demonstrated a strong coupling between topological and ferroelectric order, where the change of ferroelectric polarization causes a switch between trivial and non-trivial topological phases^[60]. Similar results were also recently reported by Bai *et al.*^[176], where a topological switching is achieved in Bi(111)-In₂Se₃ heterostructures by reversing the electric polarization of the selenide substrate. These findings further elucidate the interplay between ferroelectricity and nontrivial topological characters in a large class of materials, since both properties are tied to structural symmetries, and fundamental understanding of their relationship could pave the way for new generation devices.

Here we demonstrate through DFT calculations the coexistence of spontaneous electronic polarization and a topologically non-trivial phase in α -In₂Se₃O by incorporation of oxygen atoms onto its surface. The non-centrosymmetric structure and intrinsic polarization, paired with spin-orbit coupling (SOC) and surface oxygenation render α -In₂Se₃O a 2D TI. As such, our predictions open new possibilities for the exploitation of 2D semiconductors in the next generation of nanodevices.

Similarly to the previous chapter, Fig. 5.1a shows the fully relaxed crystal structure of pristine single-layer α -In₂Se₃. The α phase of this selenide is a semiconductor with indirect band gap and each unit cell is composed of one-atom sheets sequenced as Se⁽¹⁾-In⁽¹⁾-Se⁽²⁾-In⁽²⁾-Se⁽³⁾, as depicted in Fig. 5.1a. The optimized lattice constant is 4.11 Å with the total height of each quintuple layer of around 6.75 Å and the In-Se covalent bond lengths vary between 2.90 and 2.71 Å for the outermost Se-In-Se layers.

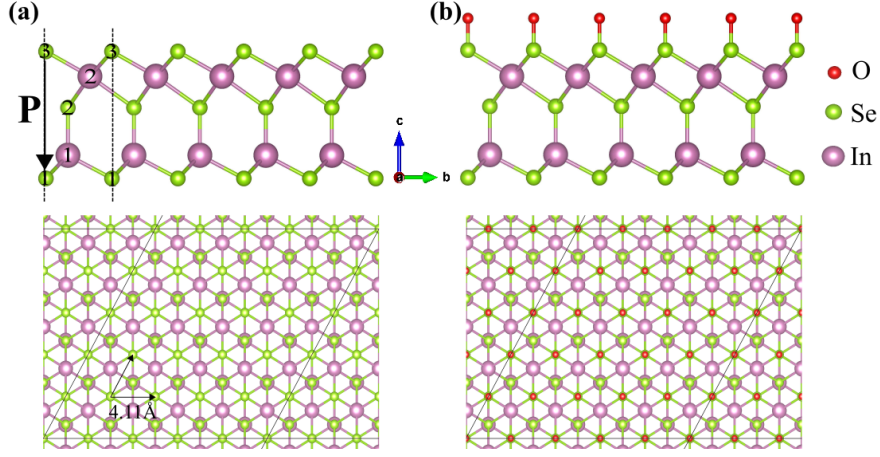


Figure 5.1: (a) Side and top views of the atomic structure of monolayer $\alpha\text{-In}_2\text{Se}_3$, with the electric polarization pointing downwards along the c -axis. (b) Side and top views of its 5×5 supercell with oxygen atoms adsorbed on surface Se atoms. In, Se and O atoms are represented by purple, green and red circles, respectively. The dashed lines delimit one unit cell within the structure.

Next, we investigated the energetic stability and the changes on electronic properties of $\alpha\text{-In}_2\text{Se}_3$ under oxygen incorporation. To this end, we constructed a $5\times 5\times 1$ supercell to explore several adsorption configurations and calculated the corresponding binding energies (normalized per O atom) as $E_b = E_{\text{sys.}} - (E_{\text{In}_2\text{Se}_3} + nE_O)$, where $E_{\text{sys.}}$ is the total energy of the system, n is the number of surface oxygen atoms, $E_{\text{In}_2\text{Se}_3}$ is total energy of the bare semiconductor and E_o is the reference energy of an oxygen atom from different sources, and more details regarding these are discussed below.

Initially, we surveyed the interaction between oxygen molecules and surface. As a molecule approaches the surface, the total energies of its singlet and triplet become degenerate for distances smaller than 2.0 \AA . For a better understanding of the interaction, we have used the Nudged Elastic Band (NEB) method, as implemented in the QE package. An oxygen molecule is adsorbed onto the surface as an initial configuration (A1), and the resulting dissociated pair of oxygen atoms are then bonded to surface Se atoms as a final configuration (A7). For the reaction pathway investigated (A1-A7), a molecule in its singlet state results in a favorable reaction and an energy barrier of 0.47 eV is found.

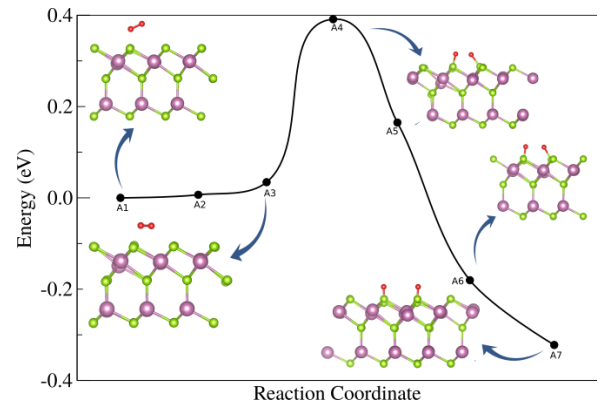


Figure 5.2: Dissociation reaction path of a O_2 on the surface of monolayer $\alpha\text{-In}_2\text{Se}_3$.

Coverage (%)	E_b /atom (eV)		
	atomic oxygen	O ₂ molecule	H ₂ O molecule
4	-2.80	-0.25	+2.77
8	-2.78	-0.23	+2.79
16	-2.74	-0.19	+2.84
20	-2.73	-0.19	+2.84
24	-2.71	-0.16	+2.87
32	-2.68	-0.13	+2.90
36	-2.67	-0.12	+2.91
48	-2.65	-0.10	+2.92
100	-2.46	+0.09	+3.11

Table V.1: The binding energies per oxygen atom from different sources: an atomic oxygen source (in a triplet spin state), a O₂ molecule source (in its singlet spin state) and a H₂O molecule.

Additionally, we have explored the full oxygenation of the top (see Fig. 5.1b) and bottom Se layers of 2D α -In₂Se₃, and the total energy difference between the two cases is $\Delta E = E_{\text{top}} - E_{\text{bottom}} = -0.43$ eV, hence on-top oxygenation is more favorable. As previously mentioned, the α phase of this selenide has a spontaneous out-of-plane electric polarization^[67] due to the absence of centrosymmetry, resulting in an electron-rich (hole-rich) Se top (bottom) layer, which is consistent with the preferred top layer oxygenation. As such, any mentions of oxygenation throughout the text refer only to the top Se layer.

The oxygen binding energies were calculated with respect to common sources such as: (i) an O₂ molecule and (ii) an isolated atomic oxygen. For source (i), using half the energy of an isolated oxygen molecule in a singlet state, E_b ranges from -0.23 (4%) to +0.09 (100%) eV. In case (ii) we have calculated E_b of an isolated oxygen atom in a triplet state. Foster *et al.*^[177,178] and Crocombette^[179] have also done so by using periodic rectangular cells with varying lattice parameters exceeding 10 Å, but in our present work the supercell is large enough to obtain the same results. By doing so, an isolated oxygen atom in a triplet state is slightly more stable than otherwise, and the resulting binding energies are shown in Table V.1.

To determine whether or not surface oxygenation had any form of selectivity, several oxygen configurations for different concentrations were considered. For a given concentration, some configurations were considered and the results indicate that they are energetically equivalent. In all schemes explored, from 4 to 36% of surface coverage the lattice parameter was kept fixed. The relaxed Se-O bond lengths, once a molecule was dissociated, range in between 1.68 and 1.70 Å with increasing surface coverage levels. Based on the binding energy data, all configurations are energetically stable and the oxy-

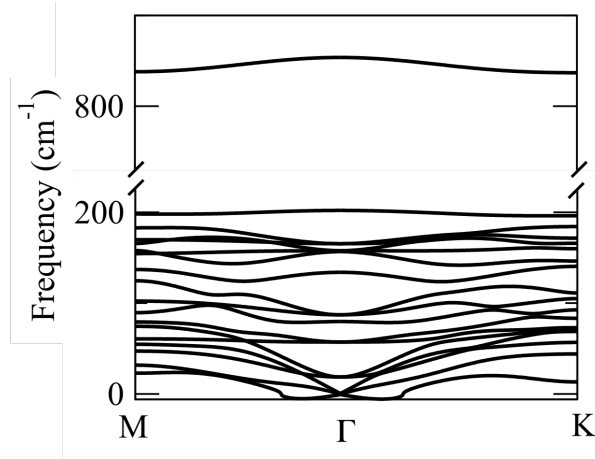


Figure 5.3: Phonon dispersion for α -In₂Se₃ with full passivation of Se surface sites by oxygen atoms.

generation might be uniform, as is the case for epitaxial graphene under Ultrahigh vacuum (UHV) exposure^[180].

The fully oxygenated structure turned out to be structurally stable based on its phonon dispersion spectrum along the high-symmetry M- Γ -K path (see Fig. 5.3), since there are no soft modes along the Brillouin zone, indicating that this oxide is dynamically stable.

In summary, the surface of α -In₂Se₃ is reactive to oxygen species, as reported both experimental^[139] and theoretically^[64] in α -In₂Se₃ nanosheets. Additionally, the intrinsic polarization is enhanced due to the charge redistribution between Se layers, however the degenerate ground states with opposite electric polarizations achieved by displacement of the central Se atom in the pristine structure is broken once oxygen is adsorbed^[67]. In fact, the equivalent final state is energetically less stable and its electronic polarization does not switch. As such, we conclude that although the spontaneous polarization is preserved, the ferroelectric nature of α -In₂Se₃ is lost in α -In₂Se₃O. The GGA-PBE calculated magnitudes of the electric dipoles using the Berry phase approach is 0.14 eÅ per unit cell, in good agreement with previous reports^[67]; when oxygen is adsorbed, the dipole magnitude is increased to 0.88 eÅ. We also note that the in-plane electric polarization along the [110] direction is preserved with oxygen adsorption, and its magnitude was calculated to be 1.34 eÅ per unit cell. It is important to emphasize that oxygen incorporation in other 2D materials, such as hexagonal borophene^[170,181], antimonene^[171] and phosphorene^[182] has been observed and could be used to further encourage efforts for experimental synthesis of this system.

Previous studies have shown that strain engineering and surface oxygenation are

effective methods for modulating the electronic structure of low dimensional materials^[59,181,183]. For a better understanding of how the surface oxygenation process impacts the electronic properties of α -In₂Se₃, we calculated the band structures of 2D α -In₂Se₃O and its individual (Se and O) orbital projections along the high-symmetry path M- Γ -K-M. Pristine 2D α -In₂Se₃ is an indirect band gap semiconductor with a band gap of 0.81 eV at the PBE level ($E_{\text{gap}} = 1.46$ eV, as calculated with the HSE06 functional^[67,140,148]) with the Conduction Band Minimum (CBM) located at Γ and the Valence Band Maximum (VBM) located along the M- Γ path.

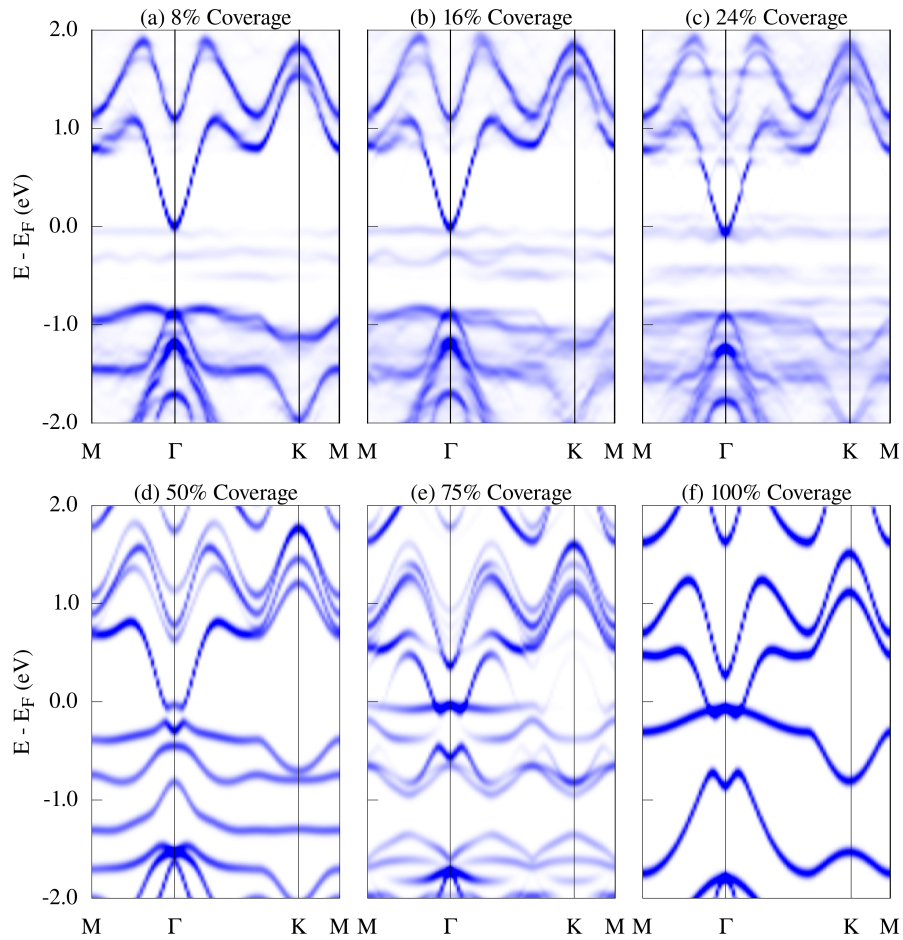


Figure 5.4: Effective electronic band structures of α -In₂Se₃ with increasing surface oxygen coverage along the M- Γ -K-M high-symmetry path. (a)-(c) Low coverage regime. An indirect-to-direct gap nature transition is observed as oxygen concentration is raised. (d)-(f) High coverage regime. Band inversion occurs and α -In₂Se₃O becomes gapless at maximum concentration. All Fermi levels are shifted to zero energy.

It has also been demonstrated that in α -In₂Se₃, an indirect-to-direct band gap and band inversion takes place in the vicinity of Γ when uniaxial or biaxial tensile strains larger than 11% are applied^[59]. SOC effect opens up a gap of 110 meV at the band

crossing, the band structure finally exhibiting features of a two-dimensional topological insulator. Taking into account the nature of the transition with tensile strains, we expect that surface oxygenation with large surface area coverage could also lead to a conversion into a 2D topological insulator of α -In₂Se₃. Indeed, high oxygen concentrations result in the emergence of direct band gap α -In₂Se₃ oxides, with both VBM and CBM located at Γ .

The unfolded effective band structures for increasing oxygen concentrations are plotted in Fig. 5.4, while the detailed orbital projections are shown in Fig. 5.5a-h. First we note, at low concentrations (Fig. 5.4a-c), the appearance of shadow bands in the band gap (see Fig. 5.5a-d) attributed to oxygen atoms, with the CBM gradually shifting downwards in energy as oxygen concentration raises. Strikingly, as surface coverage reaches levels above 50% (Fig. 5.4d-f), there is an anti-crossing of bands at Γ near the Fermi level as a result of a band inversion process. The conduction band, mainly composed of Se p_z and In s orbitals (Fig. 5.5a-d) sinks below the newly formed Se-O p_x band around E_F , as shown in Fig. 5.5e-h for maximum O concentration. We can attribute the raising of the p_x band to the charge transfer of surface Se atoms to O atoms due to the strong electronegativity of the latter. Importantly, as the band inversion develops, a strong hybridization opens a 0.67 eV gap. Simultaneously, the valence band, mainly composed of p_y orbitals of top surface Se atoms (see Fig. 5.5b-c), is extinguished, being substituted by a lower-energy band as the VBM at Γ with p_x character (Fig. 5.5h). We can attribute this disappearance to the strong chemical bond between p_y orbitals of top surface Se⁽³⁾ and O atoms, which forms a pair of bonding-antibonding bands. In fact, for maximum O concentration the anti-bonding band is clearly visible as a fairly flat band below the Fermi level. The orbital character of this band is shown in Fig. 5.5g-h.

To further confirm the band topological properties of 2D oxygenated In₂Se₃, the \mathbb{Z}_2 topological invariant was calculated. The invariant can be determined by the parity method if the system has inversion and time-reversal symmetry. However, α -In₂Se₃ is noncentrosymmetric, as mentioned and therefore, the topological invariant was calculated based on the evolution of the Wannier function center (WFC) in reciprocal space. The tight-binding Hamiltonian of the semi-infinite system was constructed by maximally localized Wannier functions (MLWFs)^[123,124]. As the energy bands near the Fermi level are predominantly composed of hybridized p_z , $p_{x,y}$ and s orbitals, the MLWFs are mainly composed of s and p -like atomic orbitals of In and p -like atomic orbitals of Se and O atoms generated by first-principles calculations.

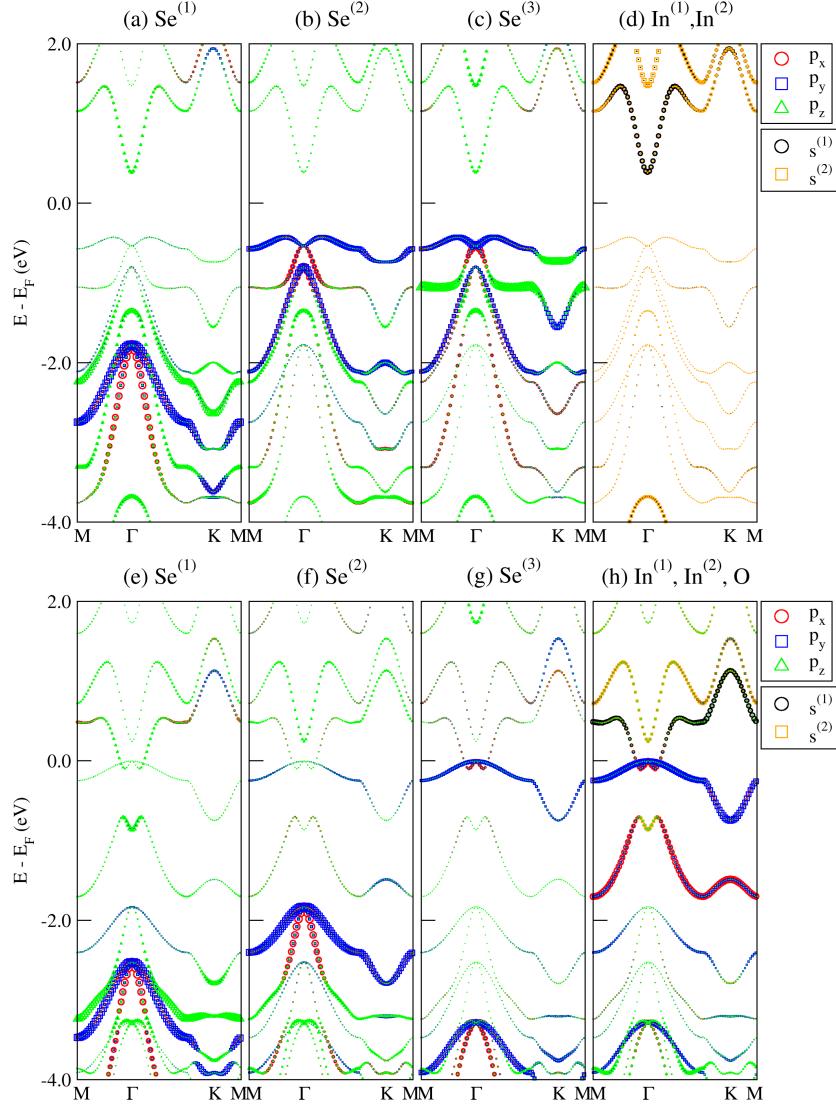


Figure 5.5: Orbital-resolved electronic band structure of pristine (a)-(d) and fully oxygenated α -In₂Se₃ (e)-(h) split into contributions from each atom. Orbitals are represented by different colors and sizes according to their respective contribution to a given band. The incorporation of oxygen into the system to hybridization and band inversion between Se⁽¹⁾-p_z, In⁽¹⁾-s, In⁽²⁾-s, Se⁽³⁾-p_y and O-p_{x,y} orbitals. All Fermi levels are shifted to zero energy.

The occupied WFC's as a function of k_y are given in the unit of lattice constant a in Fig. 5.7a. The topological insulator phase is distinguished from the normal insulator (NI) phase by the variation in the WFCs. It is clear that Z_2 equals 1 as the reference line is crossed an odd number of times by the evolution curves, indicating the non-trivial topology of 2D In₂Se₃O. To verify the existence of gapless edge states, we calculated the band structure of a semi-infinite system employing the Green's function method with spin-orbit coupling and tight binding parameters from QE and Wannier90^[123,124,184], as shown in Fig. 5.7b. The surface local density of states was calculated by employing the WannierTools package^[103] using the maximally localized Wannier functions obtained. It

can be clearly seen that the edge states occur in the bulk band gap and cross linearly at the Γ point that is topological in origin, since it connects bulk valence and conduction bands, which implies that the surface oxygenated In_2Se_3 is indeed a 2D TI.

The computation of the \mathbb{Z}_2 invariant has thus confirmed that oxygenation is indeed responsible for the appearance of a non-trivial topological phase, although our system is gapless due to the presence of the p_y crossing the band-inverted gap in the whole BZ. This band may hamper the observation of physical quantities associated with the protected edge states (e.g., quantized conductance). However, SOC opens a small but sizable indirect gap of 61 meV (0.41 eV as calculated by HSE06) around the Fermi level at Γ , $\text{In}_2\text{Se}_3\text{O}$ displaying now an insulating character enough to allow for such observation. This induced transition of a gapless semiconductor to insulator by spin-orbit coupling is also observed in a number of 2D materials, such as antimonene^[181], SiTe and BiAs thin films^[185,186]. Also, we note that due to the flatness of the p_y band on a large portion of the BZ. Flat bands are prone to electronic localization because the velocity of the carriers is too small and the mass is too high. In the sense of Anderson localization in two dimensions, they scale with the size towards an insulator much faster than standard parabolic-bands carriers. As such, just a small deficiency of O atoms will be enough to induce localization in this band, reducing its influence on transport properties.

To illustrate the possible applications of 2D oxygenated In_2Se_3 as a FETI, we investigate how the topological phase transition might be tuned by an applied electric field. As shown in Fig. 5.7c, oxygenated In_2Se_3 is topologically non-trivial ($\mathbb{Z}_2 = 1$) when $E_\perp = 0$. By applying a gradually increasing perpendicular field (E_\perp), we see that the gap closes at $E_\perp = 0.15 \text{ V/\AA}$ and the system transitions into a metallic state; however, this phase transition does not affect the inverted bands at Γ ; thus, the topological character is preserved. The \mathbb{Z}_2 invariant remains 1 beyond the gap-closing point until $E_\perp = 0.2 \text{ V/\AA}$, above which \mathbb{Z}_2 equals zero, and the topological character is lost. Conversely, for negative values, applying a moderate electric field completely closes the band gap ($E_\perp \approx -0.20 \text{ V/\AA}$) and re-opens it as a conventional gap of $\approx 200 \text{ meV}$ at $E_\perp = -0.25 \text{ V/\AA}$ transforming

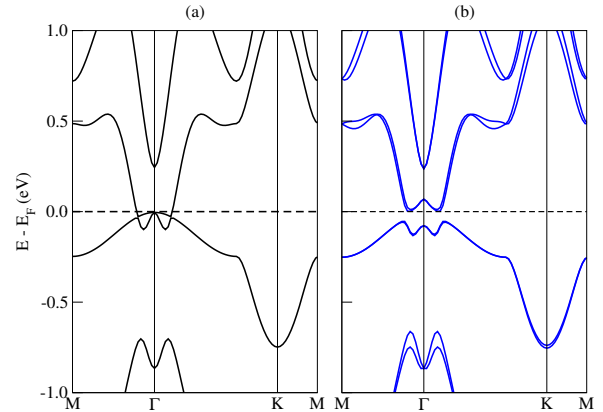


Figure 5.6: Band structure of monolayer $\alpha\text{-In}_2\text{Se}_3$ (a) without SOC and (b) with SOC. A gap of 61 meV opens up around E_F .

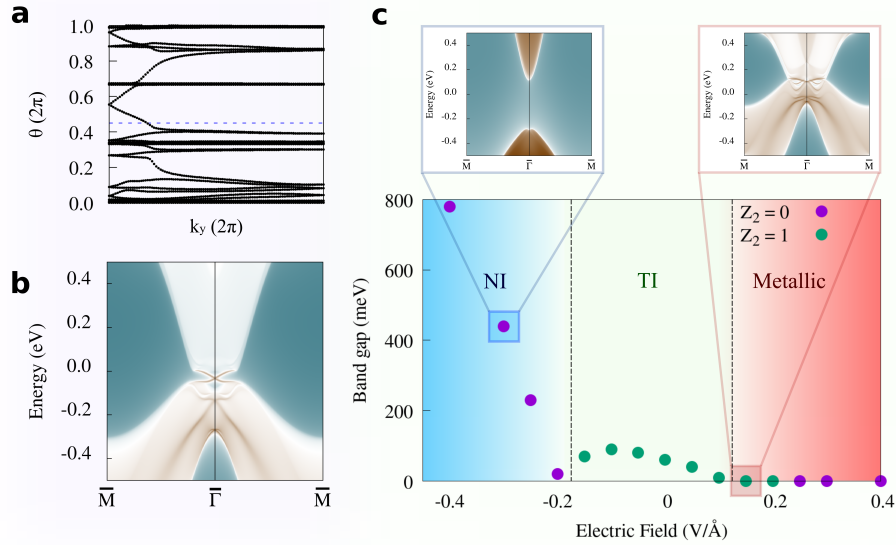


Figure 5.7: (a) Evolution of the Wannier centers along k_y which indicate a non-trivial invariant ($Z_2 = 1$) for the bulk band structure in oxygenated two-dimensional α -In₂Se₃. The evolution lines cross the arbitrary reference line (blue dashed line parallel to k_y) an odd number of times. (b) Projected edge spectrum (edge along the $[100]$ direction), where Z_2 topological edge states can be observed in the energy gaps. (c) Band gap as a function of external electric field applied in the out-of-plane direction. The insets show regions where the electric field drives a transition into a normal insulator or into a metallic state. Brown and white curves represent higher and lower spectral weight, respectively.

the system into a trivial insulator ($Z_2 = 0$) and thus the edge conduction is lost. We also notice that, as expected, and because a topological invariant is robust under continuous deformation (it is a global property in the entire BZ), a small E_{\perp} cannot affect the Z_2 invariant of the system, unless a singularity or a gap-closing point is encountered^[187,188].

The above findings show the coexistence of intrinsic electric polarization and quantum spin Hall effect in a 2D material and point to the possibility to make a field-effect topological transistor that could manipulate both spin and charge carrier simultaneously, that, in practice, would imply an all-electrical control of the on (off) charge (spin) conductance of helical edge states. The large non-trivial band gap not only ensures the coexistence of intrinsic electric polarization and the non-trivial topology, but also facilitates the observation of the QSH effect at room temperature.

5.1 Conclusions

In this work, we have discovered the conversion of single-layer α -In₂Se₃ into a stable 2D topological insulator by the process of oxygen incorporation into its surface.

The oxygenation may be promoted with the existence of O₂ molecules or atomic oxygen. Single-layer α -In₂Se₃ displays a topological insulating state with non-trivial band topology once surface oxygen coverage levels are above 50%. Remarkably, the fully oxygenated system displays non-trivial edge states while also retaining its out-of-plane spontaneous electric polarization rendering α -In₂Se₃O a stable 2D topological insulator. In addition, we have demonstrated the feasibility of controlling the topological phase by field-effect switching. The large band gaps in both the conventional and topological phases, much greater than the thermal energy at room temperature (≈ 25 meV), suggest that monolayer In₂Se₃O is suitable for practical next generation topological transistor devices.

Chapter VI

Final Remarks

In summary, we were able to carry out a thorough investigation on single-layers of two-dimensional semiconductor α - In_2Se_3 within different approaches. One of such approaches was applying strain band-gap engineering to pristine α - In_2Se_3 that yielded fruitful insights into:

- the spatial separation between conduction and valence bands may hinder electron-hole pair recombination rates;
- a change in gap nature due to tensile external strains, meaning no changes in momentum are required;
- its applicability in hydrogen gas generation by photocatalysis is demonstrated for certain pH levels and biaxial strain values;
- its surface is reactive to oxygen even in its pristine structure;
- oxygen incorporation leads to a phase transition of quantum nature into a topological insulator;
- its intrinsic electronic polarization is considerably enhanced in this process, however its ferroelectric nature is lost because requirements for the latter are no longer met;

We have further explored the last item and are currently working on another journal publication based on the results. As aforementioned in the first chapter, a ferroelectric material is defined two-fold:

- It possesses intrinsic electronic polarization (P) that is switchable by an applied electric field;

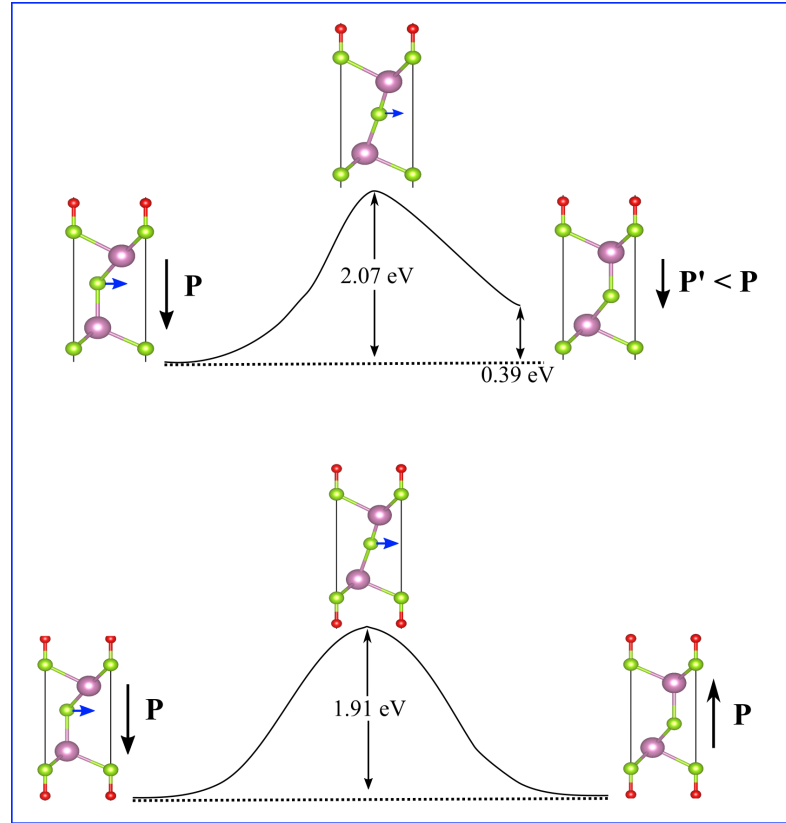


Figure 6.1: Kinetic pathways of polarization reversal processes in 2D $\alpha\text{-In}_2\text{Se}_3\text{O}$ (upper panel) and $\alpha\text{-In}_2\text{Se}_3\text{O}_2$ (bottom panel) layers transforming from the state with the electric polarization pointing downward (left) to the state with the electric polarization pointing upward (right) via a direct shifting process: lateral displacement of central Se atoms, indicated by blue arrows. Reversal does not occur for the first case.

- The ground state has a degenerate equivalent with inverted, but equal in magnitude, \mathbf{P} .

In pristine $\alpha\text{-In}_2\text{Se}_3$ both conditions are simultaneously met. The first condition is met because the central Se atom breaks centrosymmetry. The second condition is achieved by a lateral displacement of said atom as the system is carried out through an intermediate, centrosymmetric phase. When oxygen is adsorbed to its topmost layer, however, although $\alpha\text{-In}_2\text{Se}_3$ retains its spontaneous polarization, the ferroelectric property is lost since the condition that the electronic polarization is switchable is no longer met. In a kinetic pathway of polarization reversal process (Fig. 6.1), the system evolves from its ground state with electronic polarization \mathbf{P} pointing downwards, passing through a metastable centrosymmetric phase, to its previously degenerate final state; however, the electronic polarization vector does not switch and the final phase is energetically less stable by 0.39 eV, as depicted. We were able to show, in a related work under development, that oxygen adsorption on *both* (top and bottom) surfaces is favorable, with a binding energy of -2.32 eV. Furthermore, the non-trivial topological nature of $\alpha\text{-In}_2\text{Se}_3\text{O}$ is preserved, with the

remarkable addition that centrosymmetry is restored. As shown in Fig. 6.1, the degeneracy between initial and final states is restored and both conditions for ferroelectricity are met, rendering *fully* oxygenated $\alpha\text{-In}_2\text{Se}_3\text{O}_2$ a ferroelectric topological insulator.

Appendix A

Adiabatic Dynamics

Let \mathcal{H} be the time-dependent Hamiltonian defined in Eq. 2.7. If the parameter $\mathbf{R} = (R_1, R_2, \dots, R_N)$ does not change in time, after a full cycle the wave function will have evolved as $|\Psi(t)\rangle = e^{-iE_n\Delta t/\hbar} |u(\mathbf{R})\rangle$. That is, in the continuous limit, the evolution of Ψ will be given by

$$|\Psi(t)\rangle = \exp\left\{\frac{-i}{\hbar} \int_0^t dt' E_n(t')\right\} |u(\mathbf{R}(t))\rangle, \quad (\text{A.1})$$

where $\phi_n(t) = \frac{-1}{\hbar} \int_0^t dt' E_n(t')$ is a *dynamic phase* of the system that extends the usual phase factor for the case where the eigenenergies E_n are time-dependent. However, the adiabatic theorem states that when the Hamiltonian is deformed gradually, a particle in its n -th eigenstate will remain in it up to a time-dependent phase factor, even if the wave function as a whole evolves. Thus, the above expression becomes:¹

$$|\Psi(t)\rangle = |u(t)\rangle e^{i\phi_n(t)} e^{i\gamma_n(t)}, \quad (\text{A.2})$$

where $\gamma_n(t)$ is denoted as an arbitrary geometric phase acquired by the system during a cycle. As such, when we plug $|\Psi(t)\rangle$, Eq. A.2, into the wave equation, we have

$$i\hbar \left[|\dot{u}(t)\rangle e^{i\phi_n(t)} e^{i\gamma_n(t)} - \frac{i}{\hbar} E_n |u(t)\rangle e^{i\phi_n(t)} e^{i\gamma_n(t)} + i\dot{\gamma}_n |u(t)\rangle e^{i\phi_n(t)} e^{i\gamma_n(t)} \right] = \mathcal{H} |\Psi(t)\rangle,$$

from which it is easy to see that

$$\dot{\gamma}_n |u_n(t)\rangle + i |\dot{u}_n(t)\rangle = 0. \quad (\text{A.3})$$

¹The dependence of $\mathbf{R}(t)$ of the vectors $|u(\mathbf{R}(t))\rangle$ is omitted for simplicity.

Since the ket $|u_n(t)\rangle$ varies in time according with its dependence on $\mathbf{R}(t)$, we may use the product rule to rewrite the time derivative to the left as $|\dot{u}_n(t)\rangle = \nabla_{\mathbf{R}} |u_n(t)\rangle \cdot \dot{\mathbf{R}}$, thus obtaining, through the inner product with some eigenvector $\langle u_m|$:

$$\dot{\gamma}_n \langle u_m | u_n \rangle = i \langle u_m | \nabla_{\mathbf{R}} | u_n \rangle \dot{\mathbf{R}}. \quad (\text{A.4})$$

In particular, in a cyclic process along a path in parameter space, in which the initial and final states are identical, and using $d\mathbf{R} = \dot{\mathbf{R}}dt$ combined with basis eigenvectors orthonormality, we may finally rewrite $\gamma_n(t)$ as

$$\boxed{\gamma_n(t) = \int_{R(0)}^{R(t)} d\mathbf{R} \langle u_n(\mathbf{R}) | \nabla_{\mathbf{R}} | u_n(\mathbf{R}) \rangle}. \quad (\text{A.5})$$

Appendix B

Wannier Functions

Wannier functions represent an alternative to the description of Bloch functions, in the form of localized orbitals in real space with exponential decay as the distance from the point at which they are defined increases. Such functions are specially useful in electronic structure calculations as they pose as a localized basis set for the construction of Hamiltonians, as well as being widely used in the modern theory of electronic polarization^[189,190]. For a given set of states $|\psi_{n,\mathbf{k}}\rangle$ of cell-periodic Bloch functions $|u_{n,\mathbf{k}}\rangle$, it follows that $|\psi_{n,\mathbf{k}}\rangle = e^{i\mathbf{k}\cdot\mathbf{R}} |u_{n,\mathbf{k}}\rangle$, so that we may define Wannier functions associated with each unit cell with lattice vector \mathbf{R} as

$$|\mathbf{R}, n\rangle = \frac{V}{(2\pi)^3} \int_{\text{BZ}} d^3\mathbf{k} e^{-i\mathbf{k}\cdot\mathbf{R}} |u_{n,\mathbf{k}}\rangle. \quad (\text{B.1})$$

While Bloch functions are defined up to a phase, Wannier functions are not unique as they are dependent on the choices of $|u_{n,\mathbf{k}}\rangle$. This indeterminacy is more general than a phase factor for each \mathbf{k} point; Bloch functions belonging to isolated bands may undergo unitary transformations $U^{(\mathbf{k})}$ among each other. By transforming the manifold of occupied electronic states into a set of maximum localized Wannier functions (MLWFs) it is possible to study additional properties of a system by analyzing the changes in the so-called ‘‘Wannier charge centers’’ (WCCs). The WCCs are, roughly, a classical correspondence of electron localization in an insulator, in a quantum context. Furthermore, the vector sum of WCCs may directly be related to the electronic polarization of an insulator^[191]. For a deeper approach the reader is referred to the works by N. Marzari and D. Vanderbilt^[191,192].

From Eq. B.1, it is easy to show that the vectors $|\mathbf{R}, n\rangle$ form an orthonormal basis, since $\langle \mathbf{R}', n | \mathbf{R}, n \rangle = \delta_{\mathbf{R}, \mathbf{R}'}$. The matrix elements of the position operator between Wannier functions at the origin of an unit cell and lattice vector \mathbf{R} take the form

$$\langle \mathbf{R}n | \mathbf{r} | \mathbf{0}m \rangle = i \frac{V}{(2\pi)^3} \int d\mathbf{k} e^{i\mathbf{k}\cdot\mathbf{R}} \langle u_{n\mathbf{k}} | \nabla_{\mathbf{k}} | u_{m\mathbf{k}} \rangle, \quad (\text{B.2})$$

where the reverse relation (assuming a discrete lattice in real space)

$$\langle u_{n\mathbf{k}} | \nabla_{\mathbf{k}} | u_{m\mathbf{k}} \rangle = -i \sum_{\mathbf{R}} e^{-i\mathbf{k}\cdot\mathbf{R}} \langle \mathbf{R}n | \mathbf{r} | \mathbf{0}m \rangle. \quad (\text{B.3})$$

We may even define the expectation value of the square position operator, later to be used to calculate gauge-invariant functional (Ω) that measures the total delocalization of WFs. Recalling that in momentum space $i\nabla_{\mathbf{k}}$, we obtain

$$\langle \mathbf{R}n | r^2 | \mathbf{0}m \rangle = -\frac{V}{(2\pi)^3} \int d\mathbf{k} e^{i\mathbf{k}\cdot\mathbf{R}} \langle u_{n\mathbf{k}} | \nabla_{\mathbf{k}}^2 | u_{m\mathbf{k}} \rangle. \quad (\text{B.4})$$

If we now take the particular case in which the bras and kets represent vectors at the unit cell origin, the expectation values of \mathbf{r} and r^2 , denoted as WCCs, are

$$\langle \mathbf{r} \rangle_n = i \frac{V}{(2\pi)^3} \int d\mathbf{k} e^{i\mathbf{k}\cdot\mathbf{R}} \langle u_{n\mathbf{k}} | \nabla_{\mathbf{k}} | u_{n\mathbf{k}} \rangle, \quad (\text{B.5})$$

$$\langle r^2 \rangle_n = -\frac{V}{(2\pi)^3} \int d\mathbf{k} e^{i\mathbf{k}\cdot\mathbf{R}} | \nabla_{\mathbf{k}} u_{n\mathbf{k}} |^2. \quad (\text{B.6})$$

Finally, we define the functional Ω as the square deviation between the charge centers defined above:

$$\Omega = \sum_n \left(\langle r^2 \rangle_n - \langle \mathbf{r} \rangle_n^2 \right). \quad (\text{B.7})$$

The method to determine a set of maximum localized Wannier functions^[192] is based on finding a choice of unitary transformation $U_m(\mathbf{k})$ in order to minimize the functional (which in turn maximizes the localizability of the functions $|\mathbf{R}, n\rangle$), and more details can be found in Ref. N. Marzari and D. Vanderbilt^[192].

Appendix C

Second Quantization Formalism

The formalism known as second quantization was developed by P. Dirac^[193] in 1927 to describe photons in radiation theory and later extended to fermions by E. Wigner and P. Jordan (1928). This algebra in no way assumes the existence of a “first” quantization and presents a compact notation to study many-body systems; in fact, the properties of operators, that may or may not represent observables, are summarized by simple sets of commutation and anticommutation relations, instead of explicit representations of Hilbert spaces^[194,195]. More rigorous and complete descriptions may be found in the literature and for this reason this will be a brief introduction to the formalism.

We begin by considering the normalized set of eigenfunctions $|\alpha\rangle$ of some one-body Hamiltonian $\mathcal{H} : \mathcal{H}m|\alpha\rangle = E_\alpha|\alpha\rangle$. Thus, the normalized two-body eigenfunction (fermions or bosons) occupying states $|\alpha_1\rangle$ e $|\alpha_2\rangle$ is

$$\begin{aligned}\psi_F(x_1, x_2) &= \frac{1}{\sqrt{2}}(\langle x_1|\alpha_1\rangle \langle x_2|\alpha_2\rangle - \langle x_1|\alpha_2\rangle \langle x_2|\alpha_1\rangle), \\ \psi_B(x_1, x_2) &= \frac{1}{\sqrt{2}}(\langle x_1|\alpha_1\rangle \langle x_2|\alpha_2\rangle + \langle x_1|\alpha_2\rangle \langle x_2|\alpha_1\rangle).\end{aligned}\tag{C.1}$$

Note that, by indistinguishability, the symmetrization or antisymmetrization of the wave function becomes necessary: for fermions, the wave function must be antisymmetric and for bosons it must be symmetric. In general, the symmetrized wave function for a system composed of N particles may be expressed as^[194,196]

$$|\alpha_1, \alpha_2, \alpha_3, \dots, \alpha_N\rangle = \frac{1}{\sqrt{N! \prod_\alpha (n_\alpha!)}} \sum_k \eta^{(1-sgn k)/2} |\alpha_{k_1}\rangle \otimes |\alpha_{k_2}\rangle \otimes \dots \otimes |\alpha_{k_N}\rangle, \tag{C.2}$$

where n_α counts the total number of particles in state $|\alpha\rangle$ and $\eta = -1$ for fermions and 1 for bosons. In general, it is assumed that N is sufficiently large since we must somehow guarantee the existence of infinite degrees of freedom. It is noteworthy that Eq. C.2 can be used for a complete representation of a Hilbert space, however its application is quite laborious and in some cases inconvenient, as for example in representations where the individual quantum numbers of each particle are fundamental. The second-quantized formalism presented below is a tool to efficiently work around these difficulties.

3.1 Occupation Number and Fock Space

In the occupation number representation, the basis of a \mathcal{F}^N space are specified by $|n_1, n_2, \dots, n_N\rangle$, where $N = \sum_i n_i$ is, once more, the total number of particles. Thus, any state $|\psi\rangle$ in \mathcal{F}^N can be constructed as a linear superposition of occupation numbers

$$|\psi\rangle = \sum_{n_1, n_2, \dots, \sum n_i = N} c_{n_1, n_2, \dots} |n_1, n_2, \dots\rangle. \quad (\text{C.3})$$

A Hilbert space large enough such that it contains an undetermined number of particles is given by

$$\mathcal{F} \equiv \bigotimes_{N=0}^{\infty} \mathcal{F}^N. \quad (\text{C.4})$$

Note that the $N = 0$ contribution representing a one-dimensional Hilbert space, in which no particle is present, is denoted a vacuum space, $|\text{vac}\rangle$. The space \mathcal{F} is known as a Fock space and in order to obtain its basis we drop the condition $N = \sum_i n_i$ imposed on the occupation numbers and Eq. C.3 can be rewritten as a linear superposition in the form of $|\psi\rangle = \sum_{n_1, n_2, \dots} c_{n_1, n_2, \dots} |n_1, n_2, \dots\rangle$. At this stage, we are yet to obtain an explicit symmetrization or antisymmetrization of the states in \mathcal{F} . To this end, we begin by defining a set of linear operators a^\dagger acting in \mathcal{F} , such that^[194,195]

$$a_i^\dagger |n_1, \dots, n_i, \dots\rangle = (n_i + 1)^{1/2} \eta^{s_i} |n_1, \dots, n_i + 1, \dots\rangle, \quad (\text{C.5})$$

where $s_i = \sum_{j=1}^{i-1} n_j$. By this definition, we can construct *any* basis state in \mathcal{F} by successive applications of a_i^\dagger on the vacuum state. In fact, repeated applications of these linear operators lead to the following fundamental relation:

$$\boxed{|n_1, n_2, \dots\rangle = \prod_i \frac{1}{\sqrt{n_i!}} (a_i^\dagger)^{n_i} |\text{vac}\rangle.} \quad (\text{C.6})$$

From this we conclude that the definition of Fock states of Eq. C.4 may be directly generated by simple application of a set of linear operators in a reference state; the N -th application of a^\dagger in the vacuum state creates a state with N particles, and for this reason the a^\dagger operators are called *creation* operators. For fermions, a_i^\dagger acting on a state where $n_i = 1$ leads to annihilation.

Let us consider now two operators a_i^\dagger and a_j^\dagger , for $i \neq j$; from the definition C.5, we can see directly that $(a_i^\dagger a_j^\dagger \mp a_j^\dagger a_i^\dagger) |n_1, n_2, \dots\rangle = 0$. Since this is true for any basis vector, we arrive at the commutation and anticommutation relations:

$$[a_i^\dagger, a_j^\dagger] = \{a_i^\dagger, a_j^\dagger\} = 0. \quad (\text{C.7})$$

For the $i = j$ case, we note that the above result is unchanged, since for bosons $[a_i^\dagger, a_i^\dagger] = 0$ (identical operators commute), and for fermions $a_i^{\dagger 2} = 0$.

We now need to define the Hermitian adjoint of a_i^\dagger , denoted as $(a_i^\dagger)^\dagger = a_i$; to this end, taking the complex conjugate of C.5:

$$\begin{aligned} \langle n_1, \dots, n_i, \dots | a_i^\dagger | n'_1, \dots, n'_i, \dots \rangle &= (n'_i + 1)^{1/2} \eta^{s'_i} \delta_{n_1, n'_1} \dots \delta_{n_i, n'_i+1}, \dots \\ (\langle n_1, \dots, n_i, \dots | a_i^\dagger | n'_1, \dots, n'_i, \dots \rangle)^* &= \langle n'_1, \dots, n'_i, \dots | a_i | n_1, \dots, n_i, \dots \rangle \\ &= (n'_i + 1)^{1/2} \eta^{s'_i} \delta_{n_1, n'_1} \dots \delta_{n_i, n'_i+1}, \dots \\ &= (n_i)^{1/2} \eta^{s_i} \delta_{n'_1, n_1} \dots \delta_{n'_i+1, n_i} \dots \\ \implies a_i | n_1, \dots, n_i, \dots \rangle &= (n_i)^{1/2} \eta^{s_i} | n_1, \dots, n_i - 1, \dots \rangle. \end{aligned} \quad (\text{C.8})$$

In other words, the complex conjugate of a creation operator represents annihilation. That is to say, creation operators acting on a given state raise its number of particles by 1, whereas annihilation operators lower it by 1; for example, a_i acting on the vacuum state $|\text{vac}\rangle$ destroy it ($a_i |\text{vac}\rangle = 0$). We thus have a set of creation operators and its Hermitian adjoints, and from the relation C.7 combined with the above result we may easily derive the fundamental commutation relations:

$$\boxed{[a_i, a_j^\dagger] = \delta_{ij}, [a_i, a_j] = 0, [a_i^\dagger, a_j^\dagger] = 0.} \quad (\text{C.9})$$

This allows us to construct in a compact form all the symmetrization of a Fock space from the application of a_i^\dagger to a reference state.

We are now in position to explore the algebra of these operators when making a change of basis and how to represent one and two-body operators in a given vectorial basis as a function of the creation and annihilation operators. By using the identity relation $\mathbb{1}$, expansion coefficients when changing basis'^[194,197,198] $\sum_\alpha |\alpha\rangle \langle \alpha| \bar{\alpha}\rangle$ and the previous definitions, we can show that

$$\begin{aligned} a_\alpha^\dagger |0\rangle &= |\alpha\rangle; a_{\bar{\alpha}}^\dagger |0\rangle = |\bar{\alpha}\rangle, \\ \mathbb{1} a_{\bar{\alpha}}^\dagger |0\rangle &= \sum_\alpha |\alpha\rangle \langle \alpha| a_{\bar{\alpha}}^\dagger |0\rangle = \sum_\alpha |\alpha\rangle \langle \alpha| \bar{\alpha}\rangle \\ a_{\bar{\alpha}}^\dagger |0\rangle &= \sum_\alpha \langle \alpha| \bar{\alpha}\rangle a_\alpha^\dagger |0\rangle, \therefore \end{aligned}$$

$$\boxed{a_{\bar{\alpha}}^\dagger = \sum_\alpha \langle \alpha| \bar{\alpha}\rangle a_\alpha^\dagger.} \quad (\text{C.10})$$

Similarly, since $a_{\bar{\alpha}} = (a_{\bar{\alpha}}^\dagger)^\dagger$, then

$$\boxed{a_{\bar{\alpha}} = \sum_\alpha \langle \bar{\alpha}| \alpha\rangle a_\alpha.} \quad (\text{C.11})$$

In cases where we deal with continuous spectra (such as spatial coordinates or momentum space), the projections are represented by integrals and the indices are usually omitted. For example, in a one-dimensional system, the annihilation operator in coordinates basis would take the form $a_\alpha = \int dx \psi_\alpha(x) a(x)$.

3.2 One and Two-body Representation

We are now ready to represent any operator \mathcal{P} in any basis, given we are able to construct any Hilbert space from the field operators. For simplicity, we search for a representation where a one-body operator is diagonal in a given basis. For such, we first define the occupation number operator:

$$\boxed{\mathbf{n}_\alpha = a_\alpha^\dagger a_\alpha.} \quad (\text{C.12})$$

It is easy to deduct that \mathbf{n} commutes with a^\dagger, a , and for this reason \mathbf{n} counts the

number of particles in a state α , that is to say $\mathbf{n}_\alpha (a_\alpha^\dagger)^n |0\rangle = n (a_\alpha^\dagger)^n |0\rangle$, or in a more explicit form, $\mathbf{n}_{\alpha_j} |n_{\alpha_1}, n_{\alpha_2}, \dots\rangle = n_{\alpha_j} |n_{\alpha_1}, n_{\alpha_2}, \dots\rangle$. Let us now consider an operator $\mathcal{P}_1 : \mathbf{p} = \sum_i p_{\alpha_i} |\alpha_i\rangle \langle \alpha_i|$ such that $p_{\alpha_i} = \langle \alpha_i | \mathbf{p} | \alpha_i \rangle$. The matrix elements of \mathcal{P} are:

$$\begin{aligned} \langle n'_{\alpha_1}, n'_{\alpha_2}, \dots | \mathcal{P}_1 | n_{\alpha_1}, n_{\alpha_2}, \dots \rangle &= \sum_i \langle n'_{\alpha_1}, n'_{\alpha_2}, \dots | \mathbf{p}_1 | n_{\alpha_1}, n_{\alpha_2}, \dots \rangle \\ &= \sum_i p_{\alpha_i} n_{\alpha_i} \langle n'_{\alpha_1}, n'_{\alpha_2}, \dots | n_{\alpha_1}, n_{\alpha_2}, \dots \rangle \\ &= \langle n'_{\alpha_1}, n'_{\alpha_2}, \dots | \sum_i p_{\alpha_i} n_{\alpha_i} | n_{\alpha_1}, n_{\alpha_2}, \dots \rangle \end{aligned}$$

But, since $n_{\alpha_i} |n_{\alpha_1}, \dots\rangle = \mathbf{n}_{\alpha_i} |n_{\alpha_1}, \dots\rangle$, we then obtain

$$\langle n'_{\alpha_1}, n'_{\alpha_2}, \dots | \mathcal{P}_1 | n_{\alpha_1}, n_{\alpha_2}, \dots \rangle = \langle n'_{\alpha_1}, n'_{\alpha_2}, \dots | \sum_i p_{\alpha_i} \hat{n}_{\alpha_i} | n_{\alpha_1}, n_{\alpha_2}, \dots \rangle.$$

Because this result must hold true for any set of states, we may infer that the representation for an operator \mathcal{P} is given by

$$\boxed{\mathcal{P}_1 = \sum_{\alpha} p_{\alpha} \hat{n}_{\alpha} = \sum_{\alpha} \langle \alpha | \mathbf{p} | \alpha \rangle a_{\alpha}^{\dagger} a_{\alpha}.} \quad (\text{C.13})$$

In other words, a one-body operator counts the number of particles in a state α , multiplied by its corresponding eigenvalue in the diagonal representation. In general, in a generic basis $\{\mu, \nu\}$, we have:

$$\boxed{\mathcal{P}_1 = \sum_{\mu\nu} \langle \mu | \mathbf{p} | \nu \rangle a_{\mu}^{\dagger} a_{\nu} = \sum_{\mu\nu} p_{\mu\nu} a_{\mu}^{\dagger} a_{\nu}.} \quad (\text{C.14})$$

We now seek the representation of Hermitian operators in a generic basis in the a^\dagger -representation, so that we are able to describe pair-to-pair interactions between particles. However, due to indistinguishability between the latter, this is a laborious task. The previous result may be generalized for two-particle operators^[194] as:

$$\boxed{\mathcal{P}_2 = \sum_{\mu\mu'\nu\nu'} \langle \mu\mu' | \mathcal{P}_2 | \nu\nu' \rangle a_{\mu}^{\dagger} a_{\nu} a_{\mu'}^{\dagger} a_{\nu'} = \sum_{\mu\mu'\nu\nu'} \mathcal{P}_{\mu\mu'\nu\nu'} a_{\mu}^{\dagger} a_{\nu} a_{\mu'}^{\dagger} a_{\nu'}.} \quad (\text{C.15})$$

We may now write *any* one or two-body operator in *any* arbitrary basis of interest, as long as we know how these operators act on the basis vectors. Thus, the study of

many-body quantum theory becomes more tangible, at least in notation. For example, the electronic Hamiltonian due to electron-nucleus interaction takes the form

$$\mathcal{H}_{en} = \int d\mathbf{r} a^\dagger(\mathbf{r}) \left[-\frac{\hbar^2}{2m} \nabla^2 - \frac{1}{4\pi\epsilon_0} \sum_{\mathbf{R}} \frac{Z}{|\mathbf{R} - \mathbf{r}|} \right] a(\mathbf{r}), \quad (\text{C.16})$$

being rewritten in a more compact form, such as \mathcal{P}_1 , as^[112]:

$$\boxed{\mathcal{H}_{en} = \sum_{\mu\nu} h_{\mu\nu} a_\mu^\dagger a_\nu.} \quad (\text{C.17})$$

The potential due to Coulomb interaction can be expressed as

$$V_{ee} = \frac{1}{4\pi\epsilon_0} \int d\mathbf{r} d\mathbf{r}' a^\dagger(\mathbf{r}) a^\dagger(\mathbf{r}') \frac{1}{|\mathbf{r} - \mathbf{r}'|} a(\mathbf{r}) a(\mathbf{r}'), \quad (\text{C.18})$$

and, similarly, it can be rewritten as

$$\boxed{V_{ee} = \sum_{\mu\nu\kappa\gamma} g_{\mu\nu\kappa\gamma} a_\mu^\dagger a_\nu^\dagger a_\kappa a_\gamma,} \quad (\text{C.19})$$

where $h_{\mu\nu}$ e $g_{\mu\nu\kappa\gamma}$ are the Hamiltonian matrix elements and Coulomb potential in the basis spanned by the $\{|\mu\rangle\}$ vectors, respectively. Let us now consider this same complete orthonormal basis (and these can be atomic or molecular spin orbitals, for example - the real importance here is that this basis must be complete) such that the creation and annihilation operators obey the commutation relations C.9; the molecular (or spin) orbitals can be expanded as

$$a_i^\dagger = \sum_{\mu} C_{\mu i} a_\mu^\dagger, \quad (\text{C.20})$$

where $C_{\mu i} = \langle \mu | i \rangle$ are expansion coefficients from one basis to another. The matrix elements of the density matrix \mathbf{D} in this representation will be given by:

$$D_{\mu\nu} = \sum_{i=1}^n C_{\mu i} C_{\nu i}^*. \quad (\text{C.21})$$

Using the identity relation $\mathbb{1} = \sum_i |i\rangle\langle i|$ and the operator properties shown thus far, it is easy to show that

$$\begin{aligned} D_{\mu\nu} &= \langle 0 | a_\mu a_\nu^\dagger | 0 \rangle \\ D_{\nu\mu} &= \langle 0 | a_\mu^\dagger a_\nu | 0 \rangle. \end{aligned} \tag{C.22}$$

Bibliography

- [1] Kostya S Novoselov, Andre K Geim, Sergei V Morozov, De-eng Jiang, Yanshui Zhang, Sergey V Dubonos, Irina V Grigorieva, and Alexandr A Firsov. Electric field effect in atomically thin carbon films. *science*, 306(5696):666–669, 2004.
- [2] Andre K Geim and Konstantin S Novoselov. The rise of graphene. In *Nanoscience and technology: a collection of reviews from nature journals*, pages 11–19. World Scientific, 2010.
- [3] Andrea C Ferrari, Francesco Bonaccorso, Vladimir Fal’Ko, Konstantin S Novoselov, Stephan Roche, Peter Bøggild, Stefano Borini, Frank HL Koppens, Vincenzo Palermo, Nicola Pugno, et al. Science and technology roadmap for graphene, related two-dimensional crystals, and hybrid systems. *Nanoscale*, 7(11):4598–4810, 2015.
- [4] Kin Fai Mak, Matthew Y Sfeir, Yang Wu, Chun Hung Lui, James A Misewich, and Tony F Heinz. Measurement of the optical conductivity of graphene. *Physical review letters*, 101(19):196405, 2008.
- [5] Sukosin Thongrattanasiri, Frank HL Koppens, and F Javier Garcia De Abajo. Complete optical absorption in periodically patterned graphene. *Physical review letters*, 108(4):047401, 2012.
- [6] Konstantin S Novoselov, VI Fal, L Colombo, PR Gellert, MG Schwab, K Kim, et al. A roadmap for graphene. *nature*, 490(7419):192–200, 2012.
- [7] Frank Schwierz. Graphene transistors. *Nature nanotechnology*, 5(7):487–496, 2010.
- [8] Qing Hua Wang, Kourosch Kalantar-Zadeh, Andras Kis, Jonathan N Coleman, and Michael S Strano. Electronics and optoelectronics of two-dimensional transition metal dichalcogenides. *Nature nanotechnology*, 7(11):699–712, 2012.

- [9] Kostya S Novoselov, Andre K Geim, Sergei Vladimirovich Morozov, Dingde Jiang, Michail I Katsnelson, IVa Grigorieva, SVb Dubonos, and andAA Firsov. Two-dimensional gas of massless dirac fermions in graphene. *nature*, 438(7065):197–200, 2005.
- [10] Xiaofeng Qian, Junwei Liu, Liang Fu, and Ju Li. Quantum spin hall effect in two-dimensional transition metal dichalcogenides. *Science*, 346(6215):1344–1347, 2014.
- [11] Shaolong He, Junfeng He, Wenhao Zhang, Lin Zhao, Defa Liu, Xu Liu, Daixiang Mou, Yun-Bo Ou, Qing-Yan Wang, Zhi Li, et al. Phase diagram and electronic indication of high-temperature superconductivity at 65k in single-layer FeSe films. *Nature materials*, 12(7):605–610, 2013.
- [12] Michael A McGuire, Hemant Dixit, Valentino R Cooper, and Brian C Sales. Coupling of crystal structure and magnetism in the layered, ferromagnetic insulator CrI_3 . *Chemistry of Materials*, 27(2):612–620, 2015.
- [13] Shujie Tang, Chaofan Zhang, Dillon Wong, Zahra Pedramrazi, Hsin-Zon Tsai, Chunjing Jia, Brian Moritz, Martin Claassen, Hyejin Ryu, Salman Kahn, et al. Quantum spin hall state in monolayer $1\text{T}'\text{-WTe}_2$. *Nature Physics*, 13(7):683–687, 2017.
- [14] Xiaolong Liu and Mark C Hersam. 2d materials for quantum information science. *Nature Reviews Materials*, 4(10):669–684, 2019.
- [15] KS Novoselov, o A Mishchenko, o A Carvalho, and AH Castro Neto. 2d materials and van der waals heterostructures. *Science*, 353(6298):aac9439, 2016.
- [16] Victor W Brar, Min Seok Jang, Michelle Sherrott, Seyoon Kim, Josue J Lopez, Laura B Kim, Mansoo Choi, and Harry Atwater. Hybrid surface-phonon-plasmon polariton modes in graphene/monolayer h-BN heterostructures. *Nano letters*, 14(7):3876–3880, 2014.
- [17] Youngki Yoon, Kartik Ganapathi, and Sayeef Salahuddin. How good can monolayer MoS_2 transistors be? *Nano letters*, 11(9):3768–3773, 2011.
- [18] Wei Cao, Jiahao Kang, Deblina Sarkar, Wei Liu, and Kaustav Banerjee. 2d semiconductor fets—projections and design for sub-10 nm vlsi. *IEEE transactions on electron devices*, 62(11):3459–3469, 2015.

- [19] Yifan Sun, Kazunori Fujisawa, Zhong Lin, Yu Lei, Jared S Mondschein, Mauricio Terrones, and Raymond E Schaak. Low-temperature solution synthesis of transition metal dichalcogenide alloys with tunable optical properties. *Journal of the American Chemical Society*, 139(32):11096–11105, 2017.
- [20] Yumei Jing, Baoze Liu, Xukun Zhu, Fangping Ouyang, Jian Sun, and Yu Zhou. Tunable electronic structure of two-dimensional transition metal chalcogenides for optoelectronic applications. *Nanophotonics*, 9(7):1675–1694, 2020.
- [21] Eunji Lee, Young Soo Yoon, and Dong-Joo Kim. Two-dimensional transition metal dichalcogenides and metal oxide hybrids for gas sensing. *ACS sensors*, 3(10):2045–2060, 2018.
- [22] Hyeun Joong Yoon, Jin Ho Yang, Zhixian Zhou, Sang Sik Yang, Mark Ming-Cheng Cheng, et al. Carbon dioxide gas sensor using a graphene sheet. *Sensors and Actuators B: Chemical*, 157(1):310–313, 2011.
- [23] Fazel Yavari and Nikhil Koratkar. Graphene-based chemical sensors. *The journal of physical chemistry letters*, 3(13):1746–1753, 2012.
- [24] Toshiki Akama, Wakana Okita, Reito Nagai, Chao Li, Toshiro Kaneko, and Toshiaki Kato. Schottky solar cell using few-layered transition metal dichalcogenides toward large-scale fabrication of semitransparent and flexible power generator. *Scientific reports*, 7(1):1–10, 2017.
- [25] Marco Bernardi, Maurizia Palummo, and Jeffrey C Grossman. Extraordinary sunlight absorption and one nanometer thick photovoltaics using two-dimensional monolayer materials. *Nano letters*, 13(8):3664–3670, 2013.
- [26] Ding Wei, Zhengguo Lin, Zhentao Cui, Shuangyue Su, Dingkun Zhang, Minhua Cao, and Changwen Hu. Two-step fabrication of a porous γ - In_2Se_3 tetragonal photocatalyst for water splitting. *Chemical Communications*, 49(83):9609–9611, 2013.
- [27] Andre K Geim and Irina V Grigorieva. Van der waals heterostructures. *Nature*, 499(7459):419–425, 2013.
- [28] Nicolas Mounet, Marco Gibertini, Philippe Schwaller, Davide Campi, Andrius Merkys, Antimo Marrazzo, Thibault Sohier, Ivano Eligio Castelli, Andrea Cepel-

- lotti, Giovanni Pizzi, et al. Two-dimensional materials from high-throughput computational exfoliation of experimentally known compounds. *Nature nanotechnology*, 13(3):246–252, 2018.
- [29] Quanjun Xiang and Jiaguo Yu. Graphene-based photocatalysts for hydrogen generation. *The Journal of Physical Chemistry Letters*, 4(5):753–759, 2013.
- [30] Jiaguo Yu, Jian Jin, Bei Cheng, and Mietek Jaroniec. A noble metal-free reduced graphene oxide–cds nanorod composite for the enhanced visible-light photocatalytic reduction of CO₂ to solar fuel. *Journal of materials chemistry A*, 2(10):3407–3416, 2014.
- [31] Jingxiang Low, Shaowen Cao, Jiaguo Yu, and Swelm Wageh. Two-dimensional layered composite photocatalysts. *Chemical communications*, 50(74):10768–10777, 2014.
- [32] Cen-Feng Fu, Jiuyu Sun, Qiquan Luo, Xingxing Li, Wei Hu, and Jinlong Yang. Intrinsic electric fields in two-dimensional materials boost the solar-to-hydrogen efficiency for photocatalytic water splitting. *Nano Lett.*, 18(10):6312–6317, 2018.
- [33] Kin Fai Mak, Changgu Lee, James Hone, Jie Shan, and Tony F Heinz. Atomically thin MoS₂: a new direct-gap semiconductor. *Physical review letters*, 105(13):136805, 2010.
- [34] Kun Chang, Zongwei Mei, Tao Wang, Qing Kang, Shuxin Ouyang, and Jinhua Ye. MoS₂/graphene cocatalyst for efficient photocatalytic H₂ evolution under visible light irradiation. *ACS nano*, 8(7):7078–7087, 2014.
- [35] Yunguo Li, Yan-Ling Li, Carlos Moyses Araujo, Wei Luo, and Rajeev Ahuja. Single-layer MoS₂ as an efficient photocatalyst. *Catalysis Science & Technology*, 3(9):2214–2220, 2013.
- [36] Houlong L Zhuang and Richard G Hennig. Computational search for single-layer transition-metal dichalcogenide photocatalysts. *The Journal of Physical Chemistry C*, 117(40):20440–20445, 2013.
- [37] Eric Parzinger, Bastian Miller, Benno Blaschke, Jose A Garrido, Joel W Ager, Alexander Holleitner, and Ursula Wurstbauer. Photocatalytic stability of single- and few-layer MoS₂. *ACS nano*, 9(11):11302–11309, 2015.

- [38] Zizhan Liang, Rongchen Shen, Yun Hau Ng, Peng Zhang, Qunjun Xiang, and Xin Li. A review on 2d MoS₂ cocatalysts in photocatalytic H₂ production. *Journal of Materials Science & Technology*, 56:89–121, 2020.
- [39] Yijie Ren, Deqian Zeng, and Wee-Jun Ong. Interfacial engineering of graphitic carbon nitride (g-C₃N₄)-based metal sulfide heterojunction photocatalysts for energy conversion: a review. *Chinese Journal of Catalysis*, 40(3):289–319, 2019.
- [40] Peng Zhang, Lijie Wang, Xi Zhang, Junhua Hu, and Guosheng Shao. Three-dimensional porous networks of ultra-long electrospun SnO₂ nanotubes with high photocatalytic performance. *Nano-micro letters*, 7(1):86–95, 2015.
- [41] Alireza Kokabi and Shoeib Babaee Touski. Electronic and photocatalytic properties of antimonene nanosheets. *Physica E: Low-dimensional Systems and Nanostructures*, 124:114336, 2020.
- [42] Xin Wang, Xiantong Yu, Jun Song, Weichun Huang, Yuanjiang Xiang, Xiaoyu Dai, and Han Zhang. Two-dimensional semiconducting antimonene in nanophotonic applications—a review. *Chemical Engineering Journal*, 406:126876, 2021.
- [43] Mohammad Ziaur Rahman, Chi Wai Kwong, Kenneth Davey, and Shi Zhang Qiao. 2d phosphorene as a water splitting photocatalyst: fundamentals to applications. *Energy & Environmental Science*, 9(3):709–728, 2016.
- [44] Wei Hu, Lin Lin, Ruiqi Zhang, Chao Yang, and Jinlong Yang. Highly efficient photocatalytic water splitting over edge-modified phosphorene nanoribbons. *Journal of the American Chemical Society*, 139(43):15429–15436, 2017.
- [45] Xianghong Niu, Yunhai Li, Qionghua Zhou, Huabing Shu, and Jinlan Wang. Arsenene-based heterostructures: highly efficient bifunctional materials for photovoltaics and photocatalytics. *ACS applied materials & interfaces*, 9(49):42856–42861, 2017.
- [46] Martin A Green. The path to 25% silicon solar cell efficiency: History of silicon cell evolution. *Progress in photovoltaics: research and applications*, 17(3):183–189, 2009.
- [47] Masafumi Yamaguchi, Frank Dimroth, John F Geisz, and Nicholas J Ekins-Daukes.

- Multi-junction solar cells paving the way for super high-efficiency. *Journal of Applied Physics*, 129(24):240901, 2021.
- [48] Terry Chien-Jen Yang, Peter Fiala, Quentin Jeangros, and Christophe Ballif. High-bandgap perovskite materials for multijunction solar cells. *Joule*, 2(8):1421–1436, 2018.
- [49] Zhike Liu, Shu Ping Lau, and Feng Yan. Functionalized graphene and other two-dimensional materials for photovoltaic devices: device design and processing. *Chemical Society Reviews*, 44(15):5638–5679, 2015.
- [50] Jianmin Yu, Sohyeon Seo, Yongguang Luo, Yan Sun, Simgeon Oh, Chau TK Nguyen, Changwon Seo, Ji-Hee Kim, Joonsoo Kim, and Hyoyoung Lee. Efficient and stable solar hydrogen generation of hydrophilic rhenium-disulfide-based photocatalysts via chemically controlled charge transfer paths. *ACS nano*, 14(2):1715–1726, 2020.
- [51] Wenchao Peng, Yang Li, Fengbao Zhang, Guoliang Zhang, and Xiaobin Fan. Roles of two-dimensional transition metal dichalcogenides as cocatalysts in photocatalytic hydrogen evolution and environmental remediation. *Industrial & Engineering Chemistry Research*, 56(16):4611–4626, 2017.
- [52] Chengjie Song, Mingshan Fan, Weidong Shi, and Wei Wang. High-performance for hydrogen evolution and pollutant degradation of reduced graphene oxide/two-phase g-C₃N₄ heterojunction photocatalysts. *Environmental Science and Pollution Research*, 25(15):14486–14498, 2018.
- [53] Lan Wang, Detlef W Bahnemann, Liang Bian, Guohui Dong, Jie Zhao, and Chuanyi Wang. Two-dimensional layered zinc silicate nanosheets with excellent photocatalytic performance for organic pollutant degradation and CO₂ conversion. *Angewandte Chemie*, 131(24):8187–8192, 2019.
- [54] Yingxuan Miao, Yunxuan Zhao, Shuai Zhang, Run Shi, and Tierui Zhang. Strain engineering: A boosting strategy for photocatalysis. *Advanced Materials*, page 2200868, 2022.
- [55] Haotian Wang, Shicheng Xu, Charlie Tsai, Yuzhang Li, Chong Liu, Jie Zhao, Yayuan Liu, Hongyuan Yuan, Frank Abild-Pedersen, Fritz B Prinz, et al. Direct

- and continuous strain control of catalysts with tunable battery electrode materials. *Science*, 354(6315):1031–1036, 2016.
- [56] Yang Wang, Xiaopeng Li, Mengmeng Zhang, Yuanguang Zhou, Dewei Rao, Cheng Zhong, Jinfeng Zhang, Xiaopeng Han, Wenbin Hu, Yucang Zhang, et al. Lattice-strain engineering of homogeneous $\text{Ni}_{0.5}\text{Se}_{0.5}$ core-shell nanostructure as a highly efficient and robust electrocatalyst for overall water splitting. *Advanced Materials*, 32(40):2000231, 2020.
- [57] Joshua Mutch, Wei-Chih Chen, Preston Went, Tiema Qian, Ilham Zaky Wilson, Anton Andreev, Cheng-Chien Chen, and Jiun-Haw Chu. Evidence for a strain-tuned topological phase transition in ZrTe_5 . *Science advances*, 5(8):eaav9771, 2019.
- [58] Zhiyong Zhu, Yingchun Cheng, and Udo Schwingenschlögl. Topological phase transition in layered GaS and GaSe. *Physical Review Letters*, 108(26):266805, 2012.
- [59] Xingxing Jiang, Yexin Feng, Ke-Qiu Chen, and Li-Ming Tang. The coexistence of ferroelectricity and topological phase transition in monolayer $\alpha\text{-In}_2\text{Se}_3$ under strain engineering. *Journal of Physics: Condensed Matter*, 32(10):105501, 2019.
- [60] Jun-Jie Zhang, Dongyang Zhu, and Boris I Yakobson. Heterobilayer with ferroelectric switching of topological state. *Nano Letters*, 21(1):785–790, 2020.
- [61] QL Li, Yang Li, Jing Gao, SD Wang, and XH Sun. High performance single In_2Se_3 nanowire photodetector. *Applied Physics Letters*, 99(24):243105, 2011.
- [62] Qin-Liang Li, Chang-Hai Liu, Yu-Ting Nie, Wen-Hua Chen, Xu Gao, Xu-Hui Sun, and Sui-Dong Wang. Phototransistor based on single In_2Se_3 nanosheets. *Nanoscale*, 6(23):14538–14542, 2014.
- [63] Jiadong Zhou, Qingsheng Zeng, Danhui Lv, Linfeng Sun, Lin Niu, Wei Fu, Fucai Liu, Zexiang Shen, Chuanhong Jin, and Zheng Liu. Controlled synthesis of high-quality monolayered $\alpha\text{-In}_2\text{Se}_3$ via physical vapor deposition. *Nano Letters*, 15(10):6400–6405, 2015.
- [64] Bin Tang, Linfang Hou, Mei Sun, Fengjiao Lv, Jianhui Liao, Wei Ji, and Qing Chen. Uv-swir broad range photodetectors made from few-layer $\alpha\text{-In}_2\text{Se}_3$ nanosheets. *Nanoscale*, 11(27):12817–12828, 2019.

- [65] Bin Yu, Sanghyun Ju, Xuhui Sun, Garrick Ng, Thuc Dinh Nguyen, M Meyyappan, and David B Janes. Indium selenide nanowire phase-change memory. *Applied Physics Letters*, 91(13):133119, 2007.
- [66] Yu-Ting Huang, Chun-Wei Huang, Jui-Yuan Chen, Yi-Hsin Ting, Kuo-Chang Lu, Yu-Lun Chueh, and Wen-Wei Wu. Dynamic observation of phase transformation behaviors in indium (iii) selenide nanowire based phase change memory. *ACS nano*, 8(9):9457–9462, 2014.
- [67] Wenjun Ding, Jianbao Zhu, Zhe Wang, Yanfei Gao, Di Xiao, Yi Gu, Zhenyu Zhang, and Wenguang Zhu. Prediction of intrinsic two-dimensional ferroelectrics in In_2Se_3 and other $\text{III}_2\text{--VI}_3$ van der waals materials. *Nature communications*, 8(1):1–8, 2017.
- [68] Yu Zhou, Di Wu, Yihan Zhu, Yujin Cho, Qing He, Xiao Yang, Kevin Herrera, Zhaodong Chu, Yu Han, Michael C Downer, et al. Out-of-plane piezoelectricity and ferroelectricity in layered $\alpha\text{-In}_2\text{Se}_3$ nanoflakes. *Nano letters*, 17(9):5508–5513, 2017.
- [69] Chaojie Cui, Wei-Jin Hu, Xingxu Yan, Christopher Addiego, Wenpei Gao, Yao Wang, Zhe Wang, Linze Li, Yingchun Cheng, Peng Li, et al. Intercorrelated in-plane and out-of-plane ferroelectricity in ultrathin two-dimensional layered semiconductor In_2Se_3 . *Nano letters*, 18(2):1253–1258, 2018.
- [70] David Vanderbilt. *Berry Phases in Electronic Structure Theory: Electric Polarization, Orbital Magnetization and Topological Insulators*. Cambridge University Press, 2018.
- [71] A Bohm, B Kendrick, and Mark E Loewe. The berry phase in molecular physics. *International journal of quantum chemistry*, 41(1):53–75, 1992.
- [72] Michael Victor Berry. Quantal phase factors accompanying adiabatic changes. *Proceedings of the Royal Society of London. A. Mathematical and Physical Sciences*, 392(1802):45–57, 1984.
- [73] Max Born and Vladimir Fock. Beweis des adiabatenatzes. *Zeitschrift für Physik*, 51(3-4):165–180, 1928.
- [74] Shiing-shen Chern. A simple intrinsic proof of the gauss-bonnet formula for closed riemannian manifolds. *Annals of mathematics*, pages 747–752, 1944.

- [75] Barry Simon. Holonomy, the quantum adiabatic theorem, and berry's phase. *Physical Review Letters*, 51(24):2167, 1983.
- [76] Qian Niu, Ds J Thouless, and Yong-Shi Wu. Quantized hall conductance as a topological invariant. *Physical Review B*, 31(6):3372, 1985.
- [77] Edwin H Hall et al. On a new action of the magnet on electric currents. *American Journal of Mathematics*, 2(3):287–292, 1879.
- [78] Chao-Xing Liu, Shou-Cheng Zhang, and Xiao-Liang Qi. The quantum anomalous hall effect: Theory and experiment. *Annual Review of Condensed Matter Physics*, 7:301–321, 2016.
- [79] M Zahid Hasan and Charles L Kane. Colloquium: topological insulators. *Reviews of modern physics*, 82(4):3045, 2010.
- [80] K v Klitzing, Gerhard Dorda, and Michael Pepper. New method for high-accuracy determination of the fine-structure constant based on quantized hall resistance. *Physical review letters*, 45(6):494, 1980.
- [81] MA Paalanen, DC Tsui, and AC Gossard. Quantized hall effect at low temperatures. *Physical Review B*, 25(8):5566, 1982.
- [82] David J Thouless, Mahito Kohmoto, M Peter Nightingale, and Marcel den Nijs. Quantized hall conductance in a two-dimensional periodic potential. *Physical review letters*, 49(6):405, 1982.
- [83] F Duncan M Haldane. Model for a quantum hall effect without landau levels: Condensed-matter realization of the “parity anomaly”. *Physical review letters*, 61(18):2015, 1988.
- [84] B Andrei Bernevig. *Topological insulators and topological superconductors*. Princeton university press, 2013.
- [85] Charles L. Kane and Eugene J. Mele. Quantum spin hall effect in graphene. *Physical review letters*, 95(22):226801, 2005.
- [86] B Andrei Bernevig and Shou-Cheng Zhang. Quantum spin hall effect. *Physical review letters*, 96(10):106802, 2006.

- [87] B Andrei Bernevig, Taylor L Hughes, and Shou-Cheng Zhang. Quantum spin hall effect and topological phase transition in HgTe quantum wells. *science*, 314(5806):1757–1761, 2006.
- [88] Haijun Zhang, Chao-Xing Liu, Xiao-Liang Qi, Xi Dai, Zhong Fang, and Shou-Cheng Zhang. Topological insulators in Bi_2Se_3 , Bi_2Te_3 and Sb_2Te_3 with a single dirac cone on the surface. *Nature physics*, 5(6):438–442, 2009.
- [89] Jason M Crowley, Jamil Tahir-Kheli, and William A Goddard III. Accurate ab initio quantum mechanics simulations of Bi_2Se_3 and Bi_2Te_3 topological insulator surfaces. *The journal of physical chemistry letters*, 6(19):3792–3796, 2015.
- [90] Marcel Franz and Laurens Molenkamp. *Topological insulators*. Elsevier, 2013.
- [91] Shuichi Murakami, Naoto Nagaosa, and Shou-Cheng Zhang. Dissipationless quantum spin current at room temperature. *Science*, 301(5638):1348–1351, 2003.
- [92] Eduardo Fradkin. *Field theories of condensed matter physics*. Cambridge University Press, 2013.
- [93] Charles L. Kane and Eugene J. Mele. \mathbb{Z}_2 topological order and the quantum spin hall effect. *Physical review letters*, 95(14):146802, 2005.
- [94] Liang Fu, Charles L. Kane, and Eugene J. Mele. Topological insulators in three dimensions. *Physical review letters*, 98(10):106803, 2007.
- [95] Joel E Moore and Leon Balents. Topological invariants of time-reversal-invariant band structures. *Physical Review B*, 75(12):121306, 2007.
- [96] Xiao-Liang Qi, Taylor L Hughes, and Shou-Cheng Zhang. Topological field theory of time-reversal invariant insulators. *Physical Review B*, 78(19):195424, 2008.
- [97] Rahul Roy. \mathbb{Z}_2 classification of quantum spin hall systems: An approach using time-reversal invariance. *Physical Review B*, 79(19):195321, 2009.
- [98] DN Sheng, ZY Weng, L Sheng, and FDM Haldane. Quantum spin-hall effect and topologically invariant chern numbers. *Physical review letters*, 97(3):036808, 2006.
- [99] Liang Fu and Charles L Kane. Time reversal polarization and a \mathbb{Z}_2 adiabatic spin pump. *Physical Review B*, 74(19):195312, 2006.

- [100] Alexey A Soluyanov and David Vanderbilt. Computing topological invariants without inversion symmetry. *Physical Review B*, 83(23):235401, 2011.
- [101] EI Blount. Formalisms of band theory. In *Solid state physics*, volume 13, pages 305–373. Elsevier, 1962.
- [102] J Zak. Berry’s phase for energy bands in solids. *Physical review letters*, 62(23):2747, 1989.
- [103] QuanSheng Wu, ShengNan Zhang, Hai-Feng Song, Matthias Troyer, and Alexey A. Soluyanov. Wanniertools : An open-source software package for novel topological materials. *Computer Physics Communications*, 224:405 – 416, 2018.
- [104] Trygve Helgaker, Poul Jorgensen, and Jeppe Olsen. *Molecular electronic-structure theory*. John Wiley & Sons, 2014.
- [105] Douglas R Hartree. The wave mechanics of an atom with a non-coulomb central field. part i. theory and methods. *Math. Proc. Cambridge Philos. Soc*, 24:89–110, 1928.
- [106] Vladimir Fock. Näherungsmethode zur lösung des quantenmechanischen mehrkörperproblems. *Zeitschrift für Physik*, 61(1-2):126–148, 1930.
- [107] V Fock. Selfconsistent field “mit austausch für natrium. *Zeitschrift für Physik*, 62(11):795–805, 1930.
- [108] John C Slater. The theory of complex spectra. *Physical Review*, 34(10):1293, 1929.
- [109] Eva Pavarini, Erik Koch, Jeroen van den Brink, and George Sawatzky. Quantum materials: Experiments and theory. *Modeling and Simulation*, 6:420, 2016.
- [110] Pierre Hohenberg and Walter Kohn. Inhomogeneous electron gas. *Physical review*, 136(3B):B864, 1964.
- [111] Walter Kohn and Lu Jeu Sham. Self-consistent equations including exchange and correlation effects. *Physical review*, 140(4A):A1133, 1965.
- [112] Thomas Kjærgaard, Poul Jørgensen, Jeppe Olsen, Sonia Coriani, and Trygve Helgaker. Hartree-fock and kohn-sham time-dependent response theory in a second-quantization atomic-orbital formalism suitable for linear scaling. *The Journal of chemical physics*, 129(5):054106, 2008.

- [113] Richard M. Martin. *Electronic Structure: Basic Theory and Practical Methods*, volume Vol 1. Cambridge University Press, 2004.
- [114] John P Perdew, Robert G Parr, Mel Levy, and Jose L Balduz Jr. Density-functional theory for fractional particle number: derivative discontinuities of the energy. *Physical Review Letters*, 49(23):1691, 1982.
- [115] A Seidl, Andreas Görling, Peter Vogl, Jacek A Majewski, and Mel Levy. Generalized kohn-sham schemes and the band-gap problem. *Physical Review B*, 53(7):3764, 1996.
- [116] Axel D Becke. Density-functional thermochemistry. i. the effect of the exchange-only gradient correction. *The Journal of chemical physics*, 96(3):2155–2160, 1992.
- [117] John P Perdew, Matthias Ernzerhof, and Kieron Burke. Rationale for mixing exact exchange with density functional approximations. *The Journal of chemical physics*, 105(22):9982–9985, 1996.
- [118] Jochen Heyd, Gustavo E Scuseria, and Matthias Ernzerhof. Hybrid functionals based on a screened coulomb potential. *The Journal of chemical physics*, 118(18):8207–8215, 2003.
- [119] Jochen Heyd, Juan E Peralta, Gustavo E Scuseria, and Richard L Martin. Energy band gaps and lattice parameters evaluated with the heyd-scuseria-ernzerhof screened hybrid functional. *The Journal of chemical physics*, 123(17):174101, 2005.
- [120] Chengteh Lee, Weitao Yang, and Robert G Parr. Development of the colle-salvetti correlation-energy formula into a functional of the electron density. *Physical review B*, 37(2):785, 1988.
- [121] John P Perdew, Kieron Burke, and Matthias Ernzerhof. Generalized gradient approximation made simple. *Physical review letters*, 77(18):3865, 1996.
- [122] Aliaksandr V Krukau, Oleg A Vydrov, Artur F Izmaylov, and Gustavo E Scuseria. Influence of the exchange screening parameter on the performance of screened hybrid functionals. *The Journal of chemical physics*, 125(22):224106, 2006.
- [123] Paolo Giannozzi, Stefano Baroni, Nicola Bonini, Matteo Calandra, Roberto Car, Carlo Cavazzoni, Davide Ceresoli, Guido L Chiarotti, Matteo Cococcioni, Ismaila Dabo, et al. Quantum espresso: a modular and open-source software project

- for quantum simulations of materials. *Journal of physics: Condensed matter*, 21(39):395502, 2009.
- [124] Paolo Giannozzi, Oliviero Andreussi, Thomas Brumme, Oana Bunau, M Buongiorno Nardelli, Matteo Calandra, Roberto Car, Carlo Cavazzoni, Davide Ceresoli, Matteo Cococcioni, et al. Advanced capabilities for materials modelling with quantum espresso. *Journal of physics: Condensed matter*, 29(46):465901, 2017.
- [125] Peter E Blöchl. Projector augmented-wave method. *Physical review B*, 50(24):17953, 1994.
- [126] Norman Troullier and José Luís Martins. Efficient pseudopotentials for plane-wave calculations. *Physical review B*, 43(3):1993, 1991.
- [127] Hendrik J Monkhorst and James D Pack. Special points for brillouin-zone integrations. *Physical review B*, 13(12):5188, 1976.
- [128] MPAT Methfessel and AT Paxton. High-precision sampling for brillouin-zone integration in metals. *Physical Review B*, 40(6):3616, 1989.
- [129] Cen-Feng Fu, Jiuyu Sun, Qiquan Luo, Xingxing Li, Wei Hu, and Jinlong Yang. Intrinsic electric fields in two-dimensional materials boost the solar-to-hydrogen efficiency for photocatalytic water splitting. *Nano letters*, 18(10):6312–6317, 2018.
- [130] Xiaoyong Yang, Amitava Banerjee, Zhitong Xu, Ziwei Wang, and Rajeev Ahuja. Interfacial aspect of znTe/In₂Te₃ heterostructures as an efficient catalyst for the hydrogen evolution reaction. *Journal of Materials Chemistry A*, 7(48):27441–27449, 2019.
- [131] Zhen-Kun Tang, Wen-Jin Yin, Le Zhang, Bo Wen, Deng-Yu Zhang, Li-Min Liu, and Woon-Ming Lau. Spatial separation of photo-generated electron-hole pairs in biobr/bioi bilayer to facilitate water splitting. *Scientific reports*, 6(1):1–9, 2016.
- [132] Wei Zhou and Naoto Umezawa. Band gap engineering of bulk and nanosheet sno: an insight into the interlayer sn–sn lone pair interactions. *Physical Chemistry Chemical Physics*, 17(27):17816–17820, 2015.
- [133] Dequan Er, Han Ye, Nathan C Frey, Hemant Kumar, Jun Lou, and Vivek B Shenoy. Prediction of enhanced catalytic activity for hydrogen evolution reaction in janus transition metal dichalcogenides. *Nano letters*, 18(6):3943–3949, 2018.

- [134] Ruimiao Wang, Jun Wan, Jia Jia, Wenhua Xue, Xiaoyun Hu, Enzhou Liu, and Jun Fan. Synthesis of In_2Se_3 homojunction photocatalyst with α and γ phases for efficient photocatalytic performance. *Materials & Design*, 151:74–82, 2018.
- [135] ST Lakshmikumar and AC Rastogi. Selenization of Cu and in thin films for the preparation of selenide photo-absorber layers in solar cells using se vapour source. *Solar Energy Materials and Solar Cells*, 32(1):7–19, 1994.
- [136] Heon Lee, Dae-Hwan Kang, and Lung Tran. Indium selenide (In_2Se_3) thin film for phase-change memory. *Materials Science and Engineering: B*, 119(2):196–201, 2005.
- [137] Robin B Jacobs-Gedrim, Mariyappan Shanmugam, Nikhil Jain, Christopher A Durcan, Michael T Murphy, Thomas M Murray, Richard J Matyi, Richard L Moore, and Bin Yu. Extraordinary photoresponse in two-dimensional In_2Se_3 nanosheets. *ACS nano*, 8(1):514–521, 2014.
- [138] Jiping Ye, Sigeo Soeda, Yoshio Nakamura, and Osamu Nittono. Crystal structures and phase transformation in In_2Se_3 compound semiconductor. *Japanese journal of applied physics*, 37(8R):4264, 1998.
- [139] Ching-Hwa Ho, Chien-Hao Lin, Yi-Ping Wang, Ying-Cen Chen, Shin-Hong Chen, and Ying-Sheng Huang. Surface oxide effect on optical sensing and photoelectric conversion of α - In_2Se_3 hexagonal microplates. *ACS applied materials & interfaces*, 5(6):2269–2277, 2013.
- [140] Lamjed Debbichi, Olle Eriksson, and Sébastien Lebègue. Two-dimensional indium selenides compounds: an ab initio study. *The journal of physical chemistry letters*, 6(15):3098–3103, 2015.
- [141] Fredrik Schedin, AK Geim, SV Morozov, EW Hill, P Blake, MI Katsnelson, and KS Novoselov. Detection of individual gas molecules adsorbed on graphene. *Nat. Mater.*, 6(9):652, 2007.
- [142] Rashida Arsat, Michael Breedon, Mahnaz Shafiei, PG Spizziri, Scott Gilje, RB Kaner, Kouros Kalantar-zadeh, and Wojtek Wlodarski. Graphene-like nanosheets for surface acoustic wave gas sensor applications. *Chem. Phys. Lett.*, 467(4-6):344–347, 2009.

- [143] Fábio AL de Souza, Rodrigo G Amorim, Jariyane Prasangkit, Wanderlã L Scopel, Ralph H Scheicher, and Alexandre R Rocha. Topological line defects in graphene for applications in gas sensing. *Carbon*, 129:803–808, 2018.
- [144] F Traversi, C Raillon, SM Benameur, K Liu, S Khlybov, M Tosun, D Krasnozhan, A Kis, and A Radenovic. Detecting the translocation of dna through a nanopore using graphene nanoribbons. *Nat. Nanotechnol.*, 8(12):939, 2013.
- [145] Fábio AL de Souza, Rodrigo G Amorim, Wanderlã L Scopel, and Ralph H Scheicher. Electrical detection of nucleotides via nanopores in a hybrid graphene/h-BN sheet. *Nanoscale*, 9(6):2207–2212, 2017.
- [146] Jariyane Prasangkit, Ernane de Freitas Martins, Fábio AL De Souza, Wanderlã L Scopel, Rodrigo G Amorim, Vittaya Amornkitbamrung, Alexandre R Rocha, and Ralph H Scheicher. Topological line defects around graphene nanopores for dna sequencing. *J. Phys. Chem. C*, 122(13):7094–7099, 2018.
- [147] Dongwei Ma, Weiwei Ju, Yanan Tang, and Yue Chen. First-principles study of the small molecule adsorption on the InSe monolayer. *Appl. Surf. Sci.*, 426:244–252, 2017.
- [148] Zhi Xie, Fugui Yang, Xue Xu, Rui Lin, and Limin Chen. Functionalization of α -In₂Se₃ monolayer via adsorption of small molecule for gas sensing. *Frontiers in Chemistry*, page 430, 2018.
- [149] John E Ayers, Tedi Kujofsa, Paul Rago, and Johanna Raphael. *Heteroepitaxy of semiconductors: theory, growth, and characterization*. CRC press, 2016.
- [150] Muhammad Iqbal Bakti Utama, Qing Zhang, Jun Zhang, Yanwen Yuan, Francisco J Belarre, Jordi Arbiol, and Qihua Xiong. Recent developments and future directions in the growth of nanostructures by van der waals epitaxy. *Nanoscale*, 5(9):3570–3588, 2013.
- [151] Wei Feng, Wei Zheng, Feng Gao, Xiao Shuang Chen, Guangbo Liu, Tawfique Hasan, Wen Wu Cao, and Ping An Hu. Sensitive electronic-skin strain sensor array based on the patterned two-dimensional α -In₂Se₃. *Chem. Mater.*, 28(12):4278–4283, 2016.
- [152] G. Kresse and J. Furthmüller. Efficient iterative schemes for ab initio total-energy calculations using a plane-wave basis set. *Phys. Rev. B*, 54:11169–11186, Oct 1996.

- [153] M Gajdoš, K Hummer, G Kresse, J Furthmüller, and F Bechstedt. Linear optical properties in the projector-augmented wave methodology. *Physical Review B*, 73(4):045112, 2006.
- [154] Kozo Osamura, Yotaro Murakami, and Yujiro Tomiie. Crystal structures of α - and β -indium selenide, In_2Se_3 . *Journal of the Physical Society of Japan*, 21(9):1848–1848, 1966.
- [155] Xin Tao and Yi Gu. Crystalline–crystalline phase transformation in two-dimensional In_2Se_3 thin layers. *Nano letters*, 13(8):3501–3505, 2013.
- [156] Jinggeng Zhao and Liuxiang Yang. Structure evolutions and metallic transitions in In_2Se_3 under high pressure. *The Journal of Physical Chemistry C*, 118(10):5445–5452, 2014.
- [157] Rosario Vilaplana, Samuel Gallego Parra, Alejandro Jorge-Montero, Placida Rodriguez-Hernandez, Alfonso Munoz, Daniel Errandonea, Alfredo Segura, and Francisco Javier Manjon. Experimental and theoretical studies on α - In_2Se_3 at high pressure. *Inorganic chemistry*, 57(14):8241–8252, 2018.
- [158] Jan Rossmeisl, Ashildur Logadottir, and Jens Kehlet Nørskov. Electrolysis of Water on (Oxidized) metal surfaces. *Chem. Phys.*, 319(1-3):178–184, 2005.
- [159] Amitava Banerjee, Sudip Chakraborty, Naresh K Jena, and Rajeev Ahuja. Scrupulous Probing of Bifunctional Catalytic Activity of Borophene Monolayer: Mapping Reaction Coordinate with Charge Transfer. *ACS Appl. Energy Mater.*, 1(8):3571–3576, 2018.
- [160] Jens Kehlet Nørskov, Thomas Bligaard, Ashildur Logadottir, JR Kitchin, Jingguang G Chen, S Pandelov, and U Stimming. Trends in the Exchange Current for Hydrogen Evolution. *J. Electrochem. Soc.*, 152(3):J23–J26, 2005.
- [161] Shengli Zhang, Zhong Yan, Yafei Li, Zhongfang Chen, and Haibo Zeng. Atomically thin arsenene and antimonene: semimetal–semiconductor and indirect–direct band-gap transitions. *Angewandte Chemie*, 127(10):3155–3158, 2015.
- [162] Yury Yu Illarionov, Theresia Knobloch, Markus Jech, Mario Lanza, Deji Akinwande, Mikhail I Vexler, Thomas Mueller, Max C Lemme, Gianluca Fiori, Frank Schwierz,

- et al. Insulators for 2d nanoelectronics: the gap to bridge. *Nature Communications*, 11(1):1–15, 2020.
- [163] Andre K Geim. Nobel lecture: Random walk to graphene. *Reviews of Modern Physics*, 83(3):851, 2011.
- [164] Qiang Li, Qionghua Zhou, Li Shi, Qian Chen, and Jinlan Wang. Recent advances in oxidation and degradation mechanisms of ultrathin 2d materials under ambient conditions and their passivation strategies. *Journal of Materials Chemistry A*, 7(9):4291–4312, 2019.
- [165] Jiali Yang, Yuanjun Jin, Wangping Xu, Baobing Zheng, Rui Wang, and Hu Xu. Oxidation-induced topological phase transition in monolayer 1T–WTe₂. *The Journal of Physical Chemistry Letters*, 9(16):4783–4788, 2018.
- [166] Joshua D Wood, Spencer A Wells, Deep Jariwala, Kan-Sheng Chen, EunKyung Cho, Vinod K Sangwan, Xiaolong Liu, Lincoln J Lauhon, Tobin J Marks, and Mark C Hersam. Effective passivation of exfoliated black phosphorus transistors against ambient degradation. *Nano letters*, 14(12):6964–6970, 2014.
- [167] Steven P Koenig, Rostislav A Doganov, Henrik Schmidt, AH Castro Neto, and Barbaros Özyilmaz. Electric field effect in ultrathin black phosphorus. *Applied Physics Letters*, 104(10):103106, 2014.
- [168] Wenhan Zhou, Shengli Zhang, Shiyong Guo, Yangyang Wang, Jing Lu, Xing Ming, Zhi Li, Hengze Qu, and Haibo Zeng. Designing sub-10-nm metal-oxide-semiconductor field-effect transistors via ballistic transport and disparate effective mass: The case of two-dimensional BiN. *Physical Review Applied*, 13(4):044066, 2020.
- [169] Wenhan Zhou, Shengli Zhang, Yangyang Wang, Shiyong Guo, Hengze Qu, Pengxiang Bai, Zhi Li, and Haibo Zeng. Anisotropic in-plane ballistic transport in monolayer black arsenic-phosphorus FETs. *Advanced Electronic Materials*, 6(3):1901281, 2020.
- [170] Chengyong Zhong, Weikang Wu, Junjie He, Guangqian Ding, Yi Liu, Dengfeng Li, Shengyuan A Yang, and Gang Zhang. Two-dimensional honeycomb borophene oxide: Strong anisotropy and nodal loop transformation. *Nanoscale*, 11(5):2468–2475, 2019.

- [171] Shengli Zhang, Wenhan Zhou, Yandong Ma, Jianping Ji, Bo Cai, Shengyuan A Yang, Zhen Zhu, Zhongfang Chen, and Haibo Zeng. Antimonene oxides: emerging tunable direct bandgap semiconductor and novel topological insulator. *Nano letters*, 17(6):3434–3440, 2017.
- [172] Kai Chang, Junwei Liu, Haicheng Lin, Na Wang, Kun Zhao, Anmin Zhang, Feng Jin, Yong Zhong, Xiaopeng Hu, Wenhui Duan, et al. Discovery of robust in-plane ferroelectricity in atomic-thick SnTe. *Science*, 353(6296):274–278, 2016.
- [173] Changxi Zheng, Lei Yu, Lin Zhu, James L Collins, Dohyung Kim, Yaoding Lou, Chao Xu, Meng Li, Zheng Wei, Yupeng Zhang, et al. Room temperature in-plane ferroelectricity in van der waals In_2Se_3 . *Science advances*, 4(7):7720, 2018.
- [174] Mehmet Dogan, Stephanie Fernandez-Pena, Lior Kornblum, Yichen Jia, Divine P Kumah, James W Reiner, Zoran Krivokapic, Alexie M Kolpak, Sohrab Ismail-Beigi, Charles H Ahn, et al. Single atomic layer ferroelectric on silicon. *Nano letters*, 18(1):241–246, 2018.
- [175] Mutee Ur Rehman, Chenqiang Hua, and Yunhao Lu. Topology and ferroelectricity in group-v monolayers. *Chinese Physics B*, 29(5):057304, 2020.
- [176] Hua Bai, Xinwei Wang, Weikang Wu, Pimo He, Shengyuan A Yang, Yunhao Lu, et al. Nonvolatile ferroelectric control of topological states in two-dimensional heterostructures. *Physical Review B*, 102(23):235403, 2020.
- [177] Adam S Foster, VB Sulimov, F Lopez Gejo, AL Shluger, and Risto M Nieminen. Structure and electrical levels of point defects in monoclinic zirconia. *Physical Review B*, 64(22):224108, 2001.
- [178] Adam S Foster, F Lopez Gejo, AL Shluger, and Risto M Nieminen. Vacancy and interstitial defects in hafnia. *Physical Review B*, 65(17):174117, 2002.
- [179] J-P Crocombette. Theoretical study of point defects in crystalline zircon. *Physics and Chemistry of Minerals*, 27(2):138–143, 1999.
- [180] Md Zakir Hossain, James E Johns, Kirk H Bevan, Hunter J Karmel, Yu Teng Liang, Shinya Yoshimoto, Kozo Mukai, Tatanori Koitaya, Jun Yoshinobu, Maki Kawai, et al. Chemically homogeneous and thermally reversible oxidation of epitaxial graphene. *Nature chemistry*, 4(4):305–309, 2012.

- [181] Ruiqi Zhang, Zhenyu Li, and Jinlong Yang. Two-dimensional stoichiometric boron oxides as a versatile platform for electronic structure engineering. *The Journal of Physical Chemistry Letters*, 8(18):4347–4353, 2017.
- [182] Wanderla L Scopel, Everson S Souza, and Roberto H Miwa. H₂O incorporation in the phosphorene/a-SiO₂ interface: a first-principles study. *Journal of Physics: Condensed Matter*, 29(7):075002, 2016.
- [183] Shi Liu, Youngkuk Kim, Liang Z Tan, and Andrew M Rappe. Strain-induced ferroelectric topological insulator. *Nano Letters*, 16(3):1663–1668, 2016.
- [184] Giovanni Pizzi, Valerio Vitale, Ryotaro Arita, Stefan Blügel, Frank Freimuth, Guillaume Géranton, Marco Gibertini, Dominik Gresch, Charles Johnson, Takashi Kotetsune, Julen Ibañez-Azpiroz, Hyungjun Lee, Jae-Mo Lihm, Daniel Marchand, Antimo Marrazzo, Yuriy Mokrousov, Jamal I Mustafa, Yoshiro Nohara, Yusuke Nomura, Lorenzo Paulatto, Samuel Poncé, Thomas Ponweiser, Junfeng Qiao, Florian Thöle, Stepan S Tsirkin, Małgorzata Wierzbowska, Nicola Marzari, David Vanderbilt, Ivo Souza, Arash A Mostofi, and Jonathan R Yates. Wannier90 as a community code: new features and applications. *Journal of Physics: Condensed Matter*, 32(16):165902, jan 2020.
- [185] Yandong Ma, Liangzhi Kou, Ying Dai, and Thomas Heine. Proposed two-dimensional topological insulator in SiTe. *Physical Review B*, 94(20):201104, 2016.
- [186] Tamiru Teshome and Ayan Datta. Phase coexistence and strain-induced topological insulator in two-dimensional BiAs. *The Journal of Physical Chemistry C*, 122(26):15047–15054, 2018.
- [187] Shuichi Murakami, Satoshi Iso, Yshai Avishai, Masaru Onoda, and Naoto Nagaosa. Tuning phase transition between quantum spin hall and ordinary insulating phases. *Physical Review B*, 76(20):205304, 2007.
- [188] Shuichi Murakami and Shun-ichi Kuga. Universal phase diagrams for the quantum spin hall systems. *Physical Review B*, 78(16):165313, 2008.
- [189] David Vanderbilt and RD King-Smith. Electric polarization as a bulk quantity and its relation to surface charge. *Physical Review B*, 48(7):4442, 1993.

- [190] Ivo Souza, Richard M Martin, Nicola Marzari, Xinyuan Zhao, and David Vanderbilt. Wannier-function description of the electronic polarization and infrared absorption of high-pressure hydrogen. *Physical Review B*, 62(23):15505, 2000.
- [191] Nicola Marzari, Ivo Souza, and David Vanderbilt. An introduction to maximally-localized wannier functions. *Psi-K newsletter*, 57:129, 2003.
- [192] Nicola Marzari and David Vanderbilt. Maximally localized generalized wannier functions for composite energy bands. *Physical review B*, 56(20):12847, 1997.
- [193] Paul Adrien Maurice Dirac. The quantum theory of the emission and absorption of radiation. *Proceedings of the Royal Society of London. Series A, Containing Papers of a Mathematical and Physical Character*, 114(767):243–265, 1927.
- [194] A. Altland and B. Simons. *Condensed Matter Field Theory*. Cambridge University Press, England, 2010.
- [195] C. Kittel. *Quantum Theory of Solids*. John Wiley & Sons, New York, 1987.
- [196] Ivan Todorov. Quantization is a mystery. *Bulgarian Journal of Physics*, 39:107–149, 2012.
- [197] J. J. Sakurai and J. Napolitano. *Mecânica Quântica Moderna, 2a Ed.* Bookman, Porto Alegre, 2013.
- [198] C. Cohen-Tannoudji, B. Diu, and F. Laloë. *Quantum Mechanics, Vol. 2*. Wiley & Sons, New York, 1976.